Mechanistic Studies of Thiol Additions to Electrophilic Warheads

Sarah Watt

A thesis submitted in partial fulfillment of the requirements for the

Master of Science degree in Chemistry

Department of Chemistry and Biomolecular Sciences

Faculty of Science

University of Ottawa

Abstract

Targeted covalent inhibitors (TCIs) are irreversible enzyme inhibitors that are designed to first bind to a targeted enzyme's active site reversibly using non-covalent interactions between the molecular scaffold of the inhibitor and the surrounding amino acid residues of the enzyme's binding site. They then form a covalent bond between the inhibitor's electrophilic warhead and a nucleophilic amino acid residue located inside of the binding pocket. Cysteine (Cys), a redox-sensitive thiol, is found in many enzyme active sites and is used as the target for many current TCIs in clinical application. Electrophilic warheads such as acrylamides and chloroacetamides are known to readily undergo thiol-addition, and although they are commonly used in the development of enzyme inhibitors, few previous studies have explored the mechanism of thiol-addition and the intrinsic reactivities of these moieties. In this work, a robust kinetic assay was developed to perform mechanistic studies of thiol-addition to the electrophilic warhead derivatives *N*-phenylacrylamide (NPA), *N*-acryloylpiperidine (AcrPip), and *N*-phenylchloroacetamide (NPC). By reacting these warhead derivatives with thiol nucleophiles having various pK_a values, we were able to construct Brønsted-type plots, resulting in shallow positive β_{Nuc}^{RS-} values for NPA, AcrPip and NPC (β_{Nuc}^{RS-} = 0.07 ± 0.04, 0.11 ± 0.03, and 0.21 ± 0.07, respectively), meaning that these electrophiles are relatively insensitive to thiolate nucleophilicity. However, while the trend in their reactivity across thiolate nucleophilicity is similar, their intrinsic reactivity was found to be vastly different. In conjunction with the Brønsted-type plot, temperature, ionic strength, and kinetic isotope effects were studied to afford information about the rate-limiting transition state and elucidate the mechanism of thiol-addition. NPA and AcrPip were found to undergo very similar thiol-additions, consistent with the microscopic reverse of the $E1_{cb}^{rev}$ elimination, whereas NPC

follows an S_N2 type addition, consistent with the intuitive mechanism of addition to a haloacetamide.

Keywords: acrylamide, chloroacetamide, Michael-addition, S_N2, glutathione, thiol-addition

Acknowledgments

First, I would like to thank my supervisor Jeff for his dedication to the Keillor research group, and his undying support and kindness throughout my time in his lab. You never failed to make time to discuss issues I encountered with my project and answer any questions I had about new concepts and techniques. I would also like to thank you for your patience and confidence in me when dealing with our HPLC woes.

To both past and present Keillor group members, I would like to thank you all for your help fielding ideas for my project and willingness to learn some physical organic chemistry during my group meeting presentations! I would especially like to thank former Keillor group member Kelvin for showing me the ropes and helping get the first iteration of my project off the ground. Eric, thank you for being the ultimate go-to person for all things lab related and for keeping me in the loop when good concert tickets went on sale! Alana, thank you for all your help with my synthesis questions, and for your delicious cookies and mixology creations. Lastly a very special thank you to Pauline for being my constant sounding board, maintaining my sanity, and enabling my caffeine addiction. You definitely made sure that there was never a dull moment!

I would also like to thank my family for their constant support – I couldn't have done this without you backing me the entire way. Mom, thank you for reading all of my written work, even when you had to learn a new subject in order to understand it, and for making frequent five-hour treks to visit me. Dad, thank you for all the dinners and unending supply of wine. Jacqueline, thank you for being my unofficial tutor throughout my undergrad. Finally, thank you Alex for helping me move between apartments on multiple occasions with very few complaints.

Dedication

To my grandfather, Lynn A. K. Watt – you inspired my never-ending curiosity and desire to curate an infinitely diverse library.

Table of Contents

Table of Figures

CHAPTER 4

APPENDIX I

Table of Schemes

Table of Tables

Epigraph

"Our curiosity is supposed to have limits, though these have never been defined exactly."

- Margaret Atwood

Chapter 1 : Introduction

1.1 Medicinal chemistry

Medicinal chemistry is an invaluable field of research today, being the foundational pillar of drug design, development, and evaluation. Modern medicinal chemistry is said to have been birthed in the late 1800s, not gaining formal recognition as an established discipline until the 20thcentury, with the introduction of side chain theory by Ehrlich leading to the revelation of drug receptor theory and discovery of enzyme specificity by Fischer in 1894 and enzyme-substrate complex formation by Henry in 1903.[1] These concepts form the base of our understanding of structure activity relationships (SARs) between small molecule drugs and their enzymatic targets. Though these advanced theories of medicinal chemistry were not established until this time, records of ancient apothecary are vast, dating all the way back to 2735 B.C. in Babylonian times where there's evidence for over 100 drug-like substances derived from vegetables.[2] This trend continues throughout the following centuries, prevailing in many civilizations including ancient China, Egypt, and Greece, as well as on the European continent, up until this day.

The largest shift in the modern-day field comes in the form of regulatory control. Simultaneous to the establishment of pharmaceutical sciences and medicinal chemistry in the 20th century, regulatory agencies such as the United States Food and Drug Administration (FDA) and the Canadian Food and Drugs Act were created. Their purpose to ensure the health and safety of consumers through regulation of drugs being released for clinical use. Otherwise, these core concepts of drug research have withstood the test of time, and in conjunction with advanced biological assessments remain the foundation of modern drug design.

Within the Keillor Research Group, one of our main focuses is expanding on the fundamental knowledge of covalent enzyme inhibitors.

1.2 Enzyme inhibition

Enzymes are ubiquitous proteins, containing an active site used for binding a substrate or reactant and converting it into products. These active sites are usually specific to the enzyme and the process it catalyzes, being modified once the substrate is bound and returning to its original state after the products are released. These enzyme-catalyzed reactions are prone to covalent inhibition by small molecules that prevent the formation of products, and many drugs in disease treatment take advantage of this propensity.

Covalent inhibitors are divided into two main classes – reversible and irreversible. In all cases, inhibitors take advantage of weaker non-covalent interactions such as van der Waals forces, hydrophobic interactions, electrostatic interactions, and hydrogen-bonding to bind and correctly orient itself inside of an enzyme's active site.[3] These non-covalent interactions are quite easily disrupted, allowing for the easy dissociation of enzyme and inhibitor. Reversibility (or lack thereof) is determined through the covalent bond that is formed between the inhibitor and a nucleophilic amino acid residue inside of the target active site.

1.2.1 Covalent reversible inhibitors

Reversible inhibitors form covalent bonds that are readily reversible, and once cleaved, the enzyme regains its functionality. Reversibility can be determined experimentally through methods such as dialysis, substrate competition, or allowing for long incubation times.[3] Because the

covalent bond is readily reversible, an equilibrium will be formed between the bound and unbound states of the enzyme.

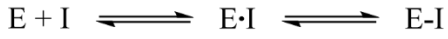

Scheme 1.1. Formation of non-covalent complex between the enzyme and inhibitor (E·I) and subsequent covalent bond formation (E-I) that is readily reversible.

1.2.2 Covalent irreversible inhibitors

Irreversible inhibitors employ the same non-covalent interactions in order to first bind a target enzyme binding pocket and properly orient themselves within it. The difference being that the covalent bond that is then formed between inhibitor and a nucleophilic residue within the active site is not easily cleaved, resulting in the permanent inactivation of the enzyme.

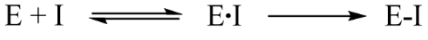

Scheme 1.2. Formation of non-covalent complex (E·I) between the enzyme and inhibitor and subsequent irreversible covalent bond formation (E-I).

1.3 Targeted covalent inhibitors (TCIs)

Targeted covalent inhibitors (TCIs) are irreversible enzyme inhibitors, designed to first bind to the targeted protein reversibly with high affinity and selectivity, then covalently react with a specific nucleophilic residue in or near the binding site. They have two major components to their design – the scaffold, responsible for initial binding, and the electrophilic warhead, responsible for covalent modification.

1.3.1 TCI Design Strategies

Conventional strategies for the development of TCIs take an existing scaffold from a known reversible inhibitor, modifying the section of the inhibitor that aligns closest to the chosen nucleophilic target (through molecular docking) to include an electrophilic moiety, serving as the 'warhead'.[3,4] Another approach employs an electrophilic fragment-based design, screening many small 'warhead' fragments and selecting only the most reactive to perform further scaffold development.[5–8] However, these methods of development leave much to be desired in the way of tuning the electrophilic warhead to generate an optimal balance between stability and reactivity.

Generally, the biggest consideration for the warhead design surrounds the required geometry and orientation for covalent bond formation. Through small changes in the scaffold and modification of the warhead this has been achieved to a degree of success[4], but those few considerations are the main factors employed in the modification of these warhead used for each inhibitor.[4] In addition to achieving optimal geometry and orientation in respect to the nucleophilic target, the intrinsic reactivity of the warhead could lend itself to ensure optimal performance of the TCI.

1.3.2 Potential targets

TCIs are typically designed to react with a nucleophilic amino acid residue located near the enzyme's binding site. Cysteine (Cys) residues contain a redox-sensitive thiol, shown in Figure 1, and are very commonly found in binding sites of enzymes.[9] Because of this, they make for an excellent nucleophilic target and as such have been exploited in the development of new irreversible enzyme inhibitors.[10–18]

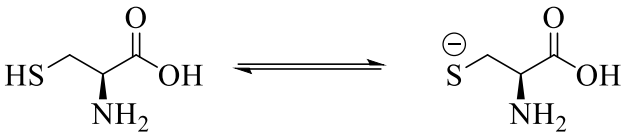

Figure 1.1. Redox-sensitive cysteine residue.

An optimized TCI achieves a fine balance between stability in the presence of differing nucleophiles, and reactivity once the scaffold non-covalently binds to the desired enzyme pocket. However, to reach this goal, the mechanism behind these electrophiles must first be well understood.

1.4 Electrophilic warheads

Electrophilic warheads may be comprised of numerous electrophilic moieties capable of covalently binding to the nucleophilic target. Some common examples used in the development of inhibitors through structure-activity relationship (SAR) studies include acrylamides[3,12,16,18–24], aldehydes[3,12,19], alkynes[3,18,19,21,25], carbamates[3,16,18,20,24,26,27], chloroacetamides[18,22,28–30], and maleimides[18,19,21,31] (Figure 2) among many others. The studies contained herein focus on two classes of electrophilic warheads – acrylamides and chloroacetamides.

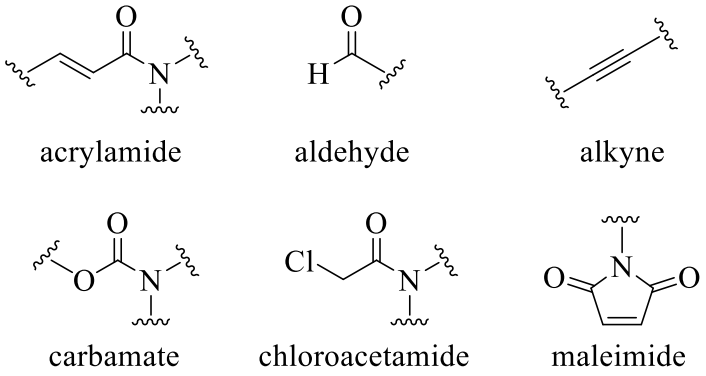

Figure 1.2. General electrophilic warheads used in the development of enzyme inhibitors.

1.4.1 Acrylamides

Acrylamides are one of the most common electrophilic warheads used in the development of TCIs, specifically for kinase inhibitors used in cancer treatments.[32] Although they are widely used in clinical applications – i.e. poseltinib[33,34], spebrutinib[35], ibrutinib[36,37], zanubrutinib[38,39], afatinib[40], neratinib[41], sotorasib[42], adagrasib[43] – and many more are being highly pursued in different phases of clinical trials – i.e. osimertinib[44–46], rociletinib[45,47] – few studies have been performed on the acrylamide warhead's intrinsic reactivity (Figure 3).

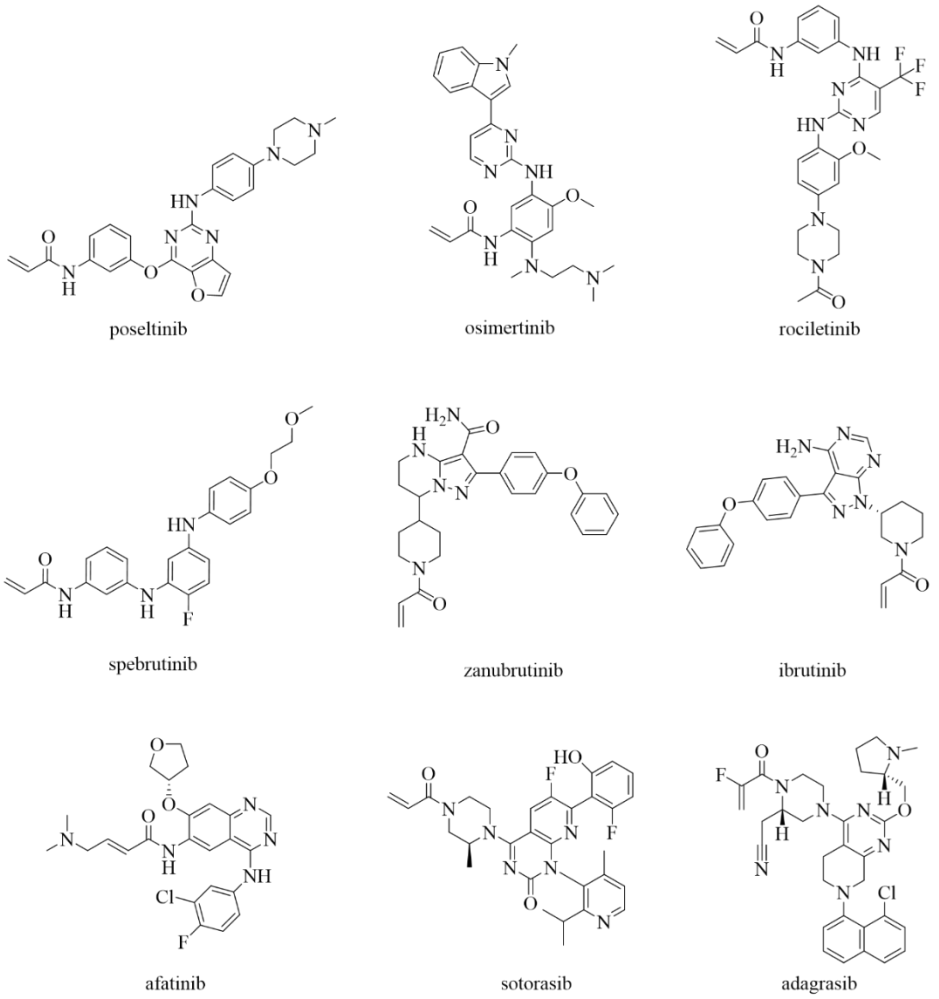

Figure 1.3. Examples of irreversible enzyme inhibitors containing the acrylamide electrophilic warhead.

1.4.2 Chloroacetamides

Chloroacetamides are another common electrophilic group well known to readily react with thiols under aqueous conditions.[48] In a study by Padhariya *et al.,* the chloroacetamide warhead was the focus of inhibitor development against cancer stem cells.[49] Their study concluded with multiple hit compounds showing inhibitory activity against cancer stem cells in both breast and prostate cancer, while having little to no toxicity when tested against normal cells. Although chloroacetamides have shown to be adequately stable under physiological aqueous conditions, biostability concerns prevent their exploitation *in vivo*,[32,50] and thus they have better lent themselves as functional cysteine-reactive probes.[21,51] Chlorofluoroacetamide has been explored as an alternative in an attempt to increase biostability, but has shown lower overall reactivity and potential interference with binding affinity, compared to the unsubstituted chloroacetamide.[22,52] Despite biostability challenges, unsubstituted α-chloroacetamide derivatives are still included in inhibitor screenings against their acrylamide counterparts and continue to be identified as lead compounds.[28,32,49,52–54] RSL3 and ML162 (Figure 4) are some of the most potent GPx4 inhibitors, both featuring a chloroacetamide warhead, proving effective in inducing ferroptosis in cancer cells.[55] Currently they are used solely in ongoing research and have not been approved for clinical use. These examples, along with the continuation of their inclusion in TCI development, highlight the importance of these warheads in the future of drug discovery.

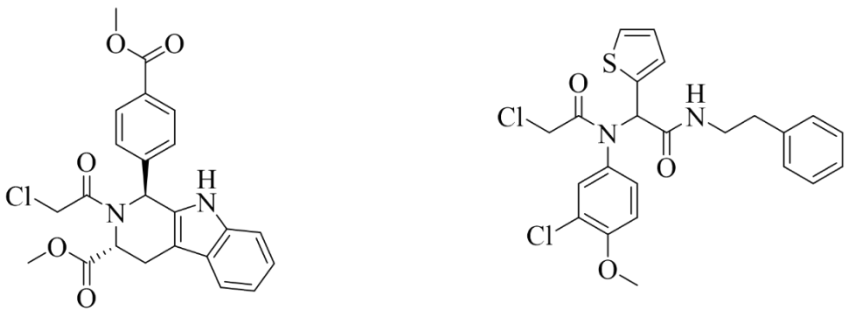

Figure 1.4. Examples of inhibitors under investigation containing the chloroacetamide warhead.

1.5 Methodology

The work presented in this thesis is focused on the study of the mechanism of thiol addition to electrophilic warhead derivatives of interest. Our approach included independently varying specific parameters of the experiment and observing their effect on the kinetic rates. These parameters include the pK_a of the nucleophiles, temperature of incubation, ionic strength of reaction buffer, and the use of a deuterated reaction buffer. The results provide information about the sensitivity to thiol nucleophilicity, enthalpy and entropy of activation, change in charge density from the ground state to the transition state, and the transfer of proton in the rate-limiting step, respectively. The change in observed kinetic rates provides valuable information about the rate limiting transition state and the role of the reactive participants within.

1.5.1 Quantification

The disappearance and appearance of compounds throughout the studies shown below were monitored through a discontinuous assay by high-performance liquid chromatography (HPLC). This is the preferred method as it allows for initial separation of compounds in the reaction mixture and then precise quantification of these compounds over time. In this way, we were able to measure

the observed kinetic rate constant. The compounds are quantified using ultraviolet-visible spectroscopy (UV-Vis), monitoring the 214 and 254 nm wavelengths, integrating the area under the curve for the respective peaks at 214 nm and plotting these data for the disappearance of starting electrophile to formed adduct over time.

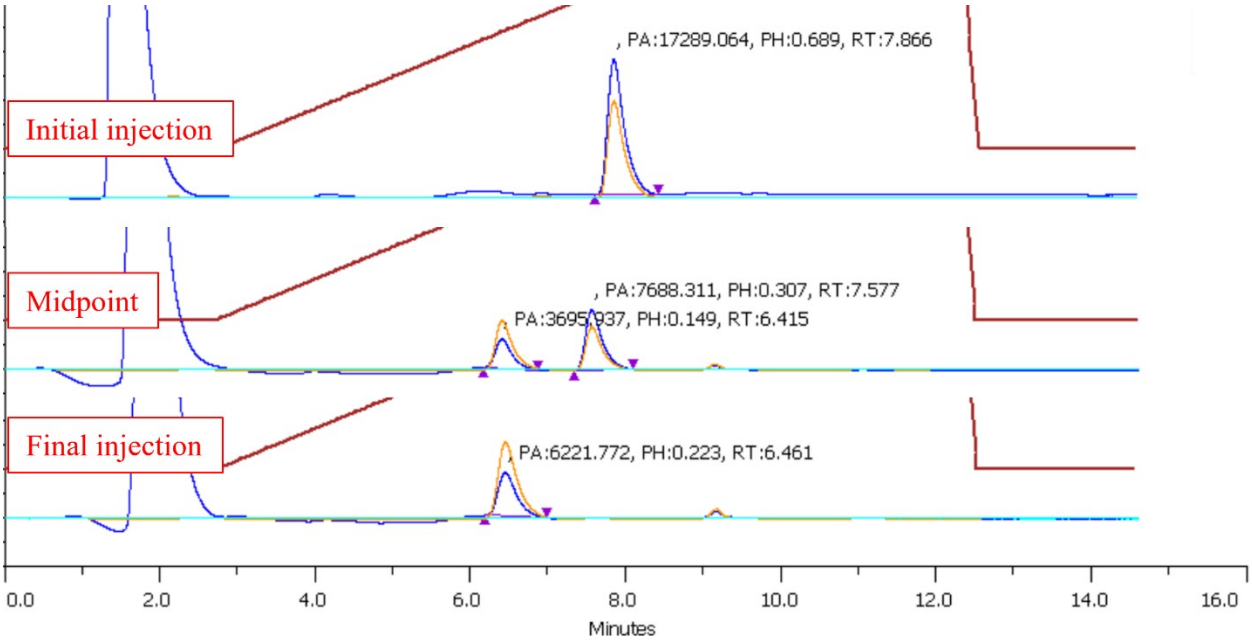

Figure 1.5. Example of high-performance liquid chromatography (HPLC) chromatograph, showing the separation of key reactants and products over the course of the reaction, and their quantification over time using the integrated area under the curve (AUC).

1.5.1.1 Advantages

Monitoring by HPLC provided many advantages to these studies, including the ability to pre-program the time points for aliquots using the liquid handler capabilities, as well as maintaining consistency of aliquots with minimal deviations in volume. Being able to monitor not only the disappearance of the starting electrophile, but the appearance of the adduct as well, allows us to ensure that the consumption of electrophile is proportional to

the formation of adduct. In addition, it allows us to confirm that no unexpected by-products formed over the course of the reaction.

1.5.1.2 Disadvantages

While the advantages of HPLC are numerous, a few disadvantages include the lengthy method development process to ensure baseline separation of all species in the reaction mixture, heavy maintenance of the equipment and high consumption of solvents.

1.5.2 Product studies

Product studies were initially performed to confirm the identity of the thiol-adducts in the studies presented below. In order to achieve this, the reaction was run in an NMR tube using deuterated buffer, and the appearance/disappearance of proton signals were monitored over the course of the reaction. Once deemed complete, a final ^{1}H-NMR spectrum was recorded and analyzed to confirm the final structure of the adduct, and an aliquot was injected on the HPLC to further assess purity. The peak corresponding to the thiol-adduct was then collected and analyzed by high-resolution mass spectroscopy.

1.5.3 Brønsted-type plot

Brønsted-type plots confer invaluable information regarding the correlation between reactivity and the basicity of nucleophiles in regard to an electrophile. Plotting the log of the second order rate constants against the pK_a of the conjugate acid of the nucleophile affords a linear relationship wherein the slope is equivalent to the sensitivity factor, β_{Nuc}. The term β_{Nuc} is indicative of the sensitivity of nucleophilic attack on the basicity of the nucleophile and ranges from 1 to 0. A β_{Nuc} value of 1 indicates that the nucleophilicity is highly linked to basicity, i.e., an electrophile will

react faster with a more basic nucleophile whereas a value of less than 1 correlates to a diminished sensitivity to nucleophile basicity, i.e., an electrophile will react at a similar rate with two nucleophiles regardless their pK_a. The degree of the slope can also be correlated to the degree of bond formation present at the rate limiting transition state – with a shallow slope indicating very little bond formation present and a steep slope indicating a high degree of bond formation.

(1) $$\log(k) = \beta_{Nuc} pK_a + \log(C')$$

The Brønsted-type plot is an invaluable tool to correlate nucleophilicity with pK_a, and can also be used to correlate nucleofugality with pK_a (β_{LG}). This property of the Brønsted-type plot is utilized in Chapter 4 of this thesis, where the leaving group's ability effect on reaction rate is explored within the α-haloacetamide derivatives. In this case, the pK_a plotted on the x-axis is that of the conjugate acid of the leaving group, and on the y-axis is plotted the log value of the second order rate constants. It is generally expected that the leaving group ability would increase with a lower pK_a, affording a negative slope. In this plot, a steep slope would indicate a high degree of bond cleavage of the leaving group at the rate limiting transition state, and a shallow slope would likewise indicate moderate or little bond cleavage.

(2) $$\log(k) = \beta_{LG}(pK_a) + \log(C)$$

1.5.4 Temperature effects

It is known that the rate constant of a reaction increases exponentially with an increase in temperature, consistent with both of the Arrhenius and Eyring parameters. Both Arrhenius and Eyring plots are used in the course of the studies below; however, a higher importance is placed on the results afforded from the Eyring plot. This is due to the fact that the Arrhenius law was

derived empirically, based on the observation that the rates of reactions increase exponentially with temperature (Eqn 3). Because of this, the Arrhenius equation does not take into account any mechanistic considerations, only considering the macroscopic rate constant for a particular overall reaction.[57] The Eyring equation analyzes a microscopic rate constant for a single step conversion of a reactant to product.

The Arrhenius plot of ln$k$ vs. 1/T following Eqn 3 affords a straight line that uses the pre-exponential factor (A) and the activation energy (E_a). The pre-exponential factor is found through the y-intercept, where 1/T=0, and the activation energy found through the slope of the plotted line ($-E_a/R$). The activation energy, by definition, is the minimum kinetic energy that reactants require in order to form products.[57] In this way, the slope obtained from experimental data gives important information on the degree of dependency of the reaction on temperature. Meaning, the higher the activation energy, the stronger the dependence on temperature, otherwise described as the steepness of the slope.

(3) $$k = A^{(-\frac{E_a}{RT})}$$

(4) $$k = \kappa(\frac{k_B T}{h})^{(-\frac{\Delta G^{\ddagger}}{RT})}$$

(5) $$\ln\left(\frac{kh}{\kappa k_B T}\right) = -\left(\frac{\Delta H^{\ddagger}}{R}\right)\left(\frac{1}{T}\right) + \Delta S^{\ddagger}/R$$

With the Eyring equation, we are able to solve for the enthalpy and entropy of activation parameters ($\Delta H^{\ddagger}$ and $\Delta S^{\ddagger}$, respectively), with the assumption that they do not change with a change in temperature. The Eyring equation (Eqn 4) can be rearranged to plot a straight line (Eqn 5). This can be plotted, assuming $\kappa = 1$, with an x-axis of 1/T and y-axis of $\ln(kh/\kappa k_B T)$. From the linear equation, the slope of this line is equivalent to $-\Delta H^{\ddagger}/R$ and the y-intercept is $\Delta S^{\ddagger}/R$ and we are thus

able to solve for the entropy and enthalpy parameters of activation. The magnitude of these values affords important information about the changes in entropy and enthalpy moving from the ground state to the transition state. In this way, a large negative entropy of activation would indicate a highly ordered transition state, probably due to a bimolecular association, and a positive value indicates increasing disorder, such as what we would observe for bond cleavage.

1.5.5 Ionic strength effects

The ionic strength (μ) effect studied herein explores how ionic species present in solution affect the rate of reaction.[57] The salts dissolved in the aqueous solution dissociate into their cationic and anionic counterparts, where the cationic species stabilize a negatively charged substrate and the anionic species stabilize the positively charged species. In this way, a higher salt concentration present in solution better stabilizes charged species. Observing the effect on the reaction rates while decreasing the ionic strength of the aqueous medium affords invaluable information on the change in charge density from the ground state moving to the transition state.[57] A decrease in reaction rate corresponding to an increase in ion presence in solution would indicate that there is a larger ionic stabilization of the ground state relative to the transition state – i.e. the charges on the reactants become dispersed as they move from the ground state to the transition state. Whereas an increase in reaction rate would indicate the reverse – the charge becoming less dispersed (more localized) moving from the ground to transition state.

To observe this effect, the corrected second order rates were plotted against μ and the resulting sign of the slope was interpreted.

1.5.6 Solvent kinetic isotope effects (SKIE)

The isotope effect is measured during a mechanistic study in order to determine if the formation/cleavage of a particular bond is implicated in the rate limiting step of the reaction. This effect is expressed as a ratio of rate constants, where the numerator is the normal rate (k_H) and the denominator is the rate observed in the deuterated solvent (k_D) – k_H/k_D.

To measure the solvent kinetic isotope effect (SKIE) in the studies detailed in chapters 2-3, one thiol-addition reaction was chosen from the series of those performed and repeated in the same manner with the exception of solvent. The buffer was instead prepared using D_2O to serve as the source of deuterium, probing the protonation step in the thiol-addition mechanism. Involving the cleavage of a hydrogen-oxygen bond from H_2O and subsequent formation of a carbon-hydrogen bond on the thiol-adduct, a primary kinetic isotope effect is expected (X-H/X-D). The resulting ratio of rate constants gives valuable information on the magnitude of the primary kinetic isotope effect. A ratio of 1 would indicate that the bond in question is not implicated in the rate limiting transition state, or that the effect is too small to be accurately measured. A result of greater than 1 would therefore indicate a normal isotope effect where the bond is implicated, and a value of less than 1 would indicate an inverse effect.

The ratio of k_H/k_D was measured and interpreted in the mechanistic studies of the acrylamide series as described in the chapters below.

1.6 Previous Work

Surprisingly, few studies have previously been reported on the intrinsic reactivity of irreversible enzyme warhead derivatives, with fewer still probing the mechanism through which they undergo thiol-addition. The previous studies pertaining to each individual warhead derivative are discussed in more detail in each individual chapter (see below).

All previous studies determining reaction rates focus on glutathione (GSH) as the model nucleophile. This is a reasonable model thiol due to the fact that it's a tripeptide and therefore able to mimic a slightly conformationally hindered nucleophilic cysteine residue. It is also found in relatively high intracellular concentrations (5-10 mM).[4] GSH has a pK_a value of 8.7[56]; however, the pK_a of a target cysteine residue inside of an enzyme active site can range between values of 8-9[30] due to the surrounding environment, so it is imperative to fully characterize the reactivity profile of electrophilic warheads over a broad range of pK_a values.

1.7 Objectives

We decided to perform a mechanistic and kinetic study on a select few warhead derivatives to gain insight into their intrinsic reactivities according to the techniques mentioned above. The research towards these studies of the selected warheads is presented in the form of either submitted or published articles in the following chapters.

1.7.1 A mechanistic study of thiol addition to N-phenylacrylamide (Chapter 2)

The first study contained herein is a foray in the mechanistic study of thiol addition to *N*-phenyl acrylamide, presented below in Chapter 2.

This paper fits into the main body of the thesis, as the first publication in a series, studying the mechanism of thiol addition to differently N- substituted acrylamides. We chose to start with N-phenylacrylamide (NPA) as it is the featured warhead in the studies published by Cee *et al*.[59] and Flanagan *et al.*[5] From the previously reported data, we were able to confirm our methodology and expand upon the previously published data surrounding this warhead. Although it was the featured warhead in the manuscripts mentioned, the effect of changing the thiol was not explored. This large gap in the understanding of how the properties of the thiol (or attacking thiolate) are related to its reactivity of this warhead was one we believe needed to be filled.

1.7.2 A mechanistic study of thiol addition to N-acryloylpiperidine (Chapter 3)

Next, Chapter 3 presents the follow up to the mechanistic study on *N*- aryl acrylamides, studying the mechanism of thiol addition to *N*- alkyl and *N,N*- dialkyl substituted acrylamides.

This study, while containing data for the N-alkyl substituted acrylamide, focuses mainly on the *N,N*-dialkyl substituted acrylamide. This was due to solubility issues and unusably slow reactivity encountered throughout the study. This publication also compares the mechanisms of the alkyl substituted acrylamides to the aromatically substituted derivatives, highlighting the large difference in intrinsic reactivity between the two.

Unlike NPA that has been previously studied, probing its intrinsic reactivity to GSH and how aromatic and α,β-unsaturation substitutions could enhance or attenuate its intrinsic reactivity, *N*-acryloylpiperidine (AcrPip) has not garnered such attention. The published work contained herein aims to fill that gap in the literature and provide meaningful insight into this series of electrophilic warheads.

1.7.3 A kinetic study of thiol addition to N-phenylchloroacetamide (Chapter 4)

Chapter 4 of this thesis comprises the mechanistic study of thiol addition to *N*-phenyl chloroacetamide. This study has been accepted for publication by *Organic and Biomolecular Chemistry*.

Following the series of publications on *N*-aryl and *N*-alkyl substituted acrylamides, we decided the next logical warheads to consider are the α-halo acetamides, starting with *N*-phenyl chloroacetamide. This *N*-phenyl derivative was chosen for the ability to make a direct comparison against *N*-phenylacrylamide. Chloride was selected as the halide leaving group due to its popularity of use in current TCI development (see above).

1.7.4 Conclusions and Future Perspectives (Chapter Five)

Lastly, the final chapter will resume the overarching story linking the three articles contained in Chapters Two through Four that make up the body of this thesis. This final chapter will also outline future perspectives for the continuation of this project.

1.8 References

1 M. O. Faruk Khan, M. J. Deimling and A. Philip, *Am J Pharm Educ*, 2011, **75**, 161.

2 M. R. Montinari, S. Minelli and R. De Caterina, *Vascul Pharmacol*, 2019, **113**, 1–8.

3 A. Tuley and W. Fast, *Biochemistry*, 2018, **57**, 3326–3337.

4 M. Gehringer and S. A. Laufer, *J Med Chem*, 2019, **62**, 5673–5724.

5 M. E. Flanagan, J. A. Abramite, D. P. Anderson, A. Aulabaugh, U. P. Dahal, A. M. Gilbert, C. Li, J. Montgomery, S. R. Oppenheimer, T. Ryder, B. P. Schuff, D. P. Uccello, G. S. Walker, Y. Wu, M. F. Brown, J. M. Chen, M. M. Hayward, M. C. Noe, R. S. Obach, L. Philippe, V. Shanmugasundaram, M. J. Shapiro, J. Starr, J. Stroh and Y. Che, *J Med Chem*, 2014, **57**, 10072–10079.

6 R. M. Miller, V. O. Paavilainen, S. Krishnan, I. M. Serafimova and J. Taunton, *J Am Chem Soc*, 2013, **135**, 5298–5301.

7 K. M. Backus, B. E. Correia, K. M. Lum, S. Forli, B. D. Horning, G. E. González-Páez, S. Chatterjee, B. R. Lanning, J. R. Teijaro, A. J. Olson, D. W. Wolan and B. F. Cravatt, *Nature*, 2016, **534**, 570–574.

8 S. G. Kathman, Z. Xu and A. V. Statsyuk, *J Med Chem*, 2014, **57**, 4969–4974.

9 C. Jöst, C. Nitsche, T. Scholz, L. Roux and C. D. Klein, *J Med Chem*, 2014, **57**, 7590–7599.

10 J. Singh, R. C. Petter, T. A. Baillie and A. Whitty, *Nat Rev Drug Discov*, 2011, **10**, 307–317.

11 M. Visscher, M. R. Arkin and T. B. Dansen, *Curr Opin Chem Biol*, 2016, **30**, 61–67.

12 P. Ábrányi-Balogh and G. M. Keserű, in *Advances in Chemical Proteomics*, Elsevier, 2021, pp. 47–73.

13 M. H. Potashman and M. E. Duggan, *J Med Chem*, 2009, **52**, 1231–1246.

14 H. Kim, Y. S. Hwang, M. Kim and S. B. Park, *RSC Med Chem*, 2021, **12**, 1037–1045.

15 R. Lonsdale and R. A. Ward, *Chem Soc Rev*, 2018, **47**, 3816–3830.

16 R. Lagoutte, R. Patouret and N. Winssinger, *Curr Opin Chem Biol*, 2017, **39**, 54–63.

17 S. E. Dalton and S. Campos, *ChemBioChem*, 2020, **21**, 1080–1100.

18 R. Lonsdale, J. Burgess, N. Colclough, N. L. Davies, E. M. Lenz, A. L. Orton and R. A. Ward, *J Chem Inf Model*, 2017, **57**, 3124–3137.

19 D. A. Shannon and E. Weerapana, *Curr Opin Chem Biol*, 2015, **24**, 18–26.

20 K. M. Backus, J. Cao and S. M. Maddox, *Bioorg Med Chem*, 2019, **27**, 3421–3439.

21 J. S. Martin, C. J. MacKenzie, D. Fletcher and I. H. Gilbert, *Bioorg Med Chem*, 2019, **27**, 2066–2074.

22 D. G. Hoch, D. Abegg and A. Adibekian, *Chem Comm*, 2018, **54**, 4501–4512.

23 L. Mader, S. K. I. Watt, H. R. Iyer, L. Nguyen, H. Kaur and J. W. Keillor, *RSC Med Chem*, 2023, **14**, 277–298.

24 A. M. M. Rangaswamy, P. Navals, E. W. J. Gates, S. Shad, S. K. I. Watt and J. W. Keillor, *RSC Med Chem*, 2022, **13**, 413–428.

25 E. Badarau, Z. Wang, D. L. Rathbone, A. Costanzi, T. Thibault, C. E. Murdoch, S. El Alaoui, M. Bartkeviciute and M. Griffin, *Chem Biol*, 2015, **22**, 1347–1361.

26 K. Y. P. Apperley, I. Roy, V. Saucier, N. Brunet-Filion, S. P. Piscopo, C. Pardin, É. De Francesco, C. Hao and J. W. Keillor, *Medchemcomm*, 2017, **8**, 338–345.

27 K. King, A.-T. Hauser, J. Melesina, W. Sippl and M. Jung, *Molecules*, 2018, **23**, 321.

28 A. K. Ghosh and M. Brindisi, *J Med Chem*, 2015, **58**, 2895–2940.

29 M. Sato, H. Fuchida, N. Shindo, K. Kuwata, K. Tokunaga, G. Xiao-Lin, R. Inamori, K. Hosokawa, K. Watari, T. Shibata, N. Matsunaga, S. Koyanagi, S. Ohdo, M. Ono and A. Ojida, *ACS Med Chem Lett*, 2020, **11**, 1137–1144.

30 K. T. Barglow and B. F. Cravatt, *Chem Biol*, 2004, **11**, 1523–1531.

31 E. Weerapana, G. M. Simon and B. F. Cravatt, *Nat Chem Biol*, 2008, **4**, 405–407.

32 D. Halim, K. Caron and J. W. Keillor, *Bioorg Med Chem Lett*, 2007, **17**, 305–308.

33 N. Shindo and A. Ojida, *Bioorg Med Chem*, 2021, **47**, 116386.

34 J. Y. Byun, Y. T. Koh, S. Y. Jang, J. W. Witcher, J. R. Chan, A. Pustilnik, M. J. Daniels, Y. H. Kim, K. H. Suh, M. D. Linnik and Y. M. Lee, *Sci Rep*, 2021, **11**, 1–14.

35 M. C. Genovese, A. Spindler, A. Sagawa, W. Park, A. Dudek, A. Kivitz, J. Chao, L. S. M. Chan, J. Witcher, W. Barchuk and A. Nirula, *J Rheum*, 2021, **48**, 969–976.

36 P. H. Schafer, A. J. Kivitz, J. Ma, S. Korish, D. Sutherland, L. Li, A. Azaryan, J. Kosek, M. Adams, L. Capone, E. M. Hur, D. R. Hough and G. E. Ringheim, *Rheumatol Ther*, 2020, **7**, 101–119.

37 J. C. Byrd, R. R. Furman, S. E. Coutre, I. W. Flinn, J. A. Burger, K. A. Blum, B. Grant, J. P. Sharman, M. Coleman, W. G. Wierda, J. A. Jones, W. Zhao, N. A. Heerema, A. J. Johnson, J.

Sukbuntherng, B. Y. Chang, F. Clow, E. Hedrick, J. J. Buggy, D. F. James and S. O'Brien, *N Engl J Med*, 2013, **369**, 32–42.

38 J. A. Woyach, R. R. Furman, T.-M. Liu, H. G. Ozer, M. Zapatka, A. S. Ruppert, L. Xue, D. H.-H. Li, S. M. Steggerda, M. Versele, S. S. Dave, J. Zhang, A. S. Yilmaz, S. M. Jaglowski, K. A. Blum, A. Lozanski, G. Lozanski, D. F. James, J. C. Barrientos, P. Lichter, S. Stilgenbauer, J. J. Buggy, B. Y. Chang, A. J. Johnson and J. C. Byrd, *N Engl J Med*, 2014, **370**, 2286–2294.

39 Y. Y. Syed, *Drugs*, 2020, **80**, 91–97.

40 C. S. Tam, Y. C. Ou, J. Trotman and S. Opat, *Expert Rev Clin Pharmacol*, 2021, **14**, 1329–1344.

41 Z. Yang, A. Hackshaw, Q. Feng, X. Fu, Y. Zhang, C. Mao and J. Tang, *Int J Cancer*, 2017, **140**, 2805–2819.

42 R. Paranjpe, D. Basatneh, G. Tao, C. De Angelis, S. Noormohammed, E. Ekinci, S. Abughosh, R. Ghose and M. V. Trivedi, *Annals of Pharmacotherapy*, 2019, 53, 612–620.

43 E. C. Nakajima, N. Drezner, X. Li, P. S. Mishra-Kalyani, Y. Liu, H. Zhao, Y. Bi, J. Liu, A. Rahman, E. Wearne, I. Ojofeitimi, L. T. Hotaki, D. Spillman, R. Pazdur, J. A. Beaver and H. Singh, *Clin Cancer Res*, 2022, **28**, 1482–1486.

44 S. Dhillon, *Drugs*, 2023, **83**, 275–285.

45 Y.-L. Wu, M. Tsuboi, J. He, T. John, C. Grohe, M. Majem, J. W. Goldman, K. Laktionov, S.-W. Kim, T. Kato, H.-V. Vu, S. Lu, K.-Y. Lee, C. Akewanlop, C.-J. Yu, F. de Marinis, L. Bonanno, M. Domine, F. A. Shepherd, L. Zeng, R. Hodge, A. Atasoy, Y. Rukazenkov and R. S. Herbst, *N Engl J Med*, 2020, **383**, 1711–1723.

46 L. V. Sequist, Z. Piotrowska, M. J. Niederst, R. S. Heist, S. Digumarthy, A. T. Shaw and J. A. Engelman, *JAMA Oncol*, 2016, **2**, 541–543.

47 A. L. Koch, P. J. Vellanki, N. Drezner, X. Li, P. S. Mishra-Kalyani, Y. L. Shen, H. Xia, Y. Li, J. Liu, J. F. Zirkelbach, E. Palazov, A. Gamarian, Q. Choo, A. Girčys, U. P. Rohr, N. Fesenko, D. Spillman, R. Pazdur, J. A. Beaver and H. Singh, *Clin Cancer Res*, 2021, **27**, 6638–6643.

48 L. V. Sequist, J.-C. Soria, J. W. Goldman, H. A. Wakelee, S. M. Gadgeel, A. Varga, V. Papadimitrakopoulou, B. J. Solomon, G. R. Oxnard, R. Dziadziuszko, D. L. Aisner, R. C. Doebele, C. Galasso, E. B. Garon, R. S. Heist, J. Logan, J. W. Neal, M. A. Mendenhall, S. Nichols, Z. Piotrowska, A. J. Wozniak, M. Raponi, C. A. Karlovich, S. Jaw-Tsai, J. Isaacson, D. Despain, S. L. Matheny, L. Rolfe, A. R. Allen and D. R. Camidge, *N Engl J Med*, 2015, **372**, 1700–1709.

49 F. Dickens, *Biochem J*, 1933, **27**, 1141–51.

50 K. N. Padhariya, M. Athavale, S. Srivastava and P. S. Kharkar, *Drug Dev Res*, 2020, **81**, 356–365.

51 J. Bi, S. Yang, L. Li, Q. Dai, N. Borcherding, B. A. Wagner, G. R. Buettner, D. R. Spitz, K. K. Leslie, J. Zhang and X. Meng, *Cell Death Dis*, 2019, **10**, 682.

52 R. D. Cole, W. H. Stein and S. Moore, *J Biol Chem*, 1958, **233**, 1359–1363.

53 N. Shindo, H. Fuchida, M. Sato, K. Watari, T. Shibata, K. Kuwata, C. Miura, K. Okamoto, Y. Hatsuyama, K. Tokunaga, S. Sakamoto, S. Morimoto, Y. Abe, M. Shiroishi, J. M. M. Caaveiro, T. Ueda, T. Tamura, N. Matsunaga, T. Nakao, S. Koyanagi, S. Ohdo, Y. Yamaguchi, I. Hamachi, M. Ono and A. Ojida, *Nat Chem Biol*, 2019, **15**, 250–258.

54 L. A. Bateman, T. B. Nguyen, A. M. Roberts, D. K. Miyamoto, W. M. Ku, T. R. Huffman, Y. Petri, M. J. Heslin, C. M. Contreras, C. F. Skibola, J. A. Olzmann and D. K. Nomura, *Chem Comm*, 2017, **53**, 7234–7237.

55 L. Wang, X. Chen, C. Yan, *Genes Dis,* 2022, **9**, 334–346.

56 E. A. Grossman, C. C. Ward, J. N. Spradlin, L. A. Bateman, T. R. Huffman, D. K. Miyamoto, J. I. Kleinman and D. K. Nomura, *Cell Chem Biol*, 2017, **24**, 1368-1376.e4.

57 E. V Anslyn and D. A. Dougherty, *Modern Physical Organic Chemistry*, University Science Books, 2005.

58 A. K. Mitra and M. M. Narurkar, *Int J Pharm*, 1986, **28**, 119–124.

59 V. J. Cee, L. P. Volak, Y. Chen, M. D. Bartberger, C. Tegley, T. Arvedson, J. McCarter, A. S. Tasker and C. Fotsch, *J Med Chem*, 2015, **58**, 9171–9178.

Chapter 2 : A mechanistic study of thiol addition to *N*-phenylacrylamide

Sarah K. I. Watt[a], Janique G. Charlebois[a], Christopher N. Rowley[b], Jeffrey W. Keillor[a]*

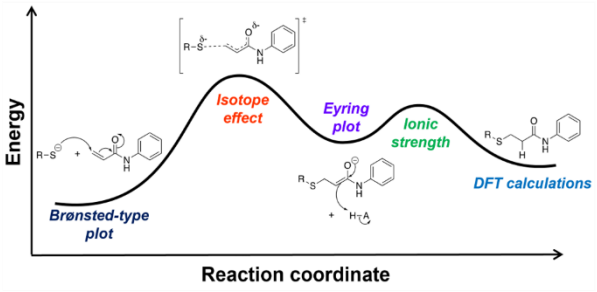

2.1 Statement of Contributions

This manuscript is a collaborative effort between all authors listed in the publication. SKIW contributed to the conceptualization, methodology and experimentation (synthesis, characterization, intrinsic reactivity), and writing. JGC contributed to the methodology and experimentation (intrinsic reactivity) as an undergraduate student under the supervision of SKIW. CNR contributed to the methodology and experimentation (molecular modelling) as well as writing. Finally, JWK contributed to the conceptualization, funding acquisition, supervision, interpretation, and writing. All authors reviewed and edited the work prior to publication.

Reproduced from S. K. I. Watt, J. G. Charlebois, C. N. Rowley, & J. W. Keillor. A mechanistic study of thiol addition to *N* -phenylacrylamide. *Organic & Biomolecular Chemistry*, 2022, **20**, 8898–8906 [1] with permission from the Royal Society of Chemistry.

2.2 Abstract

Cysteine (Cys) residues contain a redox-sensitive thiol and are commonly found in enzyme active sites. In recent years, the presence of a reactive thiolate group on a protein has been exploited in the development of irreversible enzyme inhibitors as therapeutic agents. Many targeted covalent inhibitors (TCIs) are designed to covalently react with a specific Cys residue on a target protein active site, irreversibly modifying the target and inhibiting its normal function. The electrophilic warhead most commonly used in this way is the acrylamide functional group. Although the acrylamide group is well known for its ability to undergo thiol-addition reactions, very few studies have been conducted to elucidate the detailed mechanism of this reaction, which inspired us to conduct a thorough kinetic investigation. First, we developed a robust kinetic assay to accurately monitor reaction progress between *N*-phenylacrylamide (NPA) and a small library of alkyl thiols having widely varying pK_a values. This allowed us to construct a Brønsted-type plot for the thiol addition reaction, revealing a β_{nuc}^{RS-} value of 0.07 ± 0.04. We also studied the solvent kinetic isotope effects (SKIEs), pH dependence, and temperature dependence of the reaction, which showed that reaction has a relatively large negative $\Delta S^{\ddagger}$, and a small $\Delta H^{\ddagger}$. Computational studies provided a structure for the transition state that is consistent with the experimental data. All of these data are consistent with rate-limiting nucleophilic attack, followed by rapid protonation of the enolate, corresponding to the microscopic reverse of the $E1_{cb}^{rev}$ elimination mechanism.

Keywords: acrylamide, thiol, mechanism, Brønsted plot

2.3 Introduction

Cysteine (Cys) residues contain a redox-sensitive thiol group and are often found in enzyme active sites. In recent years, the presence of reactive thiolate groups has been exploited in the development of irreversible enzyme inhibitors.[2] These targeted covalent inhibitors (TCIs) are typically designed to first bind to the target protein with high affinity and selectivity, before covalently reacting with a specific Cys residue in or near a binding site, irreversibly modifying their targets and inhibiting their normal function.

Through targeted design and optimization, effective TCIs can be developed to enhance selectivity and reactivity with their specific enzyme targets. This requires the optimisation of an affinity binding moiety, attached to a reactive electrophilic warhead whose function is to react with an adjacent nucleophilic Cys residue, thereby permanently anchoring the inhibitor in place. A key breakthrough in the design of such inhibitors is the use of warheads with attenuated reactivity, such that they only react with a target Cys residue after they are selectively bound by the target protein. One of the most common warheads that has been used in this way is the acrylamide group[3], with the *N*-phenyl substituted derivative widely used. For example, poseltinib[4,5] and spebrutinib[6] are irreversible inhibitors undergoing Phase 2 clinical trials targeting Bruton's tyrosine kinase (BTK). Osimertinib[7,8] and rociletinib[7,9] are both irreversible inhibitors targeting Epidermal-Growth Factor Receptor (EGFR) tyrosine kinase. Osimertinib has been approved for clinical application while rociletinib is currently under investigation (Figure 1).

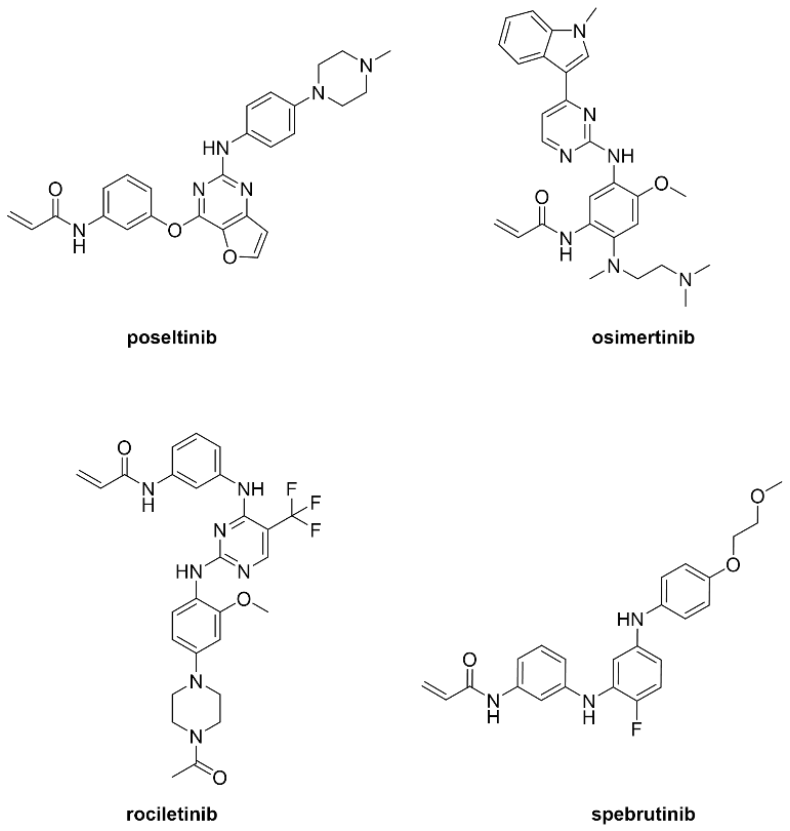

Figure 2.1. Examples of irreversible inhibitors bearing an *N*-phenylacrylamide warhead.

Acrylamides are generally well known for their ability to undergo thiol-addition reactions, but despite their broad application in this context, very few studies have been conducted to elucidate their detailed reaction mechanism. Although recent studies by Cee *et al*. have clearly demonstrated the dependence of reaction rates on *N*-phenyl and α,β-unsaturation substituents, the mechanism of the thiol addition was not explored.[3,10] To address this, we investigated the reaction of the electrophilic *N*-phenylacrylamide (NPA) in aqueous buffer (Scheme 1), with several different alkyl thiols that were chosen to cover a range of thiol pK_a values. In this way these thiols mimic Cys residues having widely varied acidity in enzyme binding sites and allow us to probe the sensitivity of the reaction rate to thiolate nucleophilicity.

For the purpose of this study, we proposed three different hypotheses for potential reaction mechanisms. The first consists of concerted nucleophilic attack of the negatively charged sulphur of the thiolate and protonation of the alpha carbon. The second involves the stepwise nucleophilic attack of the thiolate, followed by rapid protonation. Lastly, the third proposes the stepwise initial protonation followed by nucleophilic attack of the thiolate.

A pH-rate profile was constructed to determine the protonation state of the reactive species. Solvent kinetic isotope effects were studied to determine whether a proton is in flight at the rate-limiting transition state. Temperature effects were studied to measure the enthalpy and entropy of activation, as well as ionic strength effects to determine the change in electronic charge at the rate-limiting transition state. These kinetic data were also complemented with DFT computations. All of these lines of evidence were then accounted for in a cohesive proposed mechanism.

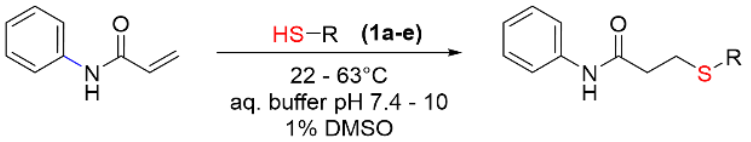

Scheme 2.1. General thiol addition reaction conditions where R represents the five alkyl thiols used in the study.

2.4 Results and Discussion

2.4.1 Product studies

NPA was prepared by adding a solution of acryloyl chloride dropwise to a stirred solution of aniline and triethylamine (see Experimental). The reactions between alkyl thiols and NPA were monitored by HPLC, following the disappearance of the acrylamide and formation of the adduct (see below). To confirm that the observed product corresponded to the expected thiol-addition adduct, independent experiments were performed by both NMR and mass spectroscopy.

First, a reaction of NPA and 3-mercaptopropionic acid (MPA) was performed in deuterated buffer in an NMR tube. ^{1}H-NMR spectra were obtained over the course of the reaction to monitor the disappearance of the acrylamide vinyl proton signals and displacement of the MPA signals (Figure 2). A final ^{1}H-NMR spectrum of the adduct was taken, as well as a COSY 2D spectrum, to confirm the coupling between the proton signals in the adduct (see ESI). All of these spectrometric analyses confirm the structure of the expected thiol-addition product. An aliquot of this reaction mixture was removed, after sufficient adduct had formed, and injected on the HPLC. The elution time of this peak corresponded with that of the product peak formed during kinetic runs (see below). Finally, the product peak was also collected and analysed by high resolution mass spectrometry, confirming that the mass corresponds to that of the expected thiol-addition adduct.

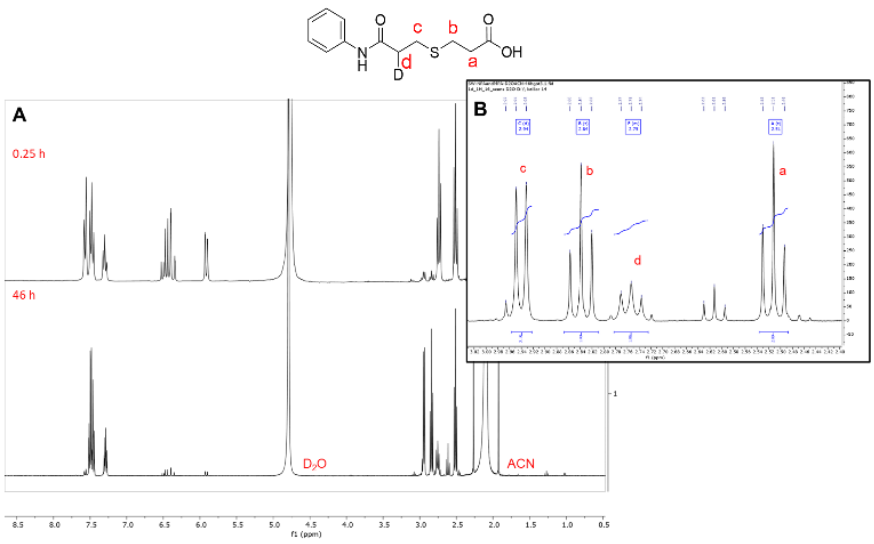

Figure 2.2. (A) ^{1}H-NMR spectra recorded over the course of the thiol-addition of MPA to NPA to monitor the disappearance of the vinyl acrylamide signals and the chemical shift observed of the MPA signals. **(B)** Expanded section of the ^{1}H-NMR spectrum of the adduct, showing the integrations and proton assignments for the thiol-acrylamide adduct.

2.4.2 Kinetic studies by HPLC

For this study, five alkyl thiols were chosen with pK_a values ranging from 7.8 to 10.3 (Table 1). The kinetic thiol-addition reactions were run in aqueous buffer, using 1% v/v DMSO as a co-solvent to maintain solubility of all species throughout the study (Scheme 1).

Reaction rate constants were measured under pseudo-first order conditions, with thiol in great excess and the acrylamide as limiting. This approach was chosen to minimize the effect of slow thiol oxidation, and effectively eliminated the need to use a reducing agent such as TCEP, which is also known to react readily with acrylamides.[11] The stability of NPA in aqueous buffer was confirmed over the course of 24 hours, which is as long as the longest reactions followed, allowing us to attribute the disappearance of NPA over this time as being solely due to its reaction with the

thiols studied. For thiols having higher pK_a values, reactions were run at higher pH, allowing pseudo-first order rate constants to be measured within this same time frame.

Table 2.1. Structures, names and literature pK_a values for thiols **1a-e**.

Thiol	Structure	Name	pK_a
1a	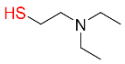	*N,N*-diethylcysteamine (DEC)	7.8[11]
1b	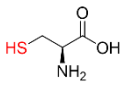	L-cysteine (Cys)	8.3[12,13]
1c	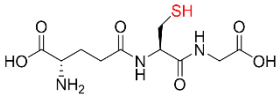	Glutathione (GSH)	8.7[12]
1d	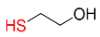	β-mercaptoethanol (BME)	9.6[13]
1e	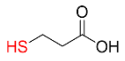	3-mercaptopropionic acid (MPA)	10.3[13]

Reaction progress was monitored according to both the disappearance of acrylamide and the formation of the acrylamide-thiol adduct over the course of at least 5-6 half-lives (Figure 3) by reverse phase HPLC. The reactions were run at room temperature in HPLC vials, sealed with a pre-slit screw cap and placed in the HPLC autosampler tray. The length of run and mobile phase gradient (consisting of milliQ water + 0.1% TFA and acetonitrile + 0.1% TFA) used for each reaction were adjusted based on the polarities of the adducts, in order to achieve complete separation of reactants and products (see Table S1, ESI). Aliquots were taken every 15-20 min,

depending on the separation method, and the proportions of acrylamide and adduct were quantified by UV at 214 nm using the integrated area under the curve (AUC) for each respective peak.

The AUC corresponding to acrylamide and adduct were plotted against time and fitted to a mono-exponential equation to afford the pseudo-first order rate constants. Second order rate constants (k_2^{calc}) were then calculated by dividing the pseudo-first order rate by the concentration of excess thiol, shown in Table 2 for all five thiols included in this study.

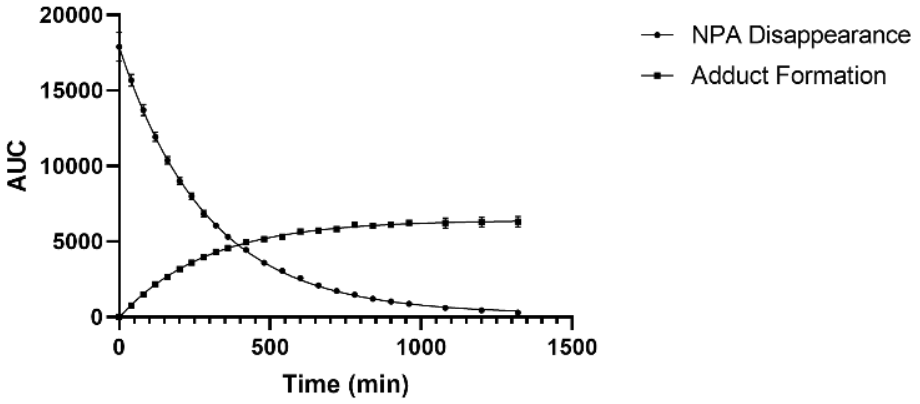

Figure 2.3. Representative plot of disappearance of NPA (1 mM) and formation of adduct for the addition of MPA (10 mM) vs time (min) in aqueous buffer (1% v/v DMSO) at pH 9, μ = 0.100, T = 22°C. The area under the curve (AUC) was integrated from the chromatograph at 214 nm for the peaks corresponding to NPA and the adduct. The AUC data for disappearance of NPA were fitted to a mono-exponential decay to afford the k_{obs} values summarized in Table 2.

Table 2.2. Observed rate constants (k_{obs}), calculated second order rate constants (k_2^{calc}), and corrected second order rate constants (k_2^{corr}) for the addition of RSH (1a-e) to NPA. Measurements were made in duplicate for both the disappearance of acrylamide and appearance of adduct, unless otherwise noted, and errors represent the standard deviation of the replicate values.

Thiol	k_{obs} (s^{-1})	k_2^{calc} ($M^{-1}s^{-1}$)	k_2^{corr} ($M^{-1}s^{-1}$)	$\log(k_2^{corr})$
1a	0.37 ± 0.03[a]	0.037 ± 0.003	0.13 ± 0.01	-0.887 ± 0.036
1b	0.068 ± 0.007	0.0068 ± 0.0007	0.061 ± 0.006	-1.214 ± 0.043
1c	0.041 ± 0.002[b]	0.0041 ± 0.0002	0.086 ± 0.005	-1.064 ± 0.024
1d	0.44 ± 0.02	0.044 ± 0.002	0.220 ± 0.008	-0.657 ± 0.016
1e	0.056 ± 0.002	0.0056 ± 0.0002	0.118 ± 0.004	-0.929 ± 0.013

[a]Measurements made in triplicate. [b]Measurements made in quadruplet.

2.4.3 pH-Rate studies

We[15] and others have shown that thiols react as nucleophiles almost exclusively from their thiolate ionization state, as demonstrated convincingly by Bednar in 1990.[16] To confirm that the thiolate is the nucleophilic species in the acrylamide addition mechanism, the second order rate constant of reaction of NPA with *N*,*N*-diethylcysteamine (DEC) was measured at five different pH values, ranging from pH 6.8 to 10. The plot of log k_2 vs pH was then fitted to eq 1 corresponding to the proportion of conjugate base (see Experimental). This fitting (Figure 4) provides a kinetic pK_a value of 7.85 ± 0.10, which corresponds closely to the thermodynamic pK_a of 7.8 reported in the literature.[12] This is consistent with the assertion that the reaction rate is exclusively dependent on the proportion of thiolate present in solution. Confirmation of this pH dependence allowed us

to correct the second order rate constants calculated for each thiol (k_2^{calc}) by the proportion of thiolate present at the pH of the reaction buffer, to give the k_2^{corr} values shown in Table 2.

In a previous study[3] conducted by Cee *et al.*, a pseudo-first order rate constant of 0.00386 ± 0.00043 min^{-1} was reported for the reaction of 5 mM GSH with 1 μM NPA at 37 °C and pH 7.4. In another study[17] by Flanagan *et al.*, a pseudo-first order rate constant of 0.013 min^{-1} was reported for the reaction of 1 mM NPA and 10 mM GSH, also at 37 °C and pH 7.4. Treating their rate constants in the same manner as described above leads to k_2^{corr} values of 0.272 ± 0.015 $M^{-1}s^{-1}$ and 0.454 $M^{-1}s^{-1}$ respectively. For the reaction of the same thiol with NPA, we calculated a corrected second order rate constant (k_2^{corr}) of 0.086 ± 0.005 $M^{-1}s^{-1}$ (see 1c in Table 2). These values are in good agreement, considering that we studied the reaction at 22 °C whereas Cee *et al.* and Flanagan *et al.* studied it at 37 °C, which accounts for their rate constants being roughly 3- to 5-fold higher.

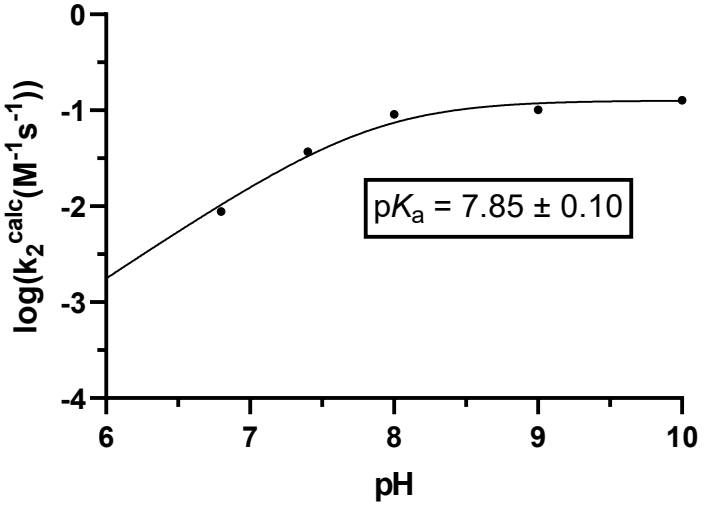

Figure 2.4. Plot of $\log(k_2^{calc})$ vs pH for the addition of **1a** to NPA in aqueous buffer (1% v/v DMSO), $\mu = 0.100$, T = 22°C. The aqueous buffers were varied to measure k_{obs} at pH 6.8, 7.4, 8.0, 9.0, and 10.0 (Table S2). The data were fitted to Eqn 5 (see Experimental), giving a kinetic pK_a value of 7.85 ± 0.10 and a maximum rate constant (k_2^{max}) of 0.1267 ± 0.0164 $M^{-1}s^{-1}$.

2.4.4 Brønsted-type plot

The corrected second order rate constants obtained for the series of thiols studied were then analysed for a linear free-energy relationship. Specifically, log k_2^{corr} values were plotted against pK_a^{RSH} to construct a Brønsted-type plot (Figure 5). This graph was fitted to a linear regression, revealing a shallow slope corresponding to a β_{nuc}^{RS-} value of 0.07 ± 0.04. This low, positive β_{nuc}^{RS-} value indicates that for alkyl thiols, NPA is relatively insensitive to thiolate nucleophilicity, and that the negative charge on the thiolate sulphur becomes only slightly less negative at the rate-limiting transition state. This is consistent with a transition state that is 'early' with respect to carbon-sulphur bond formation. It is also possible that more basic nucleophiles may present a

higher enthalpic cost of desolvation during their nucleophilic attack, partially suppressing their greater nucleophilicity, and resulting in the low observed β_{nuc}^{RS-} value. However, we do not see evidence for desolvation playing a rate-liming role, upon measurement of solvent isotope effects (see below).

The low fitted value for β_{nuc}^{RS-} also raises the question as to whether the slope is statistically significantly different from zero. An ANOVA analysis of the kinetic data provides a P value of 0.078, suggesting that at the 0.05 level, we cannot reject the hypothesis that the slope is zero. However, a β_{nuc}^{RS-} value of zero implicates a very different mechanism, in which the C-S bond would only be formed after the rate-limiting step (see below).

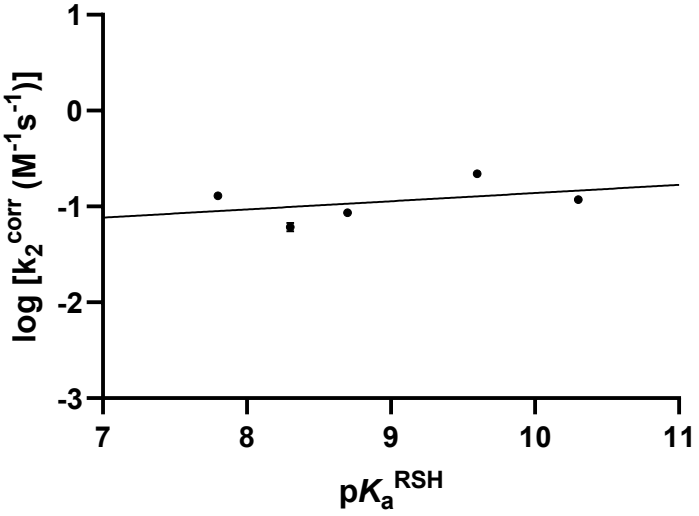

Figure 2.5. Brønsted-type plot of $\log(k_2^{corr})$ vs pK_a^{RSH} for the addition of RSH (1a-e) to NPA in aqueous buffer (1% v/v DMSO), μ=0.100, T=22°C. The data were fitted to a linear regression to provide a β_{nuc}^{RS-} value of 0.07 ± 0.04.

2.4.5 Solvent kinetic isotope effect (SKIE)

To determine whether a proton transfer is involved in the rate-limiting transition state, a solvent kinetic isotope effect (SKIE) was measured. The reaction of NPA and MPA was run in deuterated aqueous buffer and monitored by HPLC. The pD of the buffer was calculated by correcting the pH value recorded by the pH meter according to Eqn 6 (see Experimental) and the pK_a^{D2O} of the thiol corrected by Eqn 7 (see Experimental). The pD (9.7) and pK_a^{D2O} (10.68) values were used to calculate the proportion of thiolate in the reaction, which was then used to calculate the corrected second order rate constants. The ratio of the corrected second order rate constants ($k_2^{corr,H2O}/k_2^{corr,D2O}$) was calculated to be 1.09 ± 0.04 (Table S6, ESI). An unpaired *t*-test of the two data sets indicates that they are statistically distinct from each other at the 0.05 level. However, the observed value of 1.09, obtained after extrapolations according to Eqns 6 and 7, is much closer to unity than it is to the range of 3-8, expected for such a primary H/D kinetic isotope effect.[18] Therefore, we interpret the observed kinetic isotope effect as indicating that the rate-limiting step does *not* involve appreciable proton transfer. The lack of a large kinetic effect on changing from H_2O to D_2O also suggests that specific solvent effects (for example, de-solvation of thiolate nucleophile) do not appear to be kinetically significant.

2.4.6 Temperature dependence

The corrected second order rate constant (k_2^{corr}) for the reaction of NPA and MPA was then measured by the same method at three additional temperatures and used to construct an Eyring plot (Figure 6). The reactions were run in HPLC vials sealed with a pre-slit screw cap and incubated in a heated water bath. At each time point, the vials were removed from the water bath,

inverted to collect all of the condensate formed in the vial and placed in the autosampler tray. They were then returned to the incubator immediately following injection.

From the linear fitting of the Eyring plot, the enthalpy and entropy of activation were calculated, based on the slope and y-axis intercept, respectively. In this manner, $\Delta S^{\ddagger}$ was determined to be -35.8 ± 1.1 cal/mol·K, and the $\Delta H^{\ddagger}$ value was determined to be 7.94 ± 0.35 kcal/mol. The excellent linearity of the fitting (Figure 6) provides some confidence that these temperature effects are related to kinetic activation barriers, and not thermodynamic differences. However, given the uncertainties related to the Eyring plot, including a lengthy extrapolation over a reciprocal x-axis to a y-axis intercept, caution must be exercised in the interpretation of these activation parameters. That being said, the rather large negative value of $\Delta S^{\ddagger}$ suggests the transition state is highly ordered, relative to the ground state. Likewise, the relatively low value of $\Delta H^{\ddagger}$ suggests there is little change in bond order at the transition state. This is consistent with a reaction step that involves bond making (nucleophilic attack and/or net solvation at the transition state) as well as bond breaking (π-bond cleavage and/or net de-solvation at the transition state).

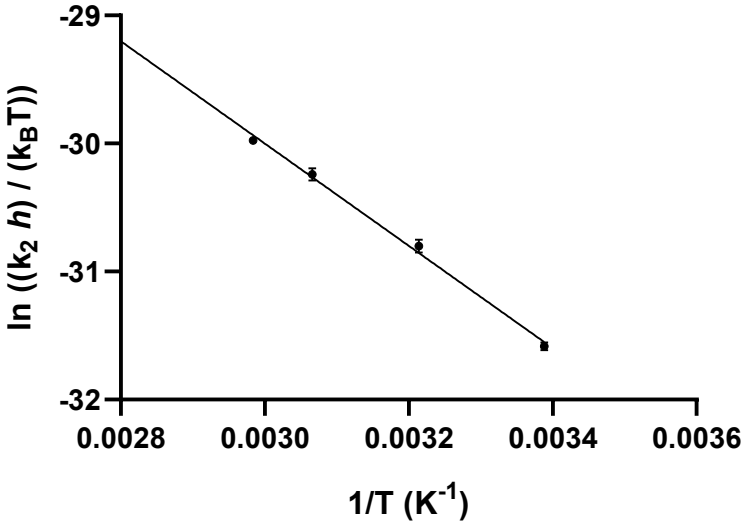

Figure 2.6. Eyring plot of ln((k_2h)/(k_BT)) vs 1/T for the addition of MPA to NPA in aqueous buffer (1% v/v DMSO), pH=9.0, μ=0.100. The data was fitted to a linear regression to obtain a slope of -3994 ± 177 and y-intercept of -18.02 ± 0.56.

2.4.7 Ionic strength effect

The reaction of NPA with MPA was also studied in aqueous buffers of varying ionic strength, in order to probe the change in electronic charge that occurs on the way to the rate-limiting transition state. The concentration of KCl salt was decreased from 0.1 M to 0.05 M (Figure 7). As the ionic strength of the buffer decreased, the rate of reaction was observed to increase. This suggests that at the rate-limiting transition state there is a net dispersal of charge, such that the ground state is stabilised more than the transition state, in solvent of higher ionic strength. This is consistent with a rate-limiting step that involves attack from thiolate having one negatively charged atom to generate a transition state where the negative charge is delocalised over the attacking thiolate and conjugated enolate.[15,19]

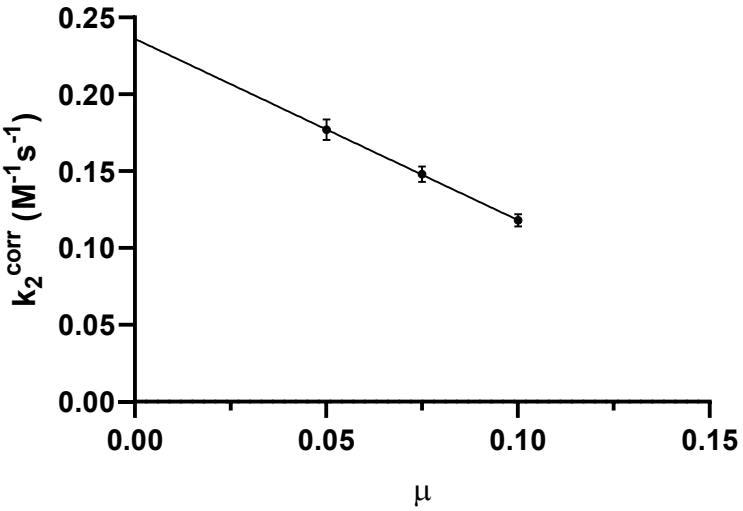

Figure 2.7. Plot of k_2^{corr} vs μ for the addition of MPA to NPA in aqueous buffer (1% v/v DMSO), pH=9.0, T=22°C. The data were fitted to a linear regression to afford a slope of -1.180 ± 0.012 and y-intercept of 0.2362 ± 0.0009.

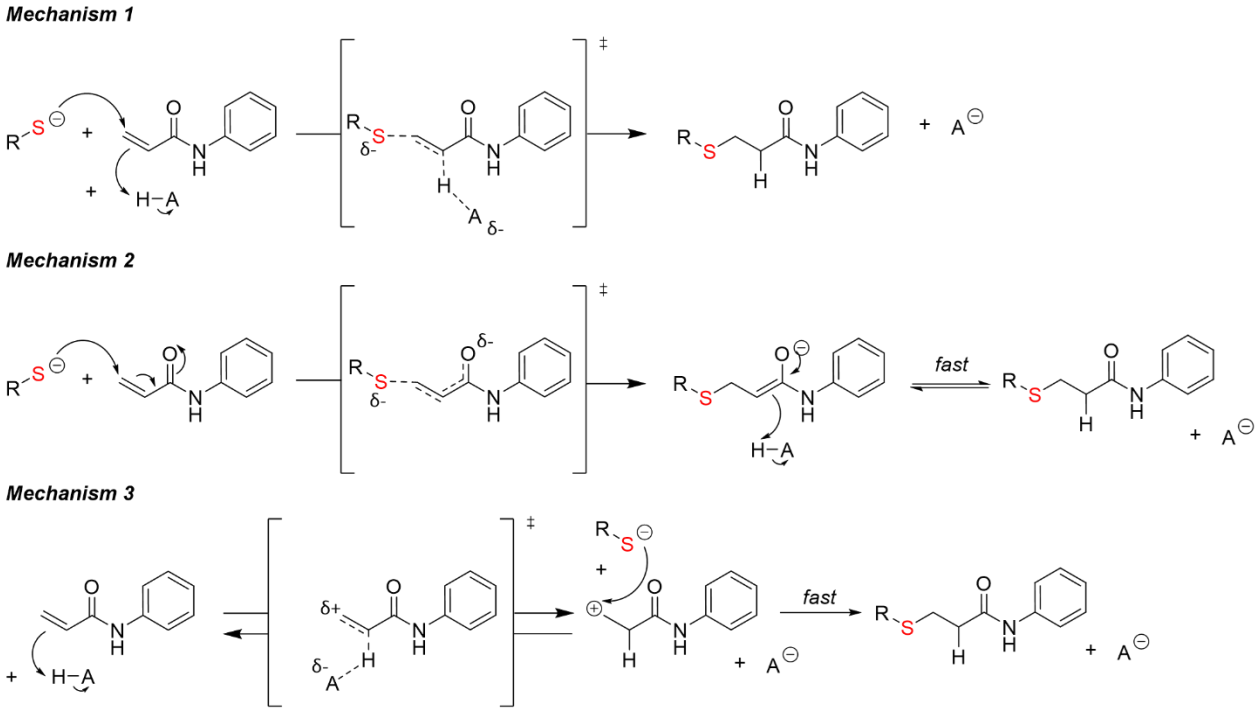

Scheme 2.2. Three hypothetical mechanisms for alkyl thiol addition to NPA, proposed *a priori*. Of these, only Mechanism 2 is consistent with all of the data presented herein (see Discussion).

2.4.8 Mechanistic interpretation

A priori, we hypothesized that three different reaction mechanisms could be proposed (see above). As shown in Scheme 2, Mechanism 1 features concerted nucleophilic attack and protonation. Mechanism 2 portrays stepwise nucleophilic attack followed by protonation, whereas Mechanism 3 (proposed for the sake of the academic exercise) shows stepwise protonation followed by nucleophilic attack.

The shallow, positive slope of the Brønsted-type plot shown in Figure 5 provides a low β_{nuc}^{RS-} value, suggesting that nucleophilic attack is rate-limiting, although little C-S bond formation has occurred at the rate-limiting transition state. This is consistent with Mechanisms 1 and 2. On the

other hand, if this slope were zero (see above), this would signify there is no C-S bond formation up to and including the rate-limiting transition state, which would be consistent with Mechanism 3. The small solvent kinetic isotope effect observed for this reaction suggests that there is no proton in flight at the rate-limiting transition state (see above). This evidence refutes Mechanisms 1 and 3. The temperature dependence of the reaction (Figure 6) provides a large negative entropy of activation, which is more consistent with the bimolecular transition states of Mechanisms 1 and 2 than the proton transfer to buffer or bulk solvent in Mechanism 3. The relatively small enthalpy of activation suggests the coordination of bond making and breaking events, consistent with the conjugate addition steps proposed in Mechanisms 1 and 2. Finally, the negative slope observed in Figure 7, indicating that the reaction is slower at higher ionic strength, is suggestive of a transition state where charge is dispersed, as in Mechanisms 1 and 2, rather than created, as in Mechanism 3.

Taken together, the empirical data consistently refute Mechanism 3, a mechanism that appears highly unlikely, even if one considers only the basicity of NPA. However, it is more informative to consider the distinction between Mechanism 1, the microscopic reverse of the concerted E2 elimination, and Mechanism 2, the microscopic reverse of the stepwise $E1_{cb}^{rev}$ elimination. The solvent kinetic isotope data is the only line of empirical evidence presented herein that rules out Mechanism 1 in favour of Mechanism 2. However, this is also consistent with intuitive interpretation of the microscopic reverse reaction. Typically, elimination from a β-substituted carbonyl compound proceeds through an initial deprotonation owing to the stability of the intermediate enolate ($E1_{cb}^{rev}$), and the concerted elimination (E2) is not enforced for such a substrate.

2.4.9 Molecular modelling

In conjunction with our experimental data, which consistently support Mechanism 2, we used DFT calculations to confirm that the mechanism is reasonable, chiefly to identify the approximate structure of the rate-limiting transition state. The results are summarized in the free energy profile in Figure 8. Methanethiol was used as a model nucleophile. Deprotonation of the thiol to form the thiolate is modestly endergonic (4.7 kcal/mol). This is followed by a transition state (TS1), featuring the attack of the thiolate on the conjugated system. This step is predicted to be rate-limiting, with an activation energy of 19.0 kcal/mol. This transition state structure (Figure 8B) features a very long partial bond between the sulphur atom and the β-carbon, of ~2.3 Å. This limited formation of the C–S bond in the transition state structure is also consistent with the shallow slope of the Brønsted-type plot (Figure 5), which indicates little change in the charge on the sulphur at the rate-limiting transition state. This transition state leads to a meta-stable enolate intermediate. Protonation of this enolate at the alpha position yields a stable thioether product. These calculations are consistent with Mechanism 2 being a low energy path where the rate-limiting transition state involves limited C–S bond formation.

To compare this reaction profile to that of a thiol having a lower pK_a, we repeated these calculations using 1a as the thiol reactant. The TS1 structure was similar, with a C–S partial bond length of ~2.3 Å and an activation energy of 16.4 kcal/mol. Relative to the thiolate, the activation energy of 1a is 1 kcal/mol higher than that of methanethiol, which is consistent with the shallow positive Brønsted slope measured experimentally.

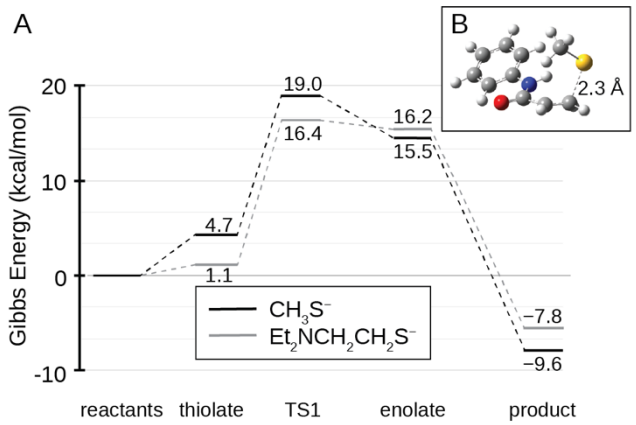

Figure 2.8. A) Calculated energy diagram of the thiol addition of methanethiol and 1a to NPA. **B)** Length of the partial bond between the β-carbon of NPA and sulphur atom of methanethiol at the transition state was calculated to be ~2.3 Å.

2.5 Conclusions

In this study, we provide multiple lines of experimental evidence in favour of the addition of alkyl thiol to NPA proceeding by nucleophilic attack of the thiolate, followed by rapid protonation of the intermediate enolate. This mechanism is supported by DFT calculations and is consistent with what one may have predicted intuitively, based on consideration of the microscopic reverse reaction, namely $E1_{cb}^{rev}$ elimination of the β-mercapto substituted *N*-phenylpropionamide. These results also confirm the suitable balance between stability and reactivity[3] shown by the acrylamide group, underpinning its suitability as a warhead for TCIs.

However, it is also important to note the shallow slope of the Brønsted-type plot (Figure 5), which clearly indicates that the thiol-addition reaction of NPA is relatively insensitive towards the nucleophilicity of the thiolate. This indicates there is relatively little rate acceleration to be gained by forming a highly basic thiolate (from a weakly acidic thiol), and NPA is just as likely to react efficiently with a weakly basic thiolate (formed from a more acidic thiol). From this point of view,

it appears that the rate of reaction of the NPA warhead with a Cys residue would require only that the residue is ionised (i.e., that its pK_a is sufficiently low with respect to physiological pH) and depends very little on the nucleophilicity of the resulting thiolate. In other words, the site selectivity of the reaction of the NPA warhead with multiple Cys residues would be based on a difference in their degree of ionisation, which may not be significant. In turn, this emphasizes how critical it is that the scaffold of a TCI directs its binding to the vicinity of a specific Cys residue, prior to its rapid reaction with the side-chain thiolate.

2.6 Experimental

2.6.1 Synthesis

All reagents and solvents were purchased from commercial sources and used without further purification. ^{1}H and ^{13}C spectra were recorded on a Bruker 400 MHz spectrometer, and chemical shifts were reported in ppm referenced to the deuterated solvent peak. High resolution mass spectra were recorded with a quadrupole time-of-flight (QTOF) analyzer and either electrospray ionization (ESI) or electron impact (EI) as noted below.

_N_-Phenylacrylamide (NPA)

In a flame dried round bottom flask, 1.5 mL (16.43 mmol) aniline and 1 mL (7.17 mmol) Et_3N was stirred. An aliquot of 0.23 mL (2.76 mmol) of acryloyl chloride was diluted in 30 mL ACN. The acryloyl chloride in ACN was added dropwise to the aniline and triethylamine solution over 20 min and the reaction was stirred for 3.5 hours. The ACN was removed *in vacuo*. The remaining solution was dissolved in EtOAc and washed with 3 × 1 M HCl, 3 × saturated $NaHCO_3$ and brine. It was then dried over Mg_2SO_4, concentrated, and dried at vacuum overnight. The product was recovered as a red powder, 390 mg (2.65 mmol), 96% yield.

^{1}H NMR (400 MHz, $CDCl_3$) δ 7.59 (d, J = 7.9 Hz, 3H), 7.32 (t, 1H), 7.12 (t, J = 7.4 Hz, 1H), 6.43 (dd, J = 16.9, 1.4 Hz, 1H), 6.27 (dd, J = 16.9, 10.2 Hz, 1H), 5.75 (dd, J = 10.1, 1.4 Hz, 1H). ^{13}C NMR (101 MHz, $CDCl_3$) δ 163.65, 137.76, 131.24, 129.04, 127.75, 124.57, 120.07. HRMS (EI) calculated (C_9H_9NO): 147.0684, found: 147.0681.

β-Mercapto-*N*-phenylpropionamide

^{1}H NMR (400 MHz, D_2O) δ 7.52 – 7.44 (m, 4H), 7.31 – 7.26 (m, 1H), 2.94 (d, J = 6.9 Hz, 2H), 2.84 (t, J = 7.4 Hz, 2H), 2.78 – 2.72 (m, 1H), 2.51 (t, J = 7.4 Hz, 2H). HRMS (ESI) calculated ($C_{12}H_{14}NO_3SD$): 277.0733, found: 277.0735.

2.6.2 Kinetics

The concentration of H_3O^+ was obtained using Fisher Scientific Accumet 15 pH meter calibrated with certified standard aqueous buffers of pH 4.00, 7.00, and 10.00. The pH was determined as -log[H_3O^+].

HPLC traces were collected by Gilson-Mandel GXP271 high performance liquid chromatography (HPLC) with UV detection at 214 and 254 nm (Phenomenex Luna, 150 mm × 4.6 mm, 30 min, 1.5 mL/min flow rate, variable gradient of 0.1% TFA in CH_3CN/0.1% TFA in H_2O). Elution conditions were adjusted to allow baseline separation of the adduct (see Table S1, ESI).

A stock solution of 0.1 M NPA was prepared in DMSO that was used throughout the course of the study and stock solutions of 0.1 M for each thiol were prepared in their respective buffers shortly before use. To the 2 mL HPLC vials containing 1602 μL of aqueous buffer, 180 μL of 0.1 M thiol stock solution was added. The reactions were initiated with the addition of 18 μL of 0.1 M NPA stock solution and the vials were inverted to ensure proper mixing. An initial aliquot was taken immediately after initiation and repeated at pre-determined time points over the course of at least 5-6 half lives. The reactions were run in at least duplicate, staggering initiation of the replicates to obtain the same time points.

The increasing AUC of the adduct peaks of the HPLC chromatograms were fitted to a mono-exponential association model with the constraint that $Y_0 = 0$ (Eqn 1).

(1) $$AUC = AUC_{max}(1 - e^{-k_{obs}t})$$

The decreasing AUC of the NPA peaks of the HPLC chromatograms were fitted to a mono-exponential decay model, with the constraint that the lower plateau = 0 (Eqn 2).

(2) $$AUC = AUC_0(e^{-k_{obs}t})$$

Both of these methods were used to obtain replicate pseudo-first order k_{obs} values. Second order rates constants were then calculated by dividing these pseudo-first order rate constants by the concentration of excess thiol (Eqn 3).

(3) $$k_2^{calc} = \frac{k_{obs}}{[thiol]}$$

The final, corrected second order rate constants were then calculated by dividing by the fraction of thiolate at the reaction pH, given by the corresponding pK_a value of the thiol (Eqn 4).

(4) $$k_2^{corr} = \frac{k_2^{calc}}{\left(\frac{K_a}{[H^+]+K_a}\right)}$$

The data for the addition of 1a to NPA in aqueous buffer of varying pH were fitted according to Eqn 5 to calculate the kinetic pK_a value and maximum rate constant (k_2^{max}).

(5) $$k_2 = k_2^{max}\left(\frac{K_a}{([H^+]+K_a)}\right)$$

For the reactions run in D_2O for the kinetic isotope effect studies, the pD of the solution was calculated according to the meter pH reading as shown in Eqn 6.

(6) $pD = pH + 0.4$[20]

The effect of D_2O on thiol was taken into account using the equation previously established by Jencks and Salvesen (Eqn 7).

(7) $\Delta pK = 0.26 + 0.012pK_a$[21]

2.6.3 DFT Calculations

The DFT calculations were performed using Gaussian 16.[22] All calculations were performed using the **ω**B97X-D functional[23] with the def2-TZVP basis set.[24] This functional has been shown to be effective for modeling thio-Michael additions because the range-separation approach employed by the wB97XD exchange-correlation functional resolves issues with delocalization error that occur when some popular DFT methods (e.g., B3LYP, PBE0, or DFTB) are used to describe thiolates.[25,26] The Conductor-like Polarizable Continuum Model (CPCM) was used to represent the aqueous solvent. [27] The Gibbs energy required to form the deprotonated thiolate was calculated from the experimental pK_a (10.4 and 7.8, for methanethiol and *N,N*-diethylcysteamine, respectively) based on a solution pH of 7 using the relation $\Delta G_{deprot} = RT \cdot \log(pK_a - pH)$. This energy is included in the calculation of the Gibbs energy of the transition state and enolate structures, which are calculated relative the thiolate reactant. The product energy was calculated relative to the neutral thiol reactant.

2.7 References

1 S. K. I. Watt, J. G. Charlebois, C. N. Rowley and J. W. Keillor, *Org Biomol Chem*, 2022, **20**, 8898–8906.

2 J. Singh, R. C. Petter, T. A. Baillie and A. Whitty, *Nat Rev Drug Discov*, 2011, **10**, 307–317.

3 V. J. Cee, L. P. Volak, Y. Chen, M. D. Bartberger, C. Tegley, T. Arvedson, J. McCarter, A. S. Tasker and C. Fotsch, *J Med Chem*, 2015, **58**, 9171–9178.

4 M. C. Genovese, A. Spindler, A. Sagawa, W. Park, A. Dudek, A. Kivitz, J. Chao, L. S. M. Chan, J. Witcher, W. Barchuk and A. Nirula, *J Rheum*, 2021, **48**, 969–976.

5 J. Y. Byun, Y. T. Koh, S. Y. Jang, J. W. Witcher, J. R. Chan, A. Pustilnik, M. J. Daniels, Y. H. Kim, K. H. Suh, M. D. Linnik and Y. M. Lee, *Sci Rep*, 2021, **11**, 1–14.

6 P. H. Schafer, A. J. Kivitz, J. Ma, S. Korish, D. Sutherland, L. Li, A. Azaryan, J. Kosek, M. Adams, L. Capone, E. M. Hur, D. R. Hough and G. E. Ringheim, *Rheumatol Ther*, 2020, **7**, 101–119.

7 L. V. Sequist, Z. Piotrowska, M. J. Niederst, R. S. Heist, S. Digumarthy, A. T. Shaw and J. A. Engelman, *JAMA Oncol*, 2016, **2**, 541–543.

8 Y.-L. Wu, M. Tsuboi, J. He, T. John, C. Grohe, M. Majem, J. W. Goldman, K. Laktionov, S.-W. Kim, T. Kato, H.-V. Vu, S. Lu, K.-Y. Lee, C. Akewanlop, C.-J. Yu, F. de Marinis, L. Bonanno, M. Domine, F. A. Shepherd, L. Zeng, R. Hodge, A. Atasoy, Y. Rukazenkov and R. S. Herbst, *N Engl J Med*, 2020, **383**, 1711–1723.

9 L. V. Sequist, J.-C. Soria, J. W. Goldman, H. A. Wakelee, S. M. Gadgeel, A. Varga, V. Papadimitrakopoulou, B. J. Solomon, G. R. Oxnard, R. Dziadziuszko, D. L. Aisner, R. C. Doebele, C. Galasso, E. B. Garon, R. S. Heist, J. Logan, J. W. Neal, M. A. Mendenhall, S. Nichols, Z. Piotrowska, A. J. Wozniak, M. Raponi, C. A. Karlovich, S. Jaw-Tsai, J. Isaacson,

D. Despain, S. L. Matheny, L. Rolfe, A. R. Allen and D. R. Camidge, *N Engl J Med*, 2015, **372**, 1700–1709.

10 A. Birkholz, D. J. Kopecky, L. P. Volak, M. D. Bartberger, Y. Chen, C. M. Tegley, T. Arvedson, J. D. McCarter, C. Fotsch and V. J. Cee, *J Med Chem*, 2020, **63**, 11602–11614.

11 Y. J. Lee, Y. Kurra and W. R. Liu, *ChemBioChem*, 2016, **17**, 456–461.

12 V. Franzen, *Chem Ber*, 1957, **90**, 623–633.

13 A. K. Mitra and M. M. Narurkar, *Int J Pharm*, 1986, **28**, 119–124.

14 J. P. Danehy and K. N. Parameswaran, *J Chem Eng Data*, 1968, **13**, 386–389.

15 M. A. R. Raycroft, K. Racine, C. N. Rowley and J. W. Keillor, *J Org Chem*, 2018, **83**, 11674–11685.

16 R. A. Bednar, *Biochem*, 1990, **29**, 3684–3690.

17 M. E. Flanagan, J. A. Abramite, D. P. Anderson, A. Aulabaugh, U. P. Dahal, A. M. Gilbert, C. Li, J. Montgomery, S. R. Oppenheimer, T. Ryder, B. P. Schuff, D. P. Uccello, G. S. Walker, Y. Wu, M. F. Brown, J. M. Chen, M. M. Hayward, M. C. Noe, R. S. Obach, L. Philippe, V. Shanmugasundaram, M. J. Shapiro, J. Starr, J. Stroh and Y. Che, *J Med Chem*, 2014, **57**, 10072–10079.

18 F. H. Westheimer, *Chem Rev*, 1961, **61**, 265–273.

19 J. W. Ogilvie, J. T. Tildon and B. S. Strauch, *Biochem*, 1964, **3**, 754–758.

20 M. P. Dale, W. P. Kopfler, I. Chait and L. D. Byers, *Biochem*, 1986, **25**, 2522–2529.

21 W. P. Jencks and K. Salvesen, *J Am Chem Soc*, 1971, **93**, 4433–4436.

22 M. J. Frisch, G. W. Trucks, H. B. Schlegel, G. E. Scuseria, M. a. Robb, J. R. Cheeseman, G. Scalmani, V. Barone, G. a. Petersson, H. Nakatsuji, X. Li, M. Caricato, a. V. Marenich, J. Bloino, B. G. Janesko, R. Gomperts, B. Mennucci, H. P. Hratchian, J. V. Ortiz, a. F.

Izmaylov, J. L. Sonnenberg, Williams, F. Ding, F. Lipparini, F. Egidi, J. Goings, B. Peng, A. Petrone, T. Henderson, D. Ranasinghe, V. G. Zakrzewski, J. Gao, N. Rega, G. Zheng, W. Liang, M. Hada, M. Ehara, K. Toyota, R. Fukuda, J. Hasegawa, M. Ishida, T. Nakajima, Y. Honda, O. Kitao, H. Nakai, T. Vreven, K. Throssell, J. a. Montgomery Jr., J. E. Peralta, F. Ogliaro, M. J. Bearpark, J. J. Heyd, E. N. Brothers, K. N. Kudin, V. N. Staroverov, T. a. Keith, R. Kobayashi, J. Normand, K. Raghavachari, a. P. Rendell, J. C. Burant, S. S. Iyengar, J. Tomasi, M. Cossi, J. M. Millam, M. Klene, C. Adamo, R. Cammi, J. W. Ochterski, R. L. Martin, K. Morokuma, O. Farkas, J. B. Foresman and D. J. Fox, Gaussian, Inc., Wallingford CT, 2016.

23 J. Da Chai and M. Head-Gordon, *Phys Chem Chem Phys*, 2008, **10**, 6615–6620.

24 F. Weigend and R. Ahlrichs, *Phys Chem Chem Phys*, 2005, **7**, 3297–3305.

25 J. M. Smith, Y. Jami Alahmadi and C. N. Rowley, *J Chem Theory Comput*, 2013, **9**, 4860–4865.

26 E. Awoonor-Williams, W. C. Isley, S. G. Dale, E. R. Johnson, H. Yu, A. D. Becke, B. Roux and C. N. Rowley, *J Comput Chem*, 2020, **41**, 427–438.

27 A. v. Marenich, C. J. Cramer and D. G. Truhlar, *J Phys Chem B*, 2009, **113**, 6378–6396.

Chapter 3 : A mechanistic study of thiol addition to *N*-acryloylpiperidine

Sarah K. I. Watt[a], Janique G. Charlebois[a], Christopher N. Rowley[b], Jeffrey W. Keillor[a]*

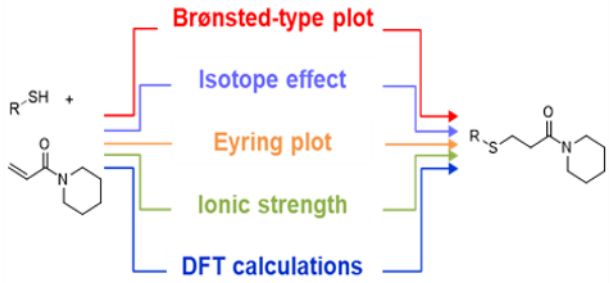

3.1 Statement of Contributions

This manuscript is a collaborative effort between all authors listed in the publication. SKIW contributed to the conceptualization, methodology and experimentation (synthesis, characterization, intrinsic reactivity), and writing. JGC contributed to the experimentation (intrinsic reactivity) as an undergraduate student under the supervision of SKIW. CNR contributed to the methodology and experimentation (molecular modelling) as well as writing. Finally, JWK contributed to the conceptualization, funding acquisition, supervision, interpretation, and writing. All authors reviewed and edited the work prior to publication.

Reproduced from S. K. I. Watt, J. G. Charlebois, C. N. Rowley, & J. W. Keillor. A mechanistic study of thiol addition to *N* -acryloylpiperidine. *Organic & Biomolecular Chemistry*, 2023, 21, 2204–2212[1] with permission from the Royal Society of Chemistry.

3.2 Abstract

Nucleophilic cysteine (Cys) residues are present in many enzyme active sites and represent the target of many different irreversible enzyme inhibitors. Given its fine balance between aqueous stability and thiolate reactivity, the acrylamide group is a particularly popular warhead pharmacophore among inhibitors designed for biological and therapeutic application. The acrylamide group is well known to undergo thiol addition, but the precise mechanism of this addition reaction has not been studied in as much detail. In this work we have focused on the reaction of *N*-acryloylpiperidine (AcrPip), which represents a motif found in many targeted covalent inhibitor drugs. Using a precise HPLC-based assay, we measured the second order rate constants for the reaction of AcrPip with a panel of thiols having different pK_a values. This allowed construction of a Brønsted-type plot that reveals the relative insensitivity of the reaction to the nucleophilicity of the thiolate. By studying temperature effects, we were able to construct an Eyring plot from which the enthalpy and entropy of activation were calculated. Ionic strength and solvent kinetic isotope effects were also studied, informing on charge dispersal and proton transfer in the transition state. DFT calculations were also performed, providing information on the potential structure of the activated complex. Taken together, these data strongly support one cohesive addition mechanism that is the microscopic reverse of the $E1_{cb}$ elimination, and highly relevant to the intrinsic thiol selectivity of AcrPip inhibitors and their subsequent design.

Keywords: acrylamide, piperidine, irreversible inhibitor, thiol-addition, kinetics, mechanism

3.3 Introduction

Irreversible small molecule enzyme inhibitors often target nucleophilic cysteine (Cys) residues found in or near enzyme active sites. Many of these inhibitors are designed to bear an acrylamide group that undergoes an addition reaction with the reactive sidechain thiolate of the Cys residue, thereby covalently anchoring the inhibitor to its target enzyme. Many studies have been conducted recently to begin to elucidate the detailed mechanism of thiol-addition to acrylamides and to characterize their intrinsic reactivity[2–5]. However, the focus of most of these studies has been directed towards *N*-aryl acrylamides, or more specifically *N*-phenyl acrylamides[2,3,5]. While these studies have provided valuable insight into the intrinsic reactivity of acrylamide warheads, there remains a lack of data surrounding *N*-alkyl and *N,N*-dialkyl acrylamide derivatives. Along with the commonly substituted *N*-phenyl derivative,[2,3] the *N*-acryloylpiperidine group is of particular interest, as it is currently employed in inhibitors such as zanubrutinib[6,7] and ibrutinib[8,9], two small molecule anti-cancer agents used to target Bruton's tyrosine kinase (Figure 1).

Our current work aims to study the mechanism of thiol addition to *N*-acryloylpiperidine (AcrPip) as a model electrophile. AcrPip was allowed to react with five different thiols of varying pK_a values in aqueous buffer, and temperature, ionic strength, and solvent kinetic isotope effects were studied in order to determine the effect on the thiol addition mechanism. This study follows our previous mechanistic study on *N*-phenylacrylamide[5] and allows comparison of the effects of changing the intrinsic properties of the *N*-substituent present in different classes of therapeutic inhibitors.

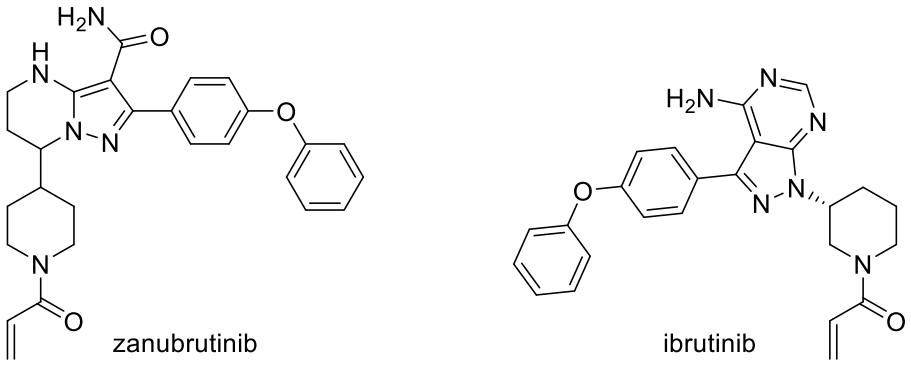

Figure 3.1. Examples of irreversible enzyme inhibitors utilizing AcrPip as the electrophilic warhead.

3.4 Results and Discussion

3.4.1 Product studies

N-acryloylpiperidine (AcrPip) was prepared by reacting acryloyl chloride with piperidine (see Experimental). The addition reactions between AcrPip and selected thiols were monitored by HPLC, following both the disappearance of the acrylamide and the appearance of the acrylamide-thiol adduct.

To confirm that the reaction product detected by UV-HPLC was the expected adduct formed by thiol addition to the acrylamide β-carbon, reactions were additionally monitored by both NMR and mass spectrometry. More specifically, AcrPip and diethyl cysteamine (DEC) were dissolved in deuterated buffer and allowed to react in an NMR tube. ^{1}H-NMR spectra were recorded over the course of the reaction and were used to monitor the disappearance of the vinyl acrylamide signals and the simultaneous shift of proton signals from DEC, adjacent to the attacking thiolate (see Figure 2). Final ^{1}H and 2D-COSY spectra were taken to confirm the identity and structure of the resulting adduct (see Figures S15-16, ESI). As well, once sufficient adduct had formed, an

aliquot of the reaction mixture was analysed by HPLC to confirm the retention time of the formed adduct, and the product peak was collected for analysis by high resolution mass spectroscopy to confirm its identity as the thiol-addition adduct.

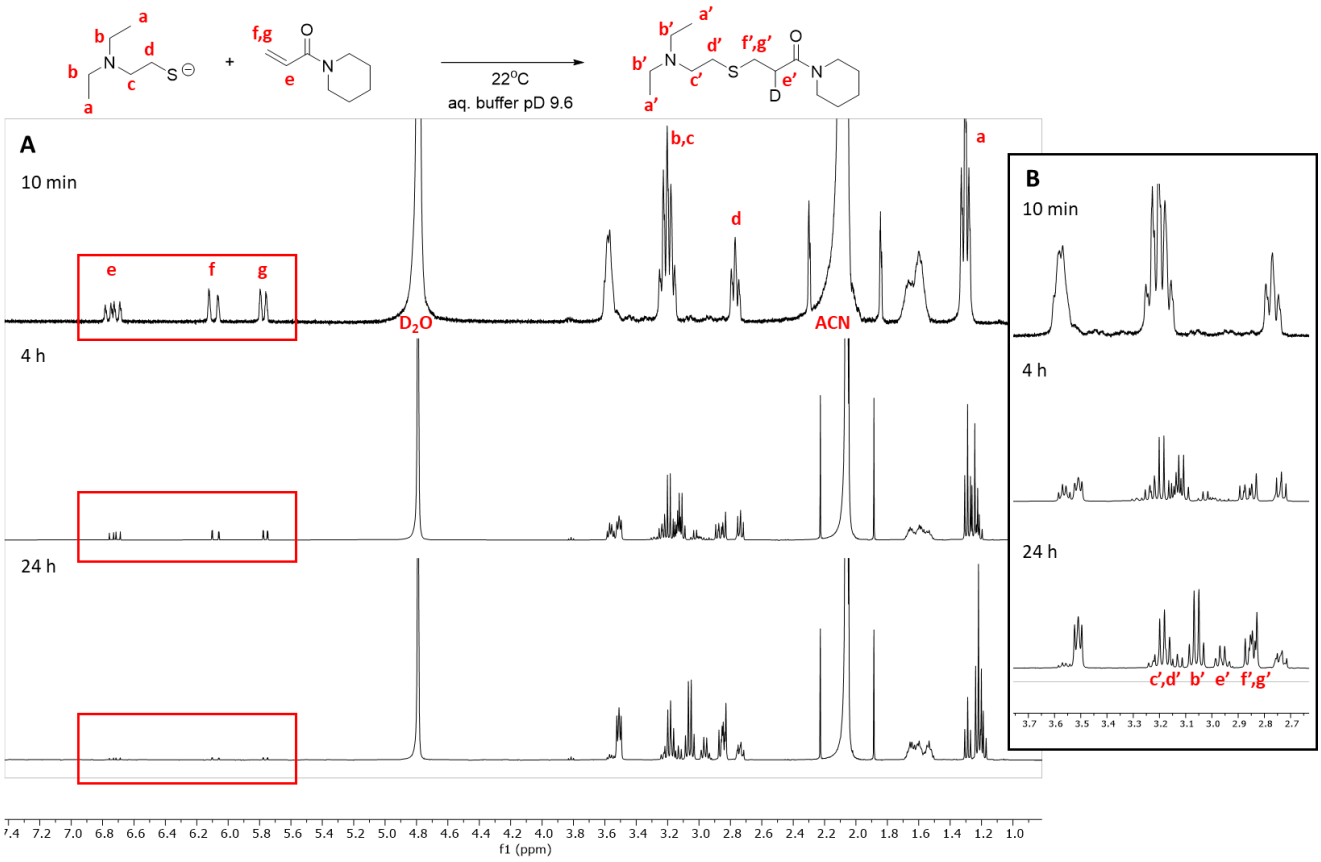

Figure 3.2. (A) ^{1}H-NMR spectra recorded at 10 min (top), 4 h (middle) and 24 h (bottom) monitoring the reaction progress between AcrPip and DEC. The disappearance of vinyl acrylamide signals was observed, along with the simultaneous appearance and shift of signals corresponding to the methylene protons adjacent to the attacking thiolate. **(B)** Magnified region of ^{1}H-NMR spectra (2.7 – 3.7 ppm) highlighting the proton signals adjacent to the attacking thiolate.

3.4.2 Kinetic studies by HPLC

Kinetic reactions were prepared in 2-mL HPLC vials fitted with a pre-slit screw cap and monitored in the same manner as previously reported[5]. For this study, five alkyl thiols were chosen with varying pK_a values similar to those of a Cys residue of a protein target, ranging from 7.8 to 10.3 (Table 1). The reactions were run in aqueous buffer using 1% v/v DMSO as a co-solvent (Scheme 1).

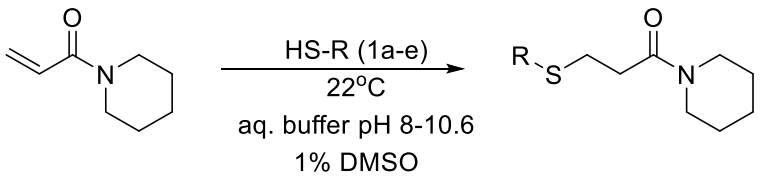

R =
a) $CH_2CH_2NEt_2$
b) $CH_2CH(NH_2)CO_2H$
c) $CH_2CH(C(O)NHCH_2CO_2H)NHC(O)CH_2CH_2CH(NH_2)CO_2H$
d) CH_2CH_2OH
e) $CH_2CH_2CO_2H$

Scheme 3.1. General scheme for the addition of RSH to AcrPip.

The reactions were run under pseudo-first order conditions, in the presence of a large excess of thiol and limiting concentration of AcrPip. In this way the impact of thiol oxidation on the observed reaction rates was also minimized. As a control, the long-term stability of AcrPip in aqueous buffer was monitored over 24 hours (see Figure S1), confirming that all observed disappearance of the acrylamide during a kinetic run can be ascribed to its reaction with thiol. The pH of the aqueous buffers used was varied according to the thiol used in each run. As previously reported,[5,10,11] the rate of thiol addition is dependent on the proportion of thiolate that is present in solution. For some thiols, the reaction with AcrPip was found to progress relatively slowly (see below), so the pH of the reaction mixture was raised, increasing the proportion of thiolate and the

observed reaction rate, allowing for data to be collected within an acceptable timeframe, and prior to significant thiol oxidation.

Reaction progress was thus monitored over 5 to 6 half-lives, using reverse-phase HPLC with UV detection at 214 nm. Both the disappearance of acrylamide as well as the formation of the thiol-acrylamide adduct were followed. Stock solutions for each thiol were prepared shortly before use in the corresponding reaction buffer and a stock solution of AcrPip was prepared in DMSO and used over the course of the study. Once the reactions were initiated, they were placed in the autosampler tray of the HPLC and incubated at room temperature. Aliquots of each reaction were taken at pre-determined time points, typically every 15-20 min based on the HPLC method, and the relative proportions of acrylamide and adduct were quantified by integrating the area under the curve (AUC) for each peak at 214 nm. The integrated AUC data for disappearance and formation were fitted over time to a mono-exponential equation for decay (Eqn 2, Experimental) or association (Eqn 1, Experimental) respectively, to give the observed reaction rates (k_{obs}). The k_{obs} values were then used to calculate the second order rate constants (k_2^{calc}) by dividing by the concentration of thiol in excess (Eqn 3, Experimental). Finally, we corrected for the proportion of thiolate present in solution according to Eqn 4 (see Experimental), since it has been previously established that the thiolate is the nucleophilic species[5,10,11]. This allowed the direct comparison of corrected second order reaction rate constants (k_2^{corr}) for all thiols.

In a previous study[4] by Flanagan *et al*, a pseudo-first order rate constant was measured for the addition of 10 mM GSH to 1 mM AcrPip at 37 °C and pH 7.4. They observed a half-life of 33 h, corresponding to a k_{obs} of 3.5×10^{-4} min^{-1}. Treating this k_{obs} in the same manner as those measured herein affords a calculated k_2^{corr} of 1.4×10^{-2} $M^{-1}s^{-1}$. In comparison, our calculated k_2^{corr} for the same reaction was measured to be $(0.824 \pm 0.121) \times 10^{-2}$ $M^{-1}s^{-1}$ (Table S2). Comparatively, these

two k_2^{corr} values are in good agreement, considering that we measured k_{obs} at 22°C whereas Flanagan *et al* recorded k_{obs} at 37°C, which accounts for the approximate 2-fold increase.

Table 3.1. Structures, names and literature pK_a values for thiols **1a-e**.

Thiol	Structure	Name	Thiol pK_a
1a	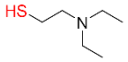	*N,N*-diethylcysteamine (DEC)	7.8[12]
1b	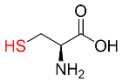	L-cysteine (Cys)	8.3[13,14]
1c	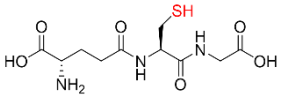	glutathione (GSH)	8.7[13]
1d	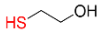	β-mercaptoethanol (BME)	9.6[14]
1e	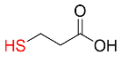	3-mercaptopropionic acid (MPA)	10.3[14]

3.4.3 Brønsted-type plot

The kinetic analysis of all five thiols is summarized in Table S2. The log values of the corrected second order rate constants (log k_2^{corr}) were also plotted against the pK_a of the respective thiols and the resulting Brønsted-type plot was fitted to linear regression (Figure 3). This reveals a shallow, positive slope (β_{nuc}^{RS-} value). Because the calculated slope is quite shallow, we tested for the

statistical significance against the null hypothesis that the slope is equal to zero, using an ANOVA analysis. From this, we obtained a *P* value of 0.0004, meaning that the slope is clearly statistically distinct from zero. This positive β_{nuc}^{RS-} value indicates a decrease of the negative charge on the incoming thiolate sulphur at the rate-limiting transition state, consistent with rate-limiting nucleophilic attack. However, the low value also indicates that AcrPip is relatively insensitive to the basicity/nucleophilicity of the thiolate and that the *decrease* of the negative charge on the thiolate at the transition state is very small, suggestive of long partial bond formation at the transition state.

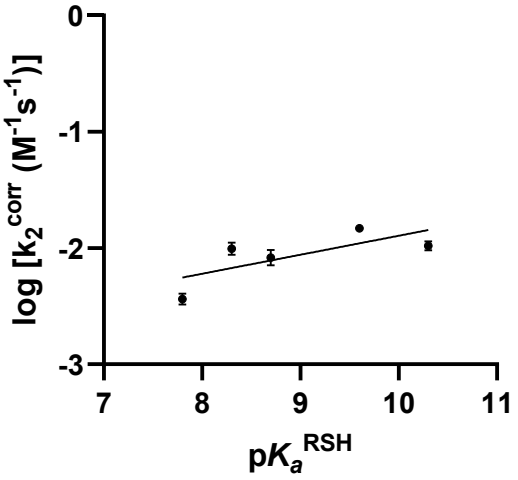

Figure 3.3. Brønsted-type plot of $\log(k_2^{corr})$ vs pK_a^{RSH} for the addition of RSH (1a-e) to AcrPip in aqueous buffer (1% v/v DMSO), μ=0.100, T=22°C. The data were fitted to a linear regression to provide a β_{nuc}^{RS-} value of 0.11 ± 0.03.

3.4.4 Solvent kinetic isotope effect (SKIE)

The reaction of AcrPip and DEC was also performed in deuterated aqueous buffer and monitored kinetically by the same method, to measure the solvent kinetic isotope effect. Two important approximations were necessary for this experiment. First, the pD of the buffer was extrapolated from the pH meter reading, according to Eqn 5 (see Experimental). Second, the pK_a^{D2O} of DEC was extrapolated from its aqueous pK_a value, according to Eqn 6 (see Experimental). This approach allowed us to calculate the corrected second order rate constant in D_2O, and to compare it to that measured in protonated buffer. The ratio of $k_2^{corr, H2O}/k_2^{corr, D2O}$ was thus calculated to be 1.52 ± 0.17. The two data sets were found to be statistically different at the 0.05 level, using an unpaired *t*-test, suggesting the ratio is statistically different from unity, according to the *precision* of the data sets. However, the approximations used to arrive at the value of $k_2^{corr,D2O}$ (see above) may give reason to question the *accuracy* of this isotope effect. In any case, we can safely interpret the value of 1.5 as being distinctly smaller than what one would expect for a primary H/D kinetic isotope effect, which would be in the range of 3 to 8-fold for such addition/elimination reactions[15]. Rather, the observed solvent kinetic isotope effect may result from weak solvation of the developing oxyanion during formation of the enolate intermediate.

3.4.5 Temperature dependence

The kinetic reaction of AcrPip and DEC was also studied over a temperature range of 22 to 62 °C. Reactions were run in the same manner as described above, but were incubated in a heated water bath between the collection of aliquots. Before each time point, the vials were removed from the water bath, inverted to collect all condensation formed on the walls of the glass vials, and

placed in the autosampler tray for immediate injection onto the HPLC. The vials were then returned to the heated bath immediately following the injection.

Corrected second order rate constants obtained in this manner were then used to construct an Eyring plot (Figure 4). From the linear fit of the Eyring plot, the slope was used to calculate an enthalpy of activation ($\Delta H^{\ddagger}$) of 10.5 ± 0.5 kcal/mol. The y-intercept was used to calculate an entropy of activation ($\Delta S^{\ddagger}$) of -33.3 ± 1.5 cal/mol·K. The relatively large negative $\Delta S^{\ddagger}$ is consistent with a highly ordered transition state, relative to the ground state. This would be expected for a bimolecular transition state involving nucleophilic attack of thiolate on acrylamide. The relatively low $\Delta H^{\ddagger}$ is consistent with a transition state representing a low net enthalpic barrier, where both bond making and bond breaking occur simultaneously, such as expected for the partial formation of a C—S σ bond and the partial cleavage of a C=C π bond (see below).

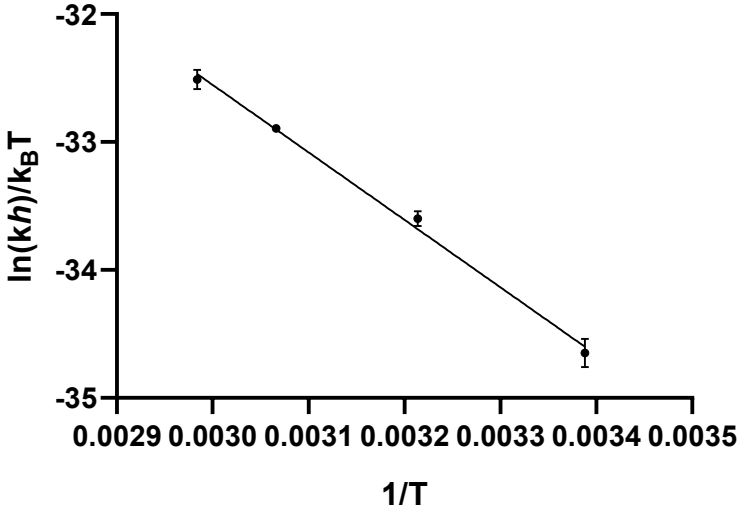

Figure 3.4. Plot of ln(k*h*)/k_BT vs 1/T for the addition of DEC (1a) to AcrPip at increasing temperatures, 22 to 62°C in aqueous buffer (1% v/v DMSO), pH=9.0, μ=0.100. The data were

fitted to a linear regression to provide a slope of -5270 ± 240 and y-intercept of -16.74 ± 0.77, R^2=0.9958.

3.4.6 Ionic strength effect

The corrected second order rates of AcrPip and DEC were also measured in buffers of decreasing ionic strength (μ) from 0.10 to 0.05 M KCl (Figure 5). The sensitivity of the rate constant to the ionic strength of the solvent is commonly used to report on the change in charge distribution from the ground state to the transition state of the reaction. In the case of AcrPip reacting with DEC, the corrected second order rate constants were observed to increase as the ionic strength of the buffer was decreased. The resulting negative slope (Figure 5) implies that the negative charge on the thiolate in the ground state is better stabilized in solutions of higher ionic strength than it is at the transition state, where the charge is dispersed between the thiolate and the conjugated enolate[10,16].

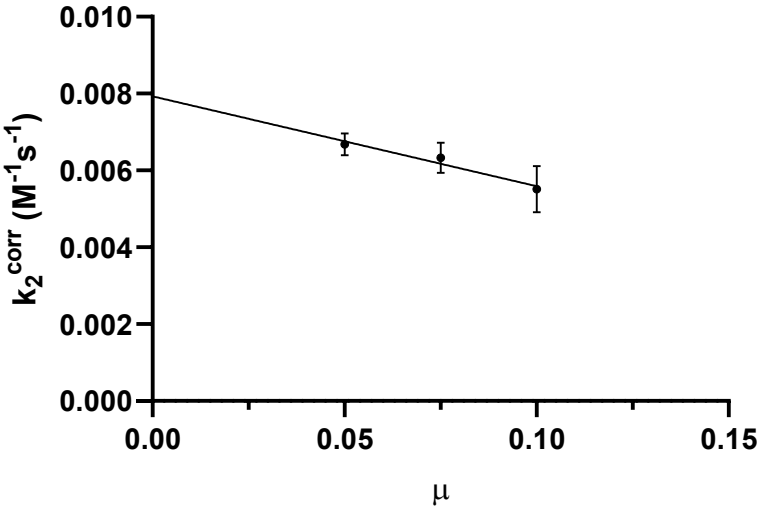

Figure 3.5. Plot of k_2^{corr} ($M^{-1}s^{-1}$) vs ionic strength (μ) for the addition of DEC (1a) to AcrPip at decreasing concentrations of KCl from 0.100 to 0.05 M in aqueous buffer (1% v/v DMSO), pH =

9.0, T=22°C. The data were fitted to a linear regression to provide a negative slope of -0.0234 ± 0.0054, $R^2 = 0.9490$.

3.4.7 Mechanistic interpretation

A thiol addition reaction may be proposed to proceed via three hypothetical mechanisms (see Scheme 2). For example, Mechanism 1 portrays a concerted reaction where addition of thiolate to the β-carbon of AcrPip takes place during the same step as protonation of the α-carbon. Mechanism 2 shows these events as sequential steps, with rate-liming attack preceding protonation. Mechanism 3 features protonation of the α-carbon prior to attack by the thiolate, which seems intuitively unlikely but was considered for the thoroughness of the academic exercise.

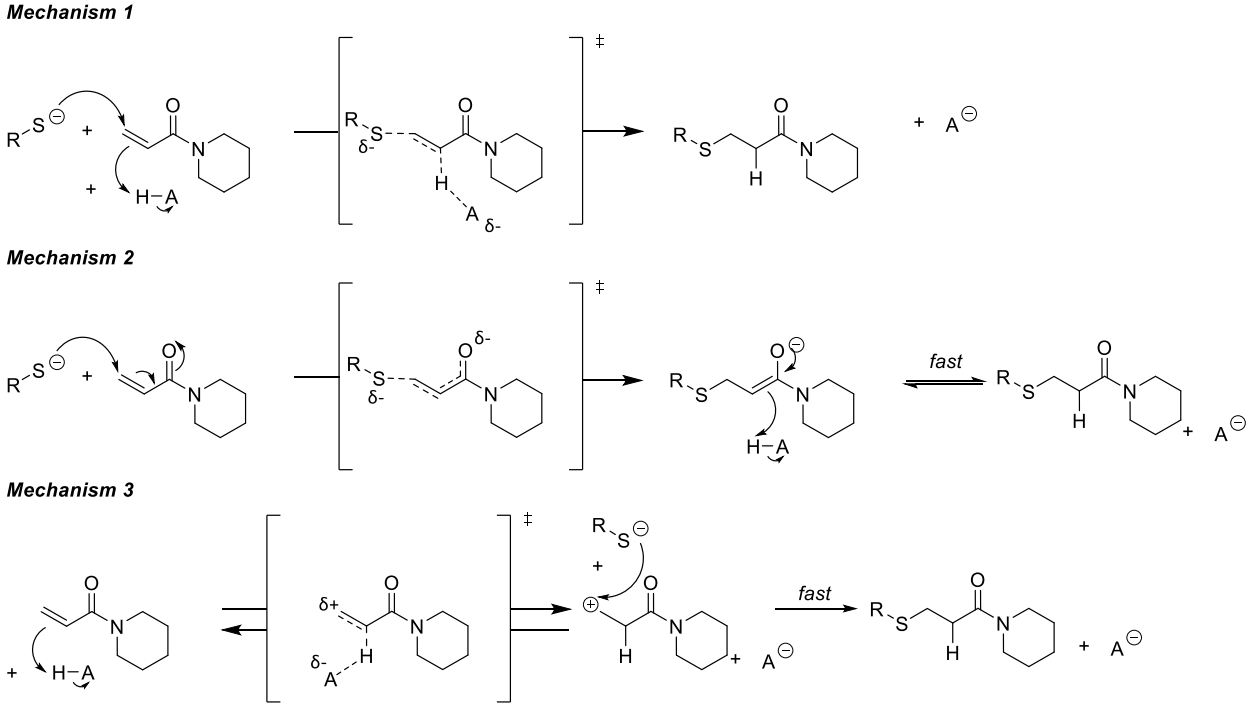

Scheme 3.2. Three proposed mechanisms of thiol addition to AcrPip.

The data shown above in Figure 2 provide a small, positive value for β_{nuc}^{RS-}. This positive value indicates carbon-sulphur bond formation takes place during the rate-limiting step, while its small value suggests that only a small degree of bond formation has occurred at the transition state. Because the slope was determined to be statistically significant from zero, this data set would rule out Mechanism 3, in which no C-S bond formation occurs at the rate-limiting step.

The relatively small kinetic isotope effect measured for the addition reaction indicates that there is minimal proton transfer occurring at the rate-limiting transition state, which would refute both Mechanisms 1 and 3, for which one might expect isotope effects in the range of 3 to 8[15].

The experimental entropy and enthalpy of activation parameters, calculated from the temperature dependence study (Figure 3), point towards a bimolecular transition state that involves both partial bond formation and cleavage. Both Mechanisms 1 and 2 are consistent with this interpretation, whereas Mechanism 3 is not.

Finally, the negative slope measured in the ionic strength study shows that the reaction rate constantly increases as the ionic strength decreases (Figure 4). This is consistent with Mechanisms 1 and 2, where the charge on the attacking thiolate in the ground state becomes more dispersed over the nascent enolate at the transition state.

From the empirical data presented herein, Mechanism 3 can be safely refuted. The data for the most part can be interpreted to support both Mechanisms 1 and 2, which can be thought of as the microscopic reverse of E2 elimination, and the microscopic reverse of the stepwise $E1_{cb}^{rev}$ elimination, respectively. However, the low value for experimental solvent isotope suggests there is no proton in flight at the transition state, refuting Mechanism 1 and confirming Mechanism 2.

In further support of Mechanism 2, we repeated the product study experiment described above, and studied the fate of the DEC+AcrPip adduct product in D_2O, in the presence of an additional 10 eq of carbonate base. After several days, the remaining proton on the alpha carbon disappeared from the spectrum, consistent with deuterium exchange due to reversible carbanion formation[16,17] (see Figure S17, ESI). The reversibility of this deprotonation, without accompanying elimination of thiolate, is consistent with the microscopic reverse of Mechanism 2, rather than Mechanism 1.

3.4.8 Molecular modelling

To explore this reaction further, Mechanism 2 was modelled using density functional theory (DFT). For the reaction of AcrPip with methanethiolate, a transition state was located for thiolate attack on the β-carbon of the AcrPip, having a Cβ–S partial bond length of 2.29 Å. This is consistent with the experimental Brønsted plot that indicated the transition state features a long partial Cβ–S bond and a dispersed charge. The Gibbs energy of activation relative to the thiol and AcrPip reactants was calculated to be 15.7 kcal/mol. This transition state leads to an enolate intermediate that is 12.0 kcal/mol higher in energy than the reactants. Protonation of this enolate intermediate leads to the thioether product. These transition structures are similar to those previously reported by Roseli *et al.*[18], where the Cβ–S bond length is >2.2 Å and the S–CH_3 bond eclipses the C=C bond.[20]

DFT calculations previously reported by Flanagan *et al.*[4] predicted a barrier of 29.5 kcal/mol for the addition of methanethiol to AcrPip. However, it should be noted that these authors used a different computational method (B3LYP/6-311++G(3df,3pd)//SMD) and also used computation to calculate the stability of the thiolate relative to the thiol, whereas we used the experimental pK_a (see ESI).

Ultimately, the enolate must be protonated at the α-carbon to form the thioether product. The α-carbons of enolates are highly basic and will readily abstract a proton from many bases[18]. Computationally, we identified multiple mechanisms by which the AcrPip enolate can abstract a proton from the aqueous solvent, including one low energy path where the solvent was modelled as a cluster of 11 water molecules within the continuum model. The barrier to this reaction step was 9.8 kcal/mol, which is significantly lower than the rate limiting addition step. However, it is likely there are many other low energy paths for the protonation step.

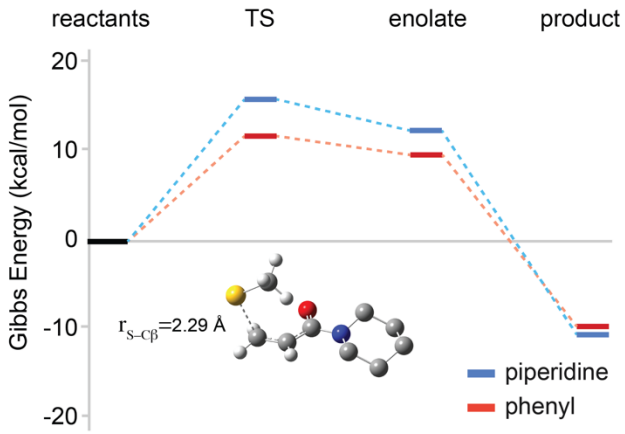

Figure 3.6. Reaction coordinate diagram for the addition of methanethiol to AcrPip in a continuum-model aqueous solvent, shown in comparison to energies previously calculated for *N*-phenylacrylamide[5]. The inset includes an image of the TS, showing a long partial bond (~2.29 Å) between the incoming S and β-carbon.

3.4.9 Mechanistic comparisons

It is informative to compare the proposed mechanism of thiol addition to AcrPip to that recently published for thiol addition to *N*-phenylacrylamide (NPA)[5]. That study also

reported a shallow, positive β_{nuc}^{RS-} value for the reaction of NPA with a panel of alkyl thiols, a relatively small enthalpy and large negative entropy of activation, a small kinetic isotope effect and evidence for the net dispersal of charge moving from the ground state to the transition state. These empirical data confirm that piperidine and aniline acrylamides follow very similar thiol addition reaction mechanisms, both consistent with Mechanism 2. However, side-by-side comparison of second order rate constants shows clearly that NPA reacts 2-fold to 15-fold faster than AcrPip, depending on the thiol. Presumably this order of magnitude acceleration is due to the electron withdrawing effect of the *N*-phenyl ring, by inductive and resonance models, which decreases back donation of electron density from the nitrogen to the carbonyl, effectively increasing the electrophilicity of the β-carbon. This electronic effect is supported by DFT calculations, which predict a lower energy transition state for the reaction of NPA, as shown for comparison in Figure 6.

To provide another level of comparison, we also synthesized *N*-propylacrylamide and measured the k_2^{corr} values for its reaction with a few of the thiols used in this study - namely, DEC, GSH and MPA. For all thiols tested, the reaction with *N*-propylacrylamide was observed to be slightly slower than that of AcrPip (see Table S6). While these experimental data show that the reaction rates for the mono-substituted alkyl acrylamide are consistently slower, it is difficult to explain this trend by electronic effects alone. For example, DFT calculations do not suggest the transition state for thiolate attack on *N*-propylacrylamide is higher in energy than that of the AcrPip reaction. In this case, we suspect that solvation, which is difficult to model by DFT[20,21], may play a more prominent role. More specifically, we hypothesize that the lower reactivity of *N*-propylacrylamide may be due to its ability to act as a hydrogen bond *donor*, in a manner that is inaccessible for AcrPip. According to

this model, solvation of the amide N-H as a hydrogen bond donor may favour the back donation of electron density from the nitrogen to the carbonyl, effectively reducing the electrophilicity of the β-carbon (Scheme S1).

3.5 Conclusions

This study provides experimental evidence consistent with the thiol addition reaction of *N*-acryloylpiperidine (AcrPip) proceeding by a mechanism involving rate-limiting thiolate attack, followed by rapid protonation of the intermediate enolate (Mechanism 2 of Scheme 2). Formally, this is the microscopic reverse of an E1cb elimination reaction. DFT calculations support this mechanistic pathway and provide a model for the transition state that features a long partial C-S bond, which is consistent with the low, positive value derived from the Brønsted-type plot (Figure 3).

This mechanism bears strong resemblance to that recently published for the thiol addition to *N*-phenylacrylamide (NPA). However, it is important to note that NPA reacts roughly 10-fold faster than AcrPip, which in turn reacts several-fold faster than *N*-propylacrylamide. In terms of the design of targeted covalent inhibitors, one successful strategy is to attenuate the reactivity of the electrophilic warhead, thereby increasing its intrinsic stability, such that it only reacts once it is properly positioned in the binding site of its target protein. According to this approach, *N*-alkyl and *N,N*-dialkyl acrylamides may be superior to NPA.

AcrPip also appears to be just as insensitive to thiolate nucleophilicity as NPA, since they both exhibit Brønsted-type plots having shallow positive slopes[5]. This suggests AcrPip warheads only require that a thiol be ionised in order to react efficiently with it, rather than reacting more rapidly with more basic thiolates (as observed for maleimides[10], for example). In the context of drug

design, this means the AcrPip warhead is unlikely to discriminate between Cys residue thiolates of different basicity, and that inhibitor selectivity must be controlled by initial reversible binding with the target protein, based on affinity for the rest of the molecular scaffold.

3.6 Experimental

3.6.1 Synthesis

Reagents and solvents were all purchased from commercial sources and used without further purification. Proton (^{1}H) and carbon (^{13}C) NMR spectra were recorded on a Bruker 400-MHz spectrometer. Chemical shifts were reported in ppm, referenced to the deuterated solvent peak. High resolution mass spectra were recorded with a quadrupole time-of-flight (QTOF) analyzer either by electrospray ionization (ESI) or electron impact (EI) as noted below.

_N_-acryloylpiperidine (AcrPip)

In a flame-dried round-bottom flask, 0.55 mL (5.52 mmol) piperidine and 1.5 mL (8.28 mmol) DIPEA were stirred in 15 mL of DCM. An aliquot of 0.23 mL (2.76 mmol) of acryloyl chloride was diluted in 15 mL DCM. This acryloyl chloride solution was added dropwise to the piperidine and DIPEA solution over 20 min and the reaction was stirred for 1 hour. The DCM was then removed *in vacuo*. The remaining residue was dissolved in EtOAc and washed with 3 × 1 M HCl, 3 × saturated $NaHCO_3$ and brine. It was then dried over Mg_2SO_4, concentrated, and dried over vacuum overnight. The product was recovered as a yellow oil, 292 mg (2.09 mmol), 76% yield.

^{1}H-NMR (400 MHz, $CDCl_3$) δ 6.57 (ddd, J = 16.9, 10.6, 0.9 Hz, 1H), 6.25 (dd, J = 16.9, 1.9 Hz, 1H), 5.66 (dd, J = 10.6, 1.9 Hz, 1H), 3.55 (t, J = 5.5 Hz, 4H), 1.65 (qd, J = 5.5, 2.1 Hz, 2H), 1.58 (tq, J = 8.6, 4.2 Hz, 4H). HRMS (EI) calculated ($C_8H_{13}NO$): 139.0997, found: 139.1002.

3-([2-(diethylamino)ethyl]sulfanyl)-1-(piperidin-1-yl)propan-1-one

^{1}H NMR (400 MHz, D_2O) δ 3.52 – 3.50 (m, 4H), 3.24 – 3.16 (m, 4H), 3.06 (q, *J* = 7.3 Hz, 4H), 2.99 – 2.93 (m, 1H), 2.87 – 2.84 (m, 2H), 1.66 – 1.53 (m, 6H), 1.22 (t, *J* = 7.3 Hz, 6H). HRMS (ESI) calculated ($C_{14}H_{27}N_2OSD$) [M+1]: 274.2063, found [M+1]: 274.2055.

3.6.2 Kinetics

A Fisher Scientific Accumet 15 pH meter was used to determine the concentration of H_3O^+, after calibration with certified standard aqueous buffers of pH 4.00, 7.00, and 10.00.

HPLC traces were collected using a Gilson-Mandel GXP271 high performance liquid chromatography (HPLC) with UV detection at 214 and 254 nm (Phenomenex Luna, 150 mm × 4.6 mm, 30 min, 1.5 mL/min flow rate, variable gradient of 0.1% TFA in CH_3CN/0.1% TFA in H_2O). Elution conditions were adjusted to allow baseline separation of the adduct (see Table S1, ESI).

A stock solution of 0.2 M AcrPip was prepared in DMSO and used throughout the course of the study. Stock solutions each thiol were prepared at 0.2 M in their respective buffers shortly before use. In a 2-mL HPLC vial, 180 µL of 0.2 M thiol stock solution was diluted in 1602 µL of aqueous buffer. Immediately prior to HPLC injection, reactions were initiated by the addition of 18 µL of 0.2 mM AcrPip stock solution. The vials were then inverted to make sure all reagents were properly mixed and placed on the autosampler tray. The HPLC was programmed to take an initial aliquot immediately after the addition of AcrPip and subsequent aliquots were repeatedly injected at pre-determined intervals over the course of the reaction, for at least 5-6 half lives. Each reaction was

run in duplicate unless otherwise noted, and reactions were initiated in a staggered manner to obtain data at the same time points.

The reactions rates for *N*-propylacrylamide were measured in the same fashion as described above for AcrPip, using a stock solution of 0.2 M *N*-propylacrylamide in DMSO and freshly prepared thiol stock solutions of 0.2 M thiol. For the series with *N*-propylacrylamide, only the disappearance of acrylamide over time was monitored. The adduct proved too polar to resolve it from the peak corresponding to DMSO on the chromatogram at 214 nm.

The integrated areas under the adduct peaks of the HPLC chromatograms were found to increase over time, and these AUC values were fitted to a mono-exponential association model with the constraint that $Y_0 = 0$ (Eqn 1).

(1) $$AUC = AUC_{max}(1 - e^{-k_{obs}t})$$

Likewise, the decreasing AUC of the AcrPip peaks from the chromatograms were fitted to a mono-exponential decay model, with the constraint that the lower plateau = 0, unless otherwise noted (Eqn 2).

(2) $$AUC = AUC_0(e^{-k_{obs}t})$$

Replicate pseudo-first order k_{obs} values were measured using both of these methods. Second order rate constants were then calculated by dividing the pseudo-first order rate constants by the concentration of excess thiol (Eqn 3).

(3) $$k_2^{calc} = \frac{k_{obs}}{[thiol]}$$

These second order rate constants were then divided by the fraction of thiolate at the reaction pH given by the corresponding pK_a value of the thiol, to provide the final, corrected second order rate constants (Eqn 4).

(4) $$k_2^{corr} = \frac{k_2^{calc}}{\left(\frac{K_a}{[H^+]+K_a}\right)}$$

For the reactions run in D_2O for the kinetic isotope effect studies, the pD of the solution was calculated according to the meter pH reading as shown in Eqn 5[22].

(5) $$pD = pH + 0.4$$

Thiol pK_a in D_2O was calculated from its pK_a in water, using the equation previously established by Jencks and Salvesen (Eqn 6)[23].

(6) $$\Delta pK = 0.26 + 0.012pK_a$$

3.6.3 DFT Methods

All calculations were performed using Gaussian 16 RevC.01 [24] using the ωB97X-D functional[25] with the def2-TZVP basis set.[26] A continuum conductor-like polarizable continuum *model* (*CPCM*) was used to describe the aqueous solvent. [27,28] The Gibbs energy of deprotonating methanethiol at pH 7 was calculated from the experimental pK_a of methanethiol (10.4) using the relation given in Eqn 7.

(7) $$\Delta G_{deprot} = -RT \times \ln\left(10^{(\mathrm{pH}-\mathrm{pK_a})}\right) = RT \times (\mathrm{pK_a} - \mathrm{pH}) \times \ln(10)$$

The energies of the transition state and the enolate were calculated relative to the methanethiolate and include this energy of deprotonating methanethiol. Each structure was confirmed to be a

stationary point by normal mode analysis, which was also used to apply a standard Gibbs energy correction to the electronic energies.

Conflicts of interest

There are no conflicts to declare.

Acknowledgements

J.W.K. would like to thank the Natural Sciences and Engineering Research Council of Canada (NSERC) and the Canadian Institutes of Health Research (CIHR) for funding. C. N. R. also thanks the NSERC and the Digital Alliance of Canada for computer resources.

3.7 References

1 S. K. I. Watt, J. G. Charlebois, C. N. Rowley and J. W. Keillor, *Org Biomol Chem*, 2023, **21**, 2204–2212.

2 V. J. Cee, L. P. Volak, Y. Chen, M. D. Bartberger, C. Tegley, T. Arvedson, J. McCarter, A. S. Tasker and C. Fotsch, *J Med Chem*, 2015, **58**, 9171–9178.

3 A. Birkholz, D. J. Kopecky, L. P. Volak, M. D. Bartberger, Y. Chen, C. M. Tegley, T. Arvedson, J. D. McCarter, C. Fotsch and V. J. Cee, *J Med Chem*, 2020, **63**, 11602–11614.

4 M. E. Flanagan, J. A. Abramite, D. P. Anderson, A. Aulabaugh, U. P. Dahal, A. M. Gilbert, C. Li, J. Montgomery, S. R. Oppenheimer, T. Ryder, B. P. Schuff, D. P. Uccello, G. S. Walker, Y. Wu, M. F. Brown, J. M. Chen, M. M. Hayward, M. C. Noe, R. S. Obach, L. Philippe, V. Shanmugasundaram, M. J. Shapiro, J. Starr, J. Stroh and Y. Che, *J Med Chem*, 2014, **57**, 10072–10079.

5 S. K. I. Watt, J. G. Charlebois, C. N. Rowley and J. W. Keillor, *Org Biomol Chem*, 2022, **20**, 8898–8906.

6 C. S. Tam, Y. C. Ou, J. Trotman and S. Opat, *Expert Rev Clin Pharmacol*, 2021, **14**, 1329–1344.

7 Y. Y. Syed, *Drugs*, 2020, **80**, 91–97.

8 J. C. Byrd, R. R. Furman, S. E. Coutre, I. W. Flinn, J. A. Burger, K. A. Blum, B. Grant, J. P. Sharman, M. Coleman, W. G. Wierda, J. A. Jones, W. Zhao, N. A. Heerema, A. J. Johnson, J. Sukbuntherng, B. Y. Chang, F. Clow, E. Hedrick, J. J. Buggy, D. F. James and S. O'Brien, *N Engl J Med*, 2013, **369**, 32–42.

9 J. A. Woyach, R. R. Furman, T.-M. Liu, H. G. Ozer, M. Zapatka, A. S. Ruppert, L. Xue, D. H.-H. Li, S. M. Steggerda, M. Versele, S. S. Dave, J. Zhang, A. S. Yilmaz, S. M. Jaglowski, K. A. Blum, A. Lozanski, G. Lozanski, D. F. James, J. C. Barrientos, P. Lichter, S. Stilgenbauer, J. J. Buggy, B. Y. Chang, A. J. Johnson and J. C. Byrd, *N Engl J Med*, 2014, **370**, 2286–2294.

10 M. A. R. Raycroft, K. Racine, C. N. Rowley and J. W. Keillor, *J Org Chem*, 2018, **83**, 11674–11685.

11 R. A. Bednar, *Biochem*, 1990, **29**, 3684–3690.

12 V. Franzen, *Chem Ber*, 1957, **90**, 623–633.

13 A. K. Mitra and M. M. Narurkar, *Int J Pharm*, 1986, **28**, 119–124.

14 J. P. Danehy and K. N. Parameswaran, *J Chem Eng Data*, 1968, **13**, 386–389.

15 F. H. Westheimer, *Chem Rev*, 1961, **61**, 265–273.

16 W. Y. Tsang, B. M. K. Wood, F. M. Wong, W. Wu, J. A. Gerlt, T. L. Amyes and J. P. Richard, *J Am Chem Soc*, 2012, **134**, 14580–14594.

17 T. L. Amyes, B. M. Wood, K. Chan, J. A. Gerlt and J. P. Richard, *J Am Chem Soc*, 2008, **130**, 1574–1575.

18 R. B. Roseli, A. B. Keto and E. H. Krenske, *Wiley Interdiscip Rev Comput Mol Sci*, 2022, 1–16.

19 J. W. Ogilvie, J. T. Tildon and B. S. Strauch, *Biochem,* 1964, **61**, 265-273.

20 J. M. Smith, Y. Jami Alahmadi and C. N. Rowley, *J Chem Theory Comput*, 2013, **9**, 4860–4865.

21 E. Awoonor-Williams, W. C. Isley, S. G. Dale, E. R. Johnson, H. Yu, A. D. Becke, B. Roux and C. N. Rowley, *J Comput Chem*, 2020, **41**, 427–438.

22 M. P. Dale, W. P. Kopfler, I. Chait and L. D. Byers, *Biochem*, 1986, **25**, 2522–2529.

23 W. P. Jencks and K. Salvesen, *J Am Chem Soc*, 1971, **93**, 4433–4436.

24 M. J. Frisch, G. W. Trucks, H. B. Schlegel, G. E. Scuseria, M. a. Robb, J. R. Cheeseman, G. Scalmani, V. Barone, G. a. Petersson, H. Nakatsuji, X. Li, M. Caricato, a. v. Marenich, J. Bloino, B. G. Janesko, R. Gomperts, B. Mennucci, H. P. Hratchian, J. v. Ortiz, a. F. Izmaylov, J. L. Sonnenberg, Williams, F. Ding, F. Lipparini, F. Egidi, J. Goings, B. Peng, A. Petrone, T. Henderson, D. Ranasinghe, V. G. Zakrzewski, J. Gao, N. Rega, G. Zheng, W. Liang, M. Hada, M. Ehara, K. Toyota, R. Fukuda, J. Hasegawa, M. Ishida, T. Nakajima, Y. Honda, O. Kitao, H. Nakai, T. Vreven, K. Throssell, J. a. Montgomery Jr., J. E. Peralta, F. Ogliaro, M. J. Bearpark, J. J. Heyd, E. N. Brothers, K. N. Kudin, V. N. Staroverov, T. a. Keith, R. Kobayashi, J. Normand, K. Raghavachari, a. P. Rendell, J. C. Burant, S. S. Iyengar, J. Tomasi, M. Cossi, J. M. Millam, M. Klene, C. Adamo, R. Cammi, J. W. Ochterski, R. L. Martin, K. Morokuma, O. Farkas, J. B. Foresman and D. J. Fox, Gaussian, Inc., Wallingford CT, 2016.

25 J. da Chai and M. Head-Gordon, *Phys Chem Chem Phys*, 2008, **10**, 6615–6620.

26 F. Weigend and R. Ahlrichs, *Phys Chem Chem Phys*, 2005, **7**, 3297–3305.

27 A. V. Marenich, C. J. Cramer and D. G. Truhlar, *J Phys Chem B*, 2009, **113**, 6378–6396.

28 V. Barone and M. Cossi, *J Phys Chem A*, 1998, **102**, 1995–2001.

Chapter 4 : A kinetic study of thiol addition to *N*-phenylchloroacetamide

Sarah K. I. Watt[a], Janique G. Charlebois[a], Christopher N. Rowley[b], Jeffrey W. Keillor[a]*

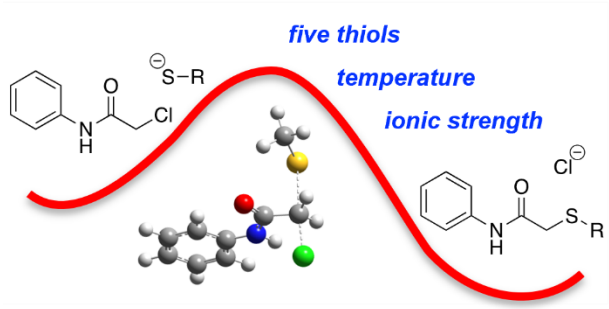

4.1 Statement of Contributions

This manuscript is a collaborative effort between all authors listed in the publication. SKIW contributed to the conceptualization, methodology and experimentation (synthesis, characterization, intrinsic reactivity), and writing. JGC contributed to the methodology and experimentation (synthesis, characterization, intrinsic reactivity) as an undergraduate student under the supervision of SKIW. CNR contributed to the methodology and experimentation (molecular modelling) as well as writing. Finally, JWK contributed to the conceptualization, funding acquisition, supervision, interpretation, and writing. All authors reviewed and edited the work prior to publication.

Reproduced from S. K. I. Watt, J. G. Charlebois, C. N. Rowley, & J. W. Keillor. A kinetic study of thiol addition to *N*-phenylchloroacetamide. *Organic & Biomolecular Chemistry*, 2023, DOI: 10.1039/d3ob00523b [1] with permission from the Royal Society of Chemistry.

4.2 Abstract

Irreversible enzyme inhibitors bind covalently to their target and permanently limit its function. The redox-sensitive thiol group on the side chain of cysteine (Cys) residues is often the nucleophilic group that is targeted for reaction with the electrophilic warhead of irreversible inhibitors. While the acrylamide group is the warhead applied most frequently currently in the design of inhibitors with therapeutic potential, the chloroacetamide group offers a comparable reactivity profile. In that context, we have studied the details of the mechanism of thiol addition to *N*-phenylchloroacetamide (NPC). A kinetic assay was developed to accurately monitor reaction progress between NPC and a small library of thiols with varying pK_a values. From these data a Brønsted-type plot was constructed, from which a β_{nuc}^{RS-} value of 0.22 ± 0.07 was derived, indicative of a relatively early transition state with respect to attack by the thiolate. The halide leaving group was also varied, for the reaction with one thiol, providing rate constants consistent with a transition state that is early with respect to leaving group departure, as well. The effects of temperature and ionic strength were also studied, and all data are consistent with an early transition state for a concerted S_N2 mechanism of addition. Molecular modelling was also performed, and these calculations confirm the concerted transition state and relative reactivity of the haloacetamides. Finally, this study allows a detailed comparison of the reactivity and reaction mechanisms of the chloroacetamide group with the benchmark acrylamides used in many irreversible inhibitor drugs.

Keywords: acrylamide, chloroacetamide, irreversible inhibitor, glutathione, thiol-addition

4.3 Introduction

Irreversible enzyme inhibitors are designed to target nucleophilic residues within the active site of an enzyme, covalently binding to their target and irreversibly modifying their function. Cysteine (Cys) residues are commonly the target of these inhibitors, since they present a highly nucleophilic and redox sensitive thiol group[2]. These inhibitors contain an electrophilic 'warhead' that reacts to form covalent bond, only after the scaffold of the inhibitor has selectively bound the active site of interest. Currently, many electrophilic warheads in clinical application make use of the acrylamide group[3–12], but other emerging electrophilic warheads may also present a reactivity profile of therapeutic potential, one of which is chloroacetamide.

Chloroacetamides are an electrophilic group well known to react readily with thiols under aqueous conditions[13]. However, although they are relatively stable under physiological aqueous conditions, concerns over their *in vivo* biostability have been expressed[14,15]. Instead, they have better lent themselves as functional cysteine-reactive probes[16,17]. The less reactive chlorofluoroacetamide has also been explored as a more stable alternative warhead[18,19] although the addition of fluorine may prove to be detrimental to binding affinity[19]. Despite these challenges, the α-chloroacetamide derivatives remain of particular interest and are still included in screening campaigns along with their acrylamide counterparts where, in some cases, they prove to be superior[15,18,20–23]. Chloroacetamide derivatives have also been identified to be some of the most potent GPx4 inhibitors (see Figure 1)[14].

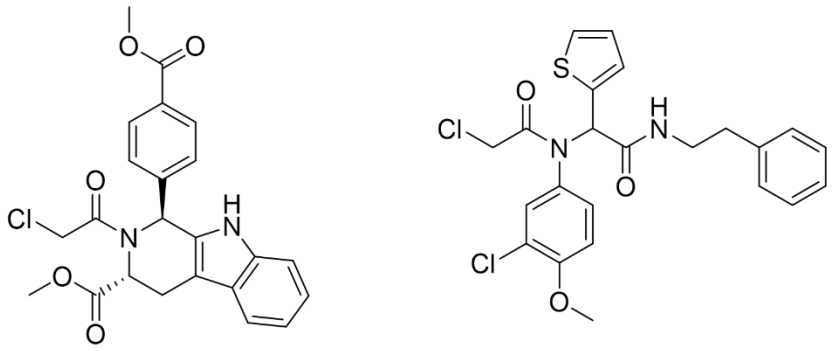

Figure 4.1. Examples of potent GPx4 irreversible enzyme inhibitors featuring the chloroacetamide warhead.

In this work we have studied in detail the intrinsic reactivity of the *N*-phenylchloroacetamide (NPC) warhead with a series of thiolates covering a broad range of basicity/nucleophilicity. The effect of temperature and ionic strength were also studied, allowing us to provide details on the (S_N2) mechanism of addition. Leaving group effects were also explored, and the transition state was further characterized by DFT calculations. This study follows our recent publications on the mechanistic studies of thiol addition *N*-phenylacrylamide[24] and *N*-acryloylpiperidine[25], thereby allowing us to compare the intrinsic reactivity profiles of the most broadly applied acrylamide warheads[2,26] to the much less utilized chloroacetamide warhead.

4.4 Results and Discussion

4.4.1 Product studies

N-phenylchloroacetamide (NPC) was first prepared by the dropwise addition of chloroacetyl chloride to a stirred solution of aniline and diisopropylethylamine in dichloromethane (see Experimental). We then studied the product of the reaction of NPC with *N*,*N*-diethylcysteamine (DEC), to confirm the identity and expected structure of the NPC-DEC adduct. For this experiment, DEC was dissolved in carbonate buffer prepared in D_2O (pD = 9.6). An initial ^{1}H-NMR spectrum was recorded to identify the protons corresponding to the free thiol. The reaction was then initiated through the addition of NPC dissolved in acetonitrile. Acetonitrile was used as co-solvent in this experiment, rather than DMSO, because the residual solvent peak of DMSO obscures the proton signals from the chloroacetamide and thiol. The initiated reaction was then monitored by ^{1}H-NMR by recording spectra after 15 minutes of incubation at room temperature and again after 2 hours, at which point the complete disappearance of starting chloroacetamide was observed. The consumption of NPC was followed by the displacement of the α protons of the reactant chloroacetamide from 4.34 to 3.57 ppm. The resulting ^{1}H-NMR spectrum was further analyzed to assign all remaining proton signals to the final adduct structure (see Figure 2). Trace amounts of residual reactant DEC were assigned by comparing to a reference spectrum of DEC recorded under the same conditions. After the reaction was deemed complete by NMR, an aliquot was injected onto the HPLC, thereby confirming the retention time of the adduct with that observed from kinetic experiments in protonated buffer (see below). The material giving rise to the adduct HPLC peak was also isolated and characterized by high-resolution mass spectroscopy to confirm its identity (see Experimental).

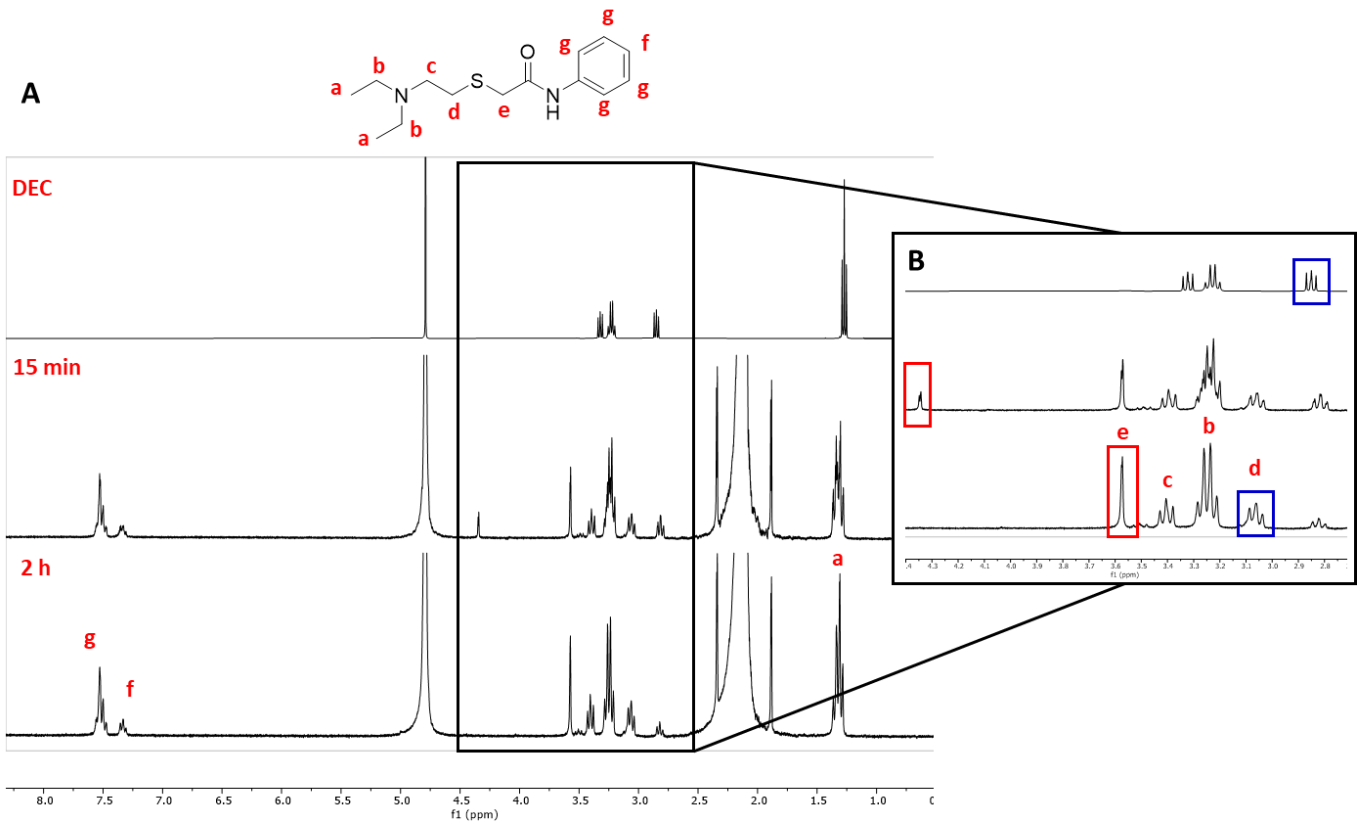

Figure 4.2. (A) ^{1}H-NMR spectra recorded before initiation (thiol only, top), 15 minutes after initiation (middle), and 2 hours after initiation (bottom) of the reaction between DEC and NPC. **(B)** Expanded region of the ^{1}H-NMR spectrum highlighting in red the upfield shift of the signal from 4.34 to 3.57 ppm corresponding to the protons of the acetamide methylene (e) undergoing nucleophilic attack. Highlighted in blue is the downfield shift from 2.82 to 3.06 ppm for the protons of the methylene adjacent to the attacking DEC thiolate (d).

4.4.2 Kinetic studies by HPLC

Second order rate constants were then measured for the reaction of NPC with a series of thiols (Scheme 1) presenting a wide range of basicity/nucleophilicity (Table 1).

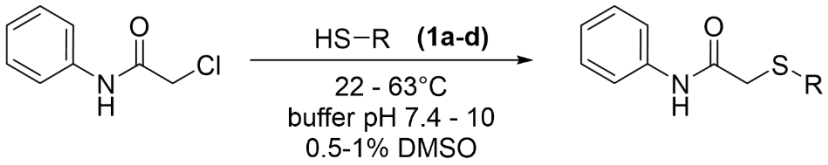

R =
a) $CH_2CH_2NEt_2$
b) $CH_2CH(C(O)NHCH_2CO_2H)NHC(O)CH_2CH_2CH(NH_2)CO_2H$
c) CH_2CH_2OH
d) $CH_2CH_2CO_2H$

Scheme 4.1. General scheme and reaction conditions for the addition of NPC to thiols 1a-d.

Table 4.1. Structures, names and thiol pK_a values for thiols **1a-d**.

Thiol	Structure	Name	Thiol pK_a
1a	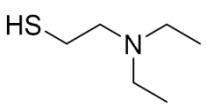	*N,N*-diethylcysteamine (DEC)	7.8 [27]
1b	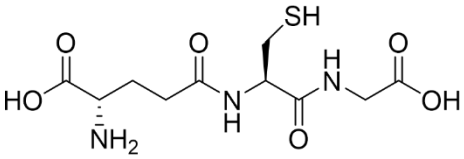	glutathione (GSH)	8.66 [28]
1c	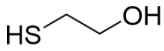	β-mercaptoethanol (BME)	9.58 [29]
1d	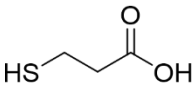	3-mercaptopropionic acid (MPA)	10.27 [29]

Stock solutions of 0.2 M thiol were freshly prepared in their respective reaction buffers (see Table 5, Experimental) just before use, and a 0.2 M stock solution of NPC was prepared in DMSO for use throughout the course of the study. In 2-mL HPLC vials fitted with a pre-slit screw-top cap, the working stock solution of thiol was diluted in the corresponding reaction buffer (see Table S1, ESI) to a final concentration of either 10 or 20 mM, depending on the thiol. The reaction was initiated by addition of NPC dissolved in DMSO, to a final concentration of 1 or 2 mM in accordance with the concentration of thiol used, to maintain a 10-fold ratio of thiol over NPC. Thiol reactants were used in large excess in order to minimize any noise in the observed reaction

rates due to the background formation of disulfides, while also allowing for pseudo first order rate constants (k_{obs}) to be measured.

Reaction progress was monitored by high-performance liquid chromatography (HPLC), following both the disappearance of NPC and simultaneous formation of thiol adduct, by variation of the area under the curve (AUC) for each respective peak, measured at 214 nm. The AUC data was plotted against time, and the resulting plots were fitted to a mono-exponential decay equation for the disappearance of the electrophile and a mono-exponential association equation for the appearance of thiol-adduct formed. These fittings afforded the pseudo-first order rate constant k_{obs} values, that were then used to calculate the second order rate constants (k_2^{calc}, Table 2), by dividing k_{obs} by the quasi-constant concentration of excess thiol. We and others have shown [24,30] that the negatively charged thiolate is the reactive nucleophilic species, which allows us to correct the k_2^{calc} values by dividing by the proportion of thiolate in solution (*f* RS-, Table 2), allowing for direct comparison of the corrected rate constants (k_2^{corr}, Table 2) measured for thiols of varying pK_a values. The stability of NPC in aqueous buffer in the absence of thiol was confirmed over a 24-h period (see Figure S1), corresponding to the length as the longest kinetic experiments performed herein. This provides confidence that we can attribute the disappearance of chloroacetamide observed in our kinetic experiments with its reaction with the thiolate present in solution. The reported standard deviations (see Table S2) account for the propagation of uncertainty, including those of the pH and pK_a values used in the calculation (see Experimental). The errors shown for the average k_2^{corr} values reported in Table 2 account for the uncertainties in the four replicate rate constants measured for both the appearance of adduct and disappearance of NPC throughout the kinetic assay.

4.4.3 Brønsted-type plot

The kinetic method described above was applied to all four thiols shown in Table 1 and the log value of the corrected second order rate constant (k_2^{corr}) was plotted against pK_a for each respective thiol. The resulting plot was then fitted to a linear regression model to reveal a β_{nuc}^{RS-} value of 0.21 ± 0.07 (Figure 3). The data were treated by statistical analysis using ANOVA to determine that the slope is indeed statistically significantly different from zero at the $\alpha = 0.05$ level, (*P* value = 0.0120). This positive, non-zero slope indicates that partial bond formation between the sulphur of the attacking thiolate and the electrophilic alpha carbon of the acetamide does occur at the rate limiting transition state. The shallow slope indicates that there is limited *decrease* of negative charge on the incoming sulphur at the transition state, suggestive of an early transition state, with respect to C-S bond formation. The shallow slope also indicates the nucleophilicity of the incoming thiolate does not have a pronounced effect on the rate constant of the displacement reaction, presumably because the electrophile is relatively activated.

Table 4.2. Calculated values for the fraction of thiolate in solution (*f* RS^-), second order rate constants (k_2^{calc}), and corrected second order rate constants (k_2^{corr}) for the addition of RSH (**1a-d**) to NPC. Measurements were made in duplicate for both the disappearance of chloroacetamide and appearance of adduct. Errors reported for *f* RS^- represent the propagation of uncertainty in the reported pK_a values and the experimental pH values. Errors reported for k_2^{corr} represent the propagated uncertainty from the four replicate measurements.

Thiol	***f* RS^-**	**k_2^{calc} ($M^{-1}s^{-1}$)**	**k_2^{corr} ($M^{-1}s^{-1}$)**
1a	0.0909 ± 0.0237	0.01491 ± 0.00037	0.164 ± 0.022
1b	0.0521 ± 0.0065	0.004333 ± 0.000033	0.0832 ± 0.0052
1c	0.0256 ± 0.0033	0.01599 ± 0.00027	0.624 ± 0.041
1d	0.0521 ± 0.0065	0.01596 ± 0.00023	0.306 ± 0.020

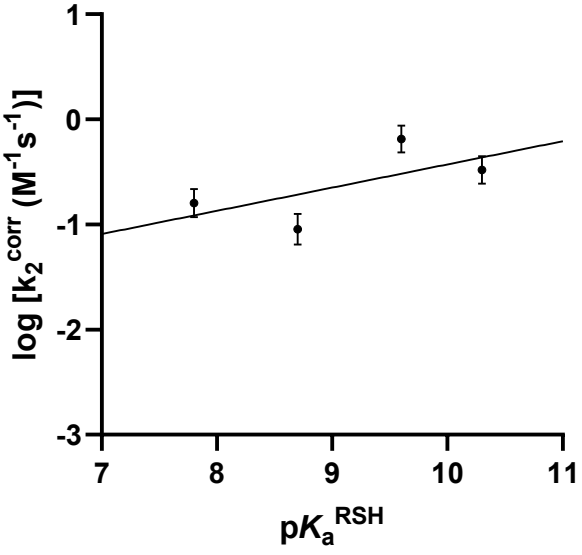

Figure 4.3. Brønsted-type plot of $\log(k_2^{corr})$ vs pK_a^{RSH} for the addition of RSH (thiols 1a-d) to NPC in aqueous buffer (0.5-1.0% v/v DMSO), μ=0.100, T=22°C. The data were fitted by linear regression to provide a slope β_{nuc}^{RS-} value of 0.21 ± 0.07.

4.4.4 Temperature dependence

The addition of thiol **1d** to NPC was also studied over a range of temperature, from 22 ℃ to 62 ℃. These reactions were run in the same manner as described above, except the vials containing the reaction mixture were incubated in a heated water bath, then manually transferred to the autosampler tray prior to injection. The vials were also inverted periodically to collect all condensate. The corrected second order rate constants obtained in this manner were used to construct an Eyring plot (Figure 4). The linear fit of this plot allows for the calculation of the entropy ($\Delta S^{\ddagger}$) and enthalpy ($\Delta H^{\ddagger}$) of activation parameters for this reaction, y-axis intercept and the slope of the best fit straight line, respectively. The large negative $\Delta S^{\ddagger}$ calculated in this manner (-26.1 ± 0.9 cal mol^{-1} K^{-1}) is indicative of a highly ordered transition state relative to the ground

state. This is consistent with a concerted transition state featuring simultaneous attack by thiolate nucleophile and departure of the chloride leaving group. The relatively low calculated $\Delta H^{\ddagger}$ (10.2 ± 0.3 kcal mol^{-1}) signifies little change in bond order at the rate-limiting transition state, consistent with concerted partial formation of the C-S sigma bond and partial cleavage of the C-Cl sigma bond (see Scheme 2).

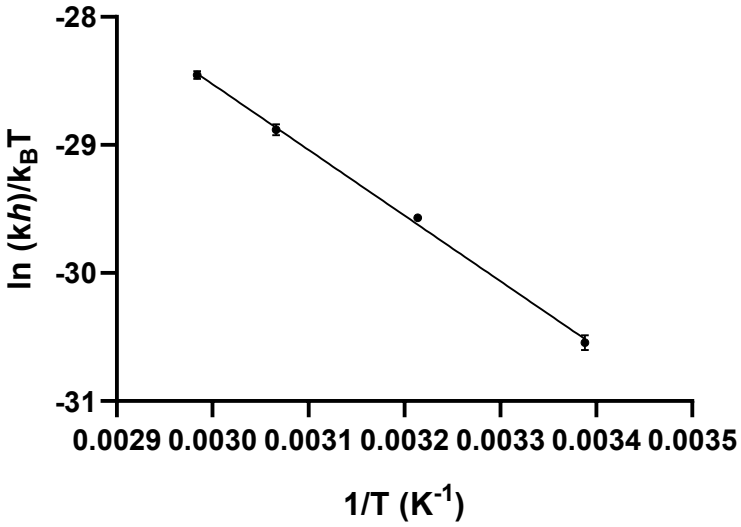

Figure 4.4. Eyring plot of $\ln(k\mathit{h})/k_BT$ vs 1/T for the addition of 1d to NPC in aqueous buffer (0.5% v/v DMSO), μ=0.100, pH=9.0. The data were fitted to a linear regression with a slope of -5126 ± 146, y-intercept of -13.2 ± 0.5 and R^2 of 0.9984.

4.4.5 Ionic strength effect

The effect of ionic strength (μ) of the reaction buffer on the corrected second order rates was also probed, by decreasing the salt concentration from 0.1 M to 0.05 M KCl. The decrease in ionic strength of the reaction buffer can be correlated to an observed increase in the corrected second order rates, as seen from the negative slope of Figure 5. At higher salt concentrations, the negatively charged thiolate species would be stabilized more effectively in solution. This ground state stabilization would lead to slower reactions exhibiting smaller k_2^{corr} values. This is consistent with ion strength effects observed for reactions where localized negative charge on reactant is dispersed over a more diffusely charged system at the transition state [31,32]. For this specific reaction, the ionic effects are consistent with those expected for an S_N2 mechanism, in which the negatively charged thiolate attacks the alpha carbon of the neutral acetamide, leading to partial negative charges over the sulphur and chloride atoms at the transition state.

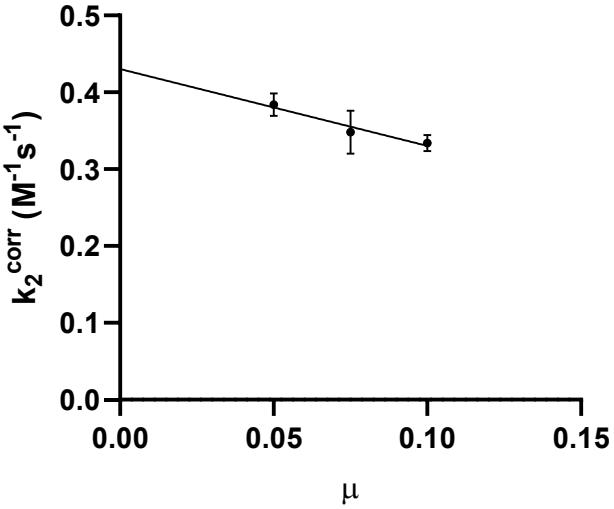

Figure 4.5. Plot of k_2^{corr} ($M^{-1}s^{-1}$) vs μ for the addition of 1d to NPC in aqueous buffer (0.5% v/v DMSO), T=22°C, pH=9.0. The data were fitted to a linear regression to afford a slope of -1.00 ± 0.25, y-intercept of 0.43 ± 0.02 and R^2 of 0.9394.

4.4.6 Leaving group effects

In a concerted S_N2 reaction, the departing leaving group is also expected to affect reaction rate. To study the leaving group effects in the thiol addition reaction of *N*-phenylhaloacetamides, we synthesized *N*-phenylbromoacetamide and *N*-phenyliodoacetamide, and measured their intrinsic reactivity with MPA (thiol **1d**). Corrected second order rate constants were measured for these two new acetamide derivatives in the same manner as for the chloroacetamide derivative, and are presented in Table 3. As expected, these second order rate constants are lower for the more basic halides, and increase with the nucleofugality of the leaving group. This variation of second order rate constant as a function of nucleofugality is consistent with the departure of leaving

group during the rate-limiting step, as expected for a concerted displacement (S_N2) mechanism.

Table 4.3. Corrected second order rate constants (k_2^{corr}) for the addition of MPA (**1d**) to *N*-phenylchloroacetamide, *N*-phenylbromoacetamide, and *N*-phenyliodoacetamide, and DFT-calculated activation energies ($\Delta G^{\ddagger}_{calc}$) for the addition of methanethiol. Errors represent the standard deviation of the replicate values for both the disappearance of acetamide and appearance of adduct.

Parameter	***N*-phenyl chloroacetamide**	***N*-phenyl bromoacetamide**	***N*-phenyl iodoacetamide**
k_2^{corr} ($M^{-1}s^{-1}$)	0.306 ± 0.020	0.988 ± 0.189	32.2 ± 4.5
$\Delta G^{\ddagger}_{calc}$ (kcal·mol^{-1})	19.1	14.7	14.4

In a previous study[33] by Flanagan *et al.*, pseudo-first order rate constants were measured at 37 ℃ and pH 7.4 for the addition of 10 mM GSH to 1 mM of *N*-methylchloroacetamide and *N*-methylbromoacetamide, and reported to be 0.0036 min^{-1} and >0.140 min^{-1} respectively. Treating these rate constants in the same manner as those reported in this study affords k_2^{corr} values of 0.126 $M^{-1}s^{-1}$ and >4.89 $M^{-1}s^{-1}$, respectively. While no direct comparison can be made between these *N*-methyl haloacetamides and the *N*-phenyl haloacetamides studied herein, the same trend in reactivity (Br > Cl) and effect of leaving group is observed.

4.4.7 Mechanistic interpretation

All of the detailed data presented above are consistent with the S_N2 mechanism intuitively expected for this addition reaction. The shallow, positive Brønsted-type plot is indicative of partial C-S sigma bond formation at the rate limiting transition state. Ion strength effects also suggest the negative charge of the attacking thiolate is dispersed over a broader system at the transition state. The $\Delta S^{\ddagger}$ and $\Delta H^{\ddagger}$ values provided by the temperature studies also point to a highly ordered bimolecular transition state, and a relatively low net change in bond order due to simultaneous bond making and bond breaking events, respectively.

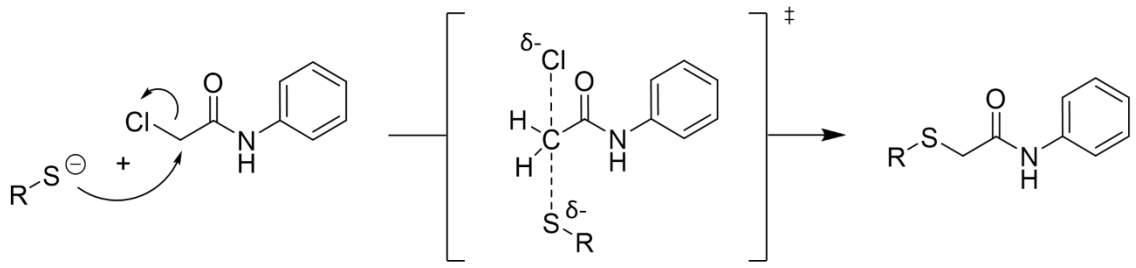

Scheme 4.2. Proposed S_N2 mechanism for thiol addition to NPC.

4.4.8 Molecular modelling

To better understand the reaction mechanism, we performed density functional theory (DFT) modelling of the reaction of *N*-phenylchloroacetamide, *N*-phenylbromoacetamide and *N*-phenyliodoacetamide with methanethiol. The details of the computational methods are included in the Experimental section (see below) and the Cartesian coordinates of the optimized structures are included in Table S5, ESI.

Although the LUMO of the *N*-phenylchloroacetamide corresponds to a π*(C=O) orbital, we could not identify any low energy reaction paths or intermediate corresponding to an attack on the carbonyl carbon. Instead, the only low energy transition state we identified is that of a concerted S_N2-type mechanism where the methanethiolate attacks the LUMO+2, corresponding to a σ*(C–X) orbital on the halo-substituted carbon (Figure 6). The calculated transition state structure is consistent with the experimental Eyring analysis which found that the reaction proceeds through an ordered, associative transition state with a modest net decrease in bonding.

The trend in calculated activation energies (see $\Delta G^{\ddagger}_{calc}$ Table 3: Cl > Br > I) is consistent with the trend observed for the experimentally measured rate constants (see k_2^{corr} Table 3: Cl < Br < I). The lower strength of the C–Br and C–I bonds results in a lower activation energy for their displacement by thiolate. The corresponding rate constants calculated from these DFT-calculated activation energies using Eyring transition state theory (see ESI Table S6) are lower than the experimental values by 1–3 orders of magnitude, suggesting the calculated activation energies are overestimated. Our experimental data indicate the differences between the Cl and Br/I activation energies should be larger in magnitude than the calculated differences, and that there should be a larger difference between the activation energies calculated for the iodo and bromo acetamides.

To test if our DFT calculations were consistent with our ionic strength experiments, we repeated these calculations using a continuum solvent model for dichloromethane instead of water. The calculated activation energies are systematically lower in the DCM models (see ESI Table S7), consistent with the activation energy increasing when the energetic cost of desolvating the thiolate increases in higher-dielectric solutions. However, the calculated reaction barriers are highly sensitive to the treatment of solvation and the optimal atomic radii of halogens are still the

subject of debate,[34] so ultimately simulation methods with explicit solvents may be needed to calculate reaction rates that are in quantitative agreement with experiment.

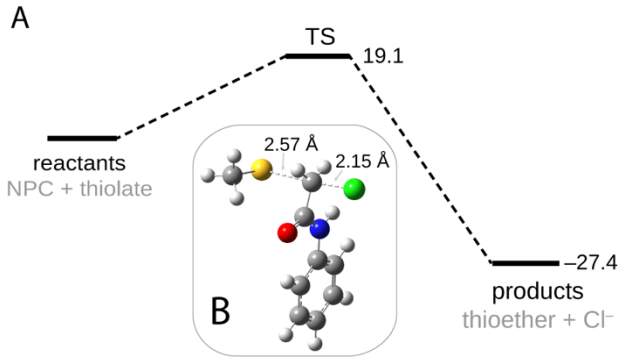

Figure 4.6. (A) Calculated reaction profile for the S_N2 reaction of chloroacetamide with methanethiol. Calculated Gibbs energies in kcal·mol^{-1} are shown for the transition state and products. **(B)** Structure of calculated transition state. The lengths of the partial C--S and C--Cl bonds are shown. All values were calculated using ωB97X-D/def2-TZVP-CPCM.

4.4.9 Comparison of addition mechanisms

Our recent investigations [24,25], of the mechanisms of addition of thiols to acrylamides allows an interesting point of reference for comparison with the results of the present study. For example, chloroacetamide shows a similar intrinsic reactivity as *N*-phenylacrylamide (NPA), but reacts significantly faster than *N*-acryloylpiperidine (AcrPip) and *N*-propylacrylamide (Table 4).

Table 4.4. Corrected second order rate constants (k_2^{corr}) for the addition of thiols to *N*-phenylchloroacetamide (NPC), *N*-phenylacrylamide (NPA), *N*-acryloylpiperidine (Acr-Pip), and *N*-propylacrylamide (NPrA).

Thiol	**k_2^{corr} ($M^{-1}s^{-1} \times 10^3$)**			
	***N*-phenylchloroacetamide (NPC)**	***N*-phenylacrylamide (NPA)[23]**	***N*-acryloylpiperidine (Acr-Pip)[24]**	***N*-propylacrylamide (NPrA)[24]**
DEC	164 ± 22	130 ± 10	5.51 ± 0.61	2.13 ± 0.03
Cys	n.d.	61 ± 6	9.77 ± 0.97	n.d.
GSH	83.2 ± 5.2	86 ± 5	8.24 ± 1.21	n.d.
BME	624 ± 41	220 ± 8	14.8 ± 0.7	8.64 ± 0.17
MPA	306 ± 20	118 ± 4	10.5 ± 0.9	3.48 ± 0.25

Considering data obtained from temperature studies of all three warhead derivatives, a temperature dependence plot can also be constructed that shows their respective activation energies at different temperatures (Figure 7). From this graph we can see that AcrPip reacts consistently more slowly than both NPA and NPC, over all biologically relevant temperatures. More interestingly, at low temperatures NPA is predicted to react faster than NPC, but at all temperatures near 37 °C, the chloroacetamide reacts faster than NPA.

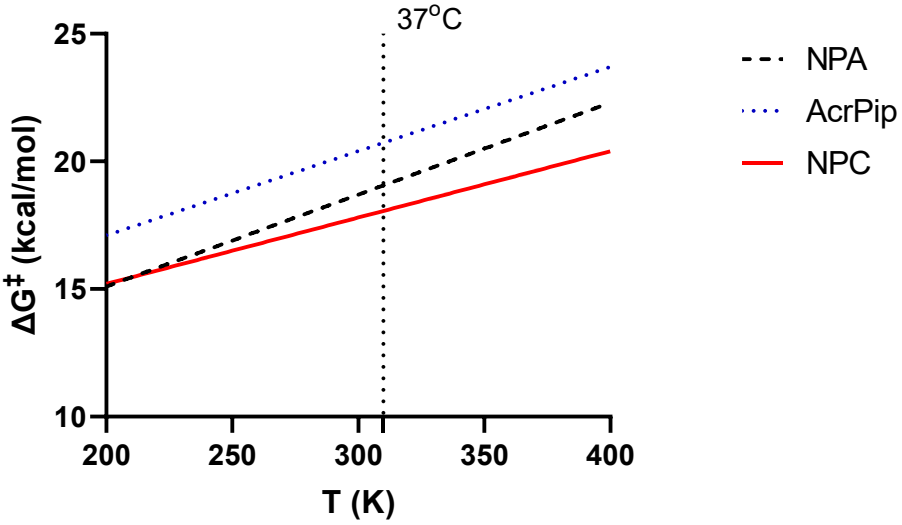

Figure 4.7. Plot of $\Delta G^{\ddagger}$ vs T for NPA, AcrPip, and NPC. $\Delta G^{\ddagger}$ was calculated using the enthalpy ($\Delta H^{\ddagger}$) and entropy ($\Delta S^{\ddagger}$) of activation parameters determined from the Eyring plot for each warhead derivative.

4.5 Conclusions

This study provides multiple lines of evidence consistent with the proposed S_N2 mechanism of thiol addition to *N*-phenylchloroacetamide. The shallow, positive Brønsted-type slope (Figure 3) is indicative of an early transition state in which the negative charge on the attacking thiolate sulfur has not been decreased appreciably at the transition state. It is also important to note that NPC's relative insensitivity to thiolate nucleophilicity means the warhead would not discriminate strongly between different protein thiolates. Rather, they are predicted to react similarly with any ionised thiolate. In the context of therapeutic application of NPC inhibitors, this intrinsic reactivity underlines the importance of designing the inhibitor to be complimentary to the binding site adjacent to the targeted Cys residue, in order to ensure selectivity.

The reactivity of NPC can also be compared with that of acrylamide warheads NPA[24] and AcrPip[25]. All three of these electrophilic warheads are relatively insensitive to thiolate nucleophilicity, presenting Brønsted-type plots with shallow positive slopes. NPC shows higher intrinsic reactivity than the acrylamides and the enthalpy and entropy of activation suggest that this would hold true over a broad range of temperatures (Figure 7). As discussed above, the higher intrinsic reactivity of NPC may also explain its lower *in vivo* stability, relative to its acrylamide counterparts.

4.6 Experimental

4.6.1 Synthesis

General comments

Reagents and solvents were all purchased from commercial sources and used without further purification. Proton (^{1}H) and carbon (^{13}C) NMR spectra were recorded on a Bruker 400-MHz spectrometer. Chemical shifts were reported in ppm, referenced to the deuterated solvent peak. High resolution mass spectra were recorded with a quadrupole time-of-flight (QTOF) analyzer either by electrospray ionization (ESI) or electron impact (EI) as noted below.

***N*-phenylchloroacetamide (NPC)**

In a flame-dried, round-bottom flask, 0.4 mL (4.42 mmol) aniline and 1.15 mL (6.63 mmol) DIPEA were dissolved in 15 mL DCM. Separately, 0.18 mL (2.21 mmol) chloroacetyl chloride was dissolved in 15 mL DCM and then added to the dissolved aniline dropwise over 10 min. The reaction mixture was stirred for 2 hours. The reaction mixture was washed with 3 × 1 M HCl, 3 × saturated $NaHCO_3$ and brine, then dried over Mg_2SO_4, concentrated *in vacuo*, and purified by flash column chromatography (25% EtOAc in Hexanes). The product was recovered as a reddish-brown solid, 291 mg (1.72 mmol), 78% yield.

^{1}H-NMR (400 MHz, $CDCl_3$) δ 7.55 – 7.51 (m, 2H), 7.37 – 7.32 (m, 2H), 7.18 – 7.32 (m, 1H), 4.18 (s, 2H). ^{13}C-NMR (101 MHz, CDCl3) δ 163.95, 136.85, 129.33, 125.44, 120.30, 43.06. HRMS (EI) calculated (C_8H_8ClNO): 169.0294, found: 169.0299.

2-([2-diethylamino)ethyl]sulfanyl)-*N*-phenylacetamide

A 0.1 M stock solution of DEC was freshly prepared in carbonate buffer using D_2O (pD = 9.6) and a 0.1 M stock solution of NPC was prepared in acetonitrile. In a 1.5 mL Eppendorf tube, 20 μL of 0.1 M DEC stock solution was dissolved in 960 μL carbonate buffer prepared in D_2O. The reaction mixture was vortexed briefly and transferred to an NMR tube. An initial ^{1}H-NMR spectrum was taken. To initiate the reaction, 20 μL of 0.1 M NPC stock solution was added to the NMR tube, and the reaction monitored by ^{1}H-NMR over the course of 2 hours. Once the reaction was deemed complete by NMR, an aliquot was injected onto the HPLC. The adduct peak was collected and analyzed by high-resolution mass spectrometry to confirm its identity as the expected adduct.

^{1}H NMR (400 MHz, D_2O) δ 7.53 – 7.46 (m, 4H), 7.33 – 7.29 (m, 1H), 3.55 (s, 2H), 3.41 – 3.37 (m, 2H), 3.26 – 3.20 (m, 6H), 3.05 – 3.02 (m, 2H), 1.34 – 1.27 (m, 6H). HRMS (ESI) calculated ($C_{14}H_{22}N_2OS$): 267.1531, found: 267.1524.

4.6.2 Kinetics

A Fisher Scientific Accumet 15 pH meter was used to determine the concentration of H_3O^+, after calibration with certified standard aqueous buffers of pH 4.00, 7.00, and 10.00. HPLC traces were collected using a Gilson-Mandel GXP271 high performance liquid chromatography (HPLC) with UV detection at 214 and 254 nm (Phenomenex Luna, 150 mm × 4.6 mm, 30 min, 1.5 mL/min flow rate, variable gradient of 0.1% TFA in CH_3CN/0.1% TFA in H_2O). Elution conditions were adjusted to allow baseline separation of the adduct (see Table S1, ESI).

A stock solution of 0.2 M NPC was prepared in DMSO and used throughout the course of the study. Working stock solutions of each thiol were prepared at 0.2 M in their respective buffers shortly before use (Table 5). The thiol was dissolved in reaction buffer to the appropriate concentration, then immediately before injection of the HPLC the reaction was initiated through addition of the stock solution of NPC in DMSO. To ensure proper mixing of reagents, the vials were inverted after initiation, and the vial was then placed on the autosampler tray. An initial aliquot was taken, and subsequent aliquots were injected at pre-determined time points over the duration of the reaction being monitored, at least 5 half-lives.

Table 4.5. Buffers used for the reaction of each thiol.

Thiol	**[NPC] (mM)**	**[Thiol] (mM)**	**pH of Aqueous Buffer**	**Reaction Buffer**
1a	2	20	6.80	67 mM MOPS
1b	1	10	7.40	67 mM potassium phosphate
1c	2	20	8.00	67 mM Tris
1d	1	10	9.01	67 mM CHES

The integrated areas of the peaks (AUC) corresponding to the adducts on the HPLC chromatograms were found to increase over time, and these AUC values were fitted to a mono-exponential association model with the constraint that the initial value was zero (Eqn 1).

(1) $$AUC = AUC_{max}(1 - e^{-k_{obs}t})$$

Likewise, the AUC of the NPC peaks from the chromatograms were observed to decrease with time, and were fitted to a mono-exponential decay model, with the constraint that the lower plateau was zero (Eqn 2).

(2) $$AUC = AUC_0(e^{-k_{obs}t})$$

Replicate pseudo-first order k_{obs} values were measured using both of these methods. Second order rate constants were then calculated by dividing the pseudo-first order rate constants by the concentration of excess thiol (Eqn 3).

(3) $$k_2^{calc} = \frac{k_{obs}}{[thiol]}$$

The second order rate constants were then divided by the fraction of thiolate at the reaction pH given by the corresponding pK_a value of the thiol, to provide the final, corrected second order rate constants (Eqn 4).

(4) $$k_2^{corr} = \frac{k_2^{calc}}{f\ \mathrm{RS}^-} = \frac{k_2^{calc}}{\left(\frac{K_a}{[H^+]+K_a}\right)}$$

The errors in the reported $f\,\mathrm{RS}^-$ values were calculated by propagating the uncertainty in the reported pK_a values and the experimental pH values, according to Eqn 5:

(5) $$\Delta f = \sqrt{\left(\frac{H}{(H+K_a)^2}\cdot \Delta K_a\right)^2 + \left(\frac{-K_a}{(H+K_a)^2}\cdot \Delta H\right)^2}$$

The errors in the reported k_2^{corr} values were calculated by propagating the uncertainty in the individual quadruplicate measurements (Eqn 6). This provided values that were slightly larger than the standard deviation of the four replicate measurements.

(6) $$\Delta k_2^{\text{corr}} = k_2^{\text{corr}} \sqrt{\left(\frac{\Delta k_2^{\text{calc}}}{k_2^{\text{calc}}}\right)^2 + \left(\frac{\Delta f}{f}\right)^2}$$

4.6.3 DFT Methods

All DFT calculations were performed using Gaussian 16 C.01[35]. The ωB97X-D exchange-correlation functional[36] was used in these calculations to address the issues related to delocalization error that occur in reactions involving thiolates[37,38]. The def2-TZVP basis set / core potential was used for all atoms. A CPCM continuum solvent model was used to describe the aqueous solvent[39]. The stability of the methanethiolate in a neutral aqueous solution was estimated using the experimental pK_a of 10.3 and the relation $\Delta G_{deprot} = RT \ln(10)\,(10.3 - 7)$.

Conflicts of interest

There are no conflicts to declare.

Acknowledgements

J.W.K. would like to thank the Natural Sciences and Engineering Research Council of Canada (NSERC) and the Canadian Institutes of Health Research (CIHR) for funding. C. N. R. also thanks the NSERC and the Digital Alliance of Canada for computer resources.

4.7 References

1 S. K. I. Watt, J. G. Charlebois, C. N. Rowley, J. W. Keillor, *Org Biomol Chem*, 2023, **21**, 4702-4710.

2 J. Singh, R. C. Petter, T. A. Baillie and A. Whitty, *Nat Rev Drug Discov*, 2011, **10**, 307–317.

3 M. C. Genovese, A. Spindler, A. Sagawa, W. Park, A. Dudek, A. Kivitz, J. Chao, L. S. M. Chan, J. Witcher, W. Barchuk and A. Nirula, *J Rheum*, 2021, **48**, 969–976.

4 J. Y. Byun, Y. T. Koh, S. Y. Jang, J. W. Witcher, J. R. Chan, A. Pustilnik, M. J. Daniels, Y. H. Kim, K. H. Suh, M. D. Linnik and Y. M. Lee, *Sci Rep*, 2021, **11**, 1–14.

5 P. H. Schafer, A. J. Kivitz, J. Ma, S. Korish, D. Sutherland, L. Li, A. Azaryan, J. Kosek, M. Adams, L. Capone, E. M. Hur, D. R. Hough and G. E. Ringheim, *Rheumatol Ther*, 2020, **7**, 101–119.

6 L. V. Sequist, Z. Piotrowska, M. J. Niederst, R. S. Heist, S. Digumarthy, A. T. Shaw and J. A. Engelman, *JAMA Oncol*, 2016, **2**, 541–543.

7 L. V. Sequist, J.-C. Soria, J. W. Goldman, H. A. Wakelee, S. M. Gadgeel, A. Varga, V. Papadimitrakopoulou, B. J. Solomon, G. R. Oxnard, R. Dziadziuszko, D. L. Aisner, R. C. Doebele, C. Galasso, E. B. Garon, R. S. Heist, J. Logan, J. W. Neal, M. A. Mendenhall, S. Nichols, Z. Piotrowska, A. J. Wozniak, M. Raponi, C. A. Karlovich, S. Jaw-Tsai, J. Isaacson, D. Despain, S. L. Matheny, L. Rolfe, A. R. Allen and D. R. Camidge, *N Engl J Med*, 2015, **372**, 1700–1709.

8 Y.-L. Wu, M. Tsuboi, J. He, T. John, C. Grohe, M. Majem, J. W. Goldman, K. Laktionov, S.-W. Kim, T. Kato, H.-V. Vu, S. Lu, K.-Y. Lee, C. Akewanlop, C.-J. Yu, F. de Marinis, L. Bonanno,

M. Domine, F. A. Shepherd, L. Zeng, R. Hodge, A. Atasoy, Y. Rukazenkov and R. S. Herbst, *N Engl J Med*, 2020, **383**, 1711–1723.

9 C. S. Tam, Y. C. Ou, J. Trotman and S. Opat, *Expert Rev Clin Pharmacol*, 2021, **14**, 1329–1344.

10 Y. Y. Syed, *Drugs*, 2020, **80**, 91–97.

11 J. C. Byrd, R. R. Furman, S. E. Coutre, I. W. Flinn, J. A. Burger, K. A. Blum, B. Grant, J. P. Sharman, M. Coleman, W. G. Wierda, J. A. Jones, W. Zhao, N. A. Heerema, A. J. Johnson, J. Sukbuntherng, B. Y. Chang, F. Clow, E. Hedrick, J. J. Buggy, D. F. James and S. O'Brien, *N Engl J Med*, 2013, **369**, 32–42.

12 J. A. Woyach, R. R. Furman, T.-M. Liu, H. G. Ozer, M. Zapatka, A. S. Ruppert, L. Xue, D. H.-H. Li, S. M. Steggerda, M. Versele, S. S. Dave, J. Zhang, A. S. Yilmaz, S. M. Jaglowski, K. A. Blum, A. Lozanski, G. Lozanski, D. F. James, J. C. Barrientos, P. Lichter, S. Stilgenbauer, J. J. Buggy, B. Y. Chang, A. J. Johnson and J. C. Byrd, *N Engl J Med*, 2014, **370**, 2286–2294.

13 F. Dickens, *Biochem J*, 1933, **27**, 1141–51.

14 J. Bi, S. Yang, L. Li, Q. Dai, N. Borcherding, B. A. Wagner, G. R. Buettner, D. R. Spitz, K. K. Leslie, J. Zhang and X. Meng, *Cell Death Dis*, 2019, **10**, 682-695.

15 N. Shindo and A. Ojida, *Bioorg Med Chem*, 2021, **47**, 116386.

16 R. D. Cole, W. H. Stein and S. Moore, *J Biol Chem*, 1958, **233**, 1359–1363.

17 D. G. Hoch, D. Abegg and A. Adibekian, *Chem Comm*, 2018, **54**, 4501–4512.

18 N. Shindo, H. Fuchida, M. Sato, K. Watari, T. Shibata, K. Kuwata, C. Miura, K. Okamoto, Y. Hatsuyama, K. Tokunaga, S. Sakamoto, S. Morimoto, Y. Abe, M. Shiroishi, J. M. M. Caaveiro,

T. Ueda, T. Tamura, N. Matsunaga, T. Nakao, S. Koyanagi, S. Ohdo, Y. Yamaguchi, I. Hamachi, M. Ono and A. Ojida, *Nat Chem Biol*, 2019, **15**, 250–258.

19 L. Mader, S. K. I. Watt, H. R. Iyer, L. Nguyen, H. Kaur and J. W. Keillor, *RSC Med Chem*, 2023, **14**, 277-298.

20 L. A. Bateman, T. B. Nguyen, A. M. Roberts, D. K. Miyamoto, W. M. Ku, T. R. Huffman, Y. Petri, M. J. Heslin, C. M. Contreras, C. F. Skibola, J. A. Olzmann and D. K. Nomura, *Chem Comm*, 2017, **53**, 7234–7237.

21 E. A. Grossman, C. C. Ward, J. N. Spradlin, L. A. Bateman, T. R. Huffman, D. K. Miyamoto, J. I. Kleinman and D. K. Nomura, *Cell Chem Biol*, 2017, **24**, 1368–1376.

22 K. N. Padhariya, M. Athavale, S. Srivastava and P. S. Kharkar, *Drug Dev Res*, 2020, **81**, 356–365.

23 M. Sato, H. Fuchida, N. Shindo, K. Kuwata, K. Tokunaga, G. Xiao-Lin, R. Inamori, K. Hosokawa, K. Watari, T. Shibata, N. Matsunaga, S. Koyanagi, S. Ohdo, M. Ono and A. Ojida, *ACS Med Chem Lett*, 2020, **11**, 1137–1144.

24 S. K. I. Watt, J. G. Charlebois, C. N. Rowley and J. W. Keillor, *Org Biomol Chem*, 2022, **20**, 8898–8906.

25 S. K. I. Watt, J. G. Charlebois, C. N. Rowley and J. W. Keillor, *Org Biomol Chem*, 2023, **21**, 2204–2212.

26 V. J. Cee, L. P. Volak, Y. Chen, M. D. Bartberger, C. Tegley, T. Arvedson, J. McCarter, A. S. Tasker and C. Fotsch, *J Med Chem*, 2015, **58**, 9171–9178.

27 V. Franzen, *Chem Ber*, 1957, **90**, 623–633.

28 A. K. Mitra and M. M. Narurkar, *Int J Pharm*, 1986, **28**, 119–124.

29 J. P. Danehy and K. N. Parameswaran, *J Chem Eng Data*, 1968, **13**, 386–389.

30 R. A. Bednar, *Biochem*, 1990, **29**, 3684–3690.

31 M. A. R. Raycroft, K. Racine, C. N. Rowley and J. W. Keillor, *J Org Chem*, 2018, **83**, 11674–11685.

32 J. W. Ogilvie, J. T. Tildon and B. S. Strauch, *Biochem*, 1964, **3**, 754–758.

33 M. E. Flanagan, J. A. Abramite, D. P. Anderson, A. Aulabaugh, U. P. Dahal, A. M. Gilbert, C. Li, J. Montgomery, S. R. Oppenheimer, T. Ryder, B. P. Schuff, D. P. Uccello, G. S. Walker, Y. Wu, M. F. Brown, J. M. Chen, M. M. Hayward, M. C. Noe, R. S. Obach, L. Philippe, V. Shanmugasundaram, M. J. Shapiro, J. Starr, J. Stroh and Y. Che, *J Med Chem*, 2014, **57**, 10072–10079.

34 E. Engelage, N. Schulz, F. Heinen, S. M. Huber, D. G. Truhlar and C. J. Cramer, *Chem Eur J*, 2018, **24**, 15983–15987.

35 M. J. Frisch, G. W. Trucks, H. B. Schlegel, G. E. Scuseria, M. A. Robb, J. R. Cheeseman, G. Scalmani, V. Barone, G. A. Petersson, H. Nakatsuji, X. Li, M. Caricato, A. V. Marenich, J. Bloino, B. G. Janesko, R. Gomperts, B. Mennucci, H. P. Hratchian, J. V. Ortiz, A. F. Izmaylov, J. L. Sonnenberg, Williams, F. Ding, F. Lipparini, F. Egidi, J. Goings, B. Peng, A. Petrone, T. Henderson, D. Ranasinghe, V. G. Zakrzewski, J. Gao, N. Rega, G. Zheng, W. Liang, M. Hada, M. Ehara, K. Toyota, R. Fukuda, J. Hasegawa, M. Ishida, T. Nakajima, Y. Honda, O. Kitao, H. Nakai, T. Vreven, K. Throssell, J. A. Montgomery Jr., J. E. Peralta, F. Ogliaro, M. J. Bearpark, J. J. Heyd, E. N. Brothers, K. N. Kudin, V. N. Staroverov, T. A. Keith, R. Kobayashi, J. Normand,

K. Raghavachari, A. P. Rendell, J. C. Burant, S. S. Iyengar, J. Tomasi, M. Cossi, J. M. Millam, M. Klene, C. Adamo, R. Cammi, J. W. Ochterski, R. L. Martin, K. Morokuma, O. Farkas, J. B. Foresman and D. J. Fox, Gaussian, Inc., Wallingford CT, 2016.

36 J. Da Chai and M. Head-Gordon, *Phys Chem Chem Phys*, 2008, **10**, 6615–6620.

37 J. M. Smith, Y. Jami Alahmadi and C. N. Rowley, *J Chem Theory Comput*, 2013, **9**, 4860–4865.

38 E. Awoonor-Williams, W. C. Isley, S. G. Dale, E. R. Johnson, H. Yu, A. D. Becke, B. Roux and C. N. Rowley, *J Comput Chem*, 2020, **41**, 427–438.

39 V. Barone and M. Cossi, *J Phys Chem A*, 1998, **102**, 1995–2001.

Chapter 5 : Final conclusions and future perspectives

5.1 Final conclusions

The three manuscripts contained herein offer a detailed view into the intrinsic reactivities of *N*-phenyl and *N*-alkyl acrylamides, and *N*-phenyl chloroacetamide. The first two manuscripts offer a detailed examination of the proposed mechanism of thiol-addition to the acrylamide series, where all data support the microscopic reverse of an $E1_{cb}$ elimination.

The third manuscript initiates an in-depth investigation into the chloroacetamide series. The mechanism of thiol-addition to chloroacetamides is intuitively understood to undergo an S_N2 type addition; however, no studies had previously been done to confirm this hypothesis. Therefore, the S_N2 pathway was the sole mechanism proposed in the manuscript and is proven consistent with the experimental data collected over the course of the study. The differences between the chloroacetamide and acrylamide derivatives are highlighted along with an initial exploration of the haloacetamide leaving group effect at the α- position.

Throughout this systematic study of some of the most commonly used electrophilic warheads in TCI development, many important discoveries were made concerning each individual warhead derivative. Additionally, the investigations were carried out in a way designed to allow for intra-study comparison. From the individually drawn conclusions, all warhead derivatives included in these studies are relatively insensitive to thiolate nucleophilicity. Thus, lacking the ability to clearly distinguish between different ionised thiolates. For the purpose of TCI development, this directs importance to the rest of the molecular scaffold – to initiate reversible binding within the desired active site, and properly aligning the inhibitor's warhead with the desired Cys target prior to irreversible covalent bond formation.

However, while the insensitivity towards thiolate nucleophilicity remained a constant trend, their intrinsic reactivity was vastly varied. *N*-phenylchloroacetamide was found to have the greatest intrinsic reactivity, followed by *N*-phenylacrylamide, *N*-acryloylpiperidine, and lastly *N*-propylacrylamide, each reacting several-fold faster than the next. This is an important consideration for the *in vivo* functionality of an inhibitor, as high reactivity combined with weak selectivity leads to instability. Unsurprisingly, the greatest downfall of chloroacetamide warheads has been their biostability issues, highlighting the importance of achieving a balance between stability and reactivity. In this way, electrophilic warheads with attenuated reactivity such as the *N*- alkyl and *N,N*- dialkyl acrylamides may better lend themselves as tools in the development of new enzyme inhibitors.

5.2 Future perspectives

This project has many potential future directions. In direct continuation of this project, it would be interesting to study the effect of alkyl spacers between the acrylamide moiety and an aromatic group. As well, studying the *N*- alkyl chloroacetamide derivatives in comparison with their acrylamide counterparts would be informative, in addition to venturing outside of acrylamides and haloacetamides to probe the intrinsic reactivity and mechanistic properties of other electrophilic warheads used in the design of irreversible enzyme inhibitors.

Another avenue of interest would be to use this kinetic method to monitor the intrinsic reactivity of small molecule inhibitors and compare those experimental values to data collected through enzymatic assays, as highlighted in our recent publication.[1]

5.3 References

1 L. Mader, S. K. I. Watt, H. R. Iyer, L. Nguyen, H. Kaur and J. W. Keillor, *RSC Med Chem*, 2023, **14**, 277-298.

S2. APPENDIX I: Supplementary information for Chapter 2

Table S2.1. pH of buffer, mobile phase gradient, length of run and retention times of NPA and thiol-adduct for each experiment of NPA with RSH (**1a-e**).

Thiol	pH of Aqueous Buffer	Mobile Phase Gradient (% CH_3CN in H_2O)	Total Length of Run (min)	Retention Time NPA (min)	Retention Time Adduct (min)
1a	7.4	20-80	15	7.9	5.7
1b	7.4	20-80	15	7.6	3.3
1c	7.4	20-80	15	7.9	3.4
1d	9.0	20-80	15	7.6	6.4
1e	9.0	20-50	20	8.7	9.9

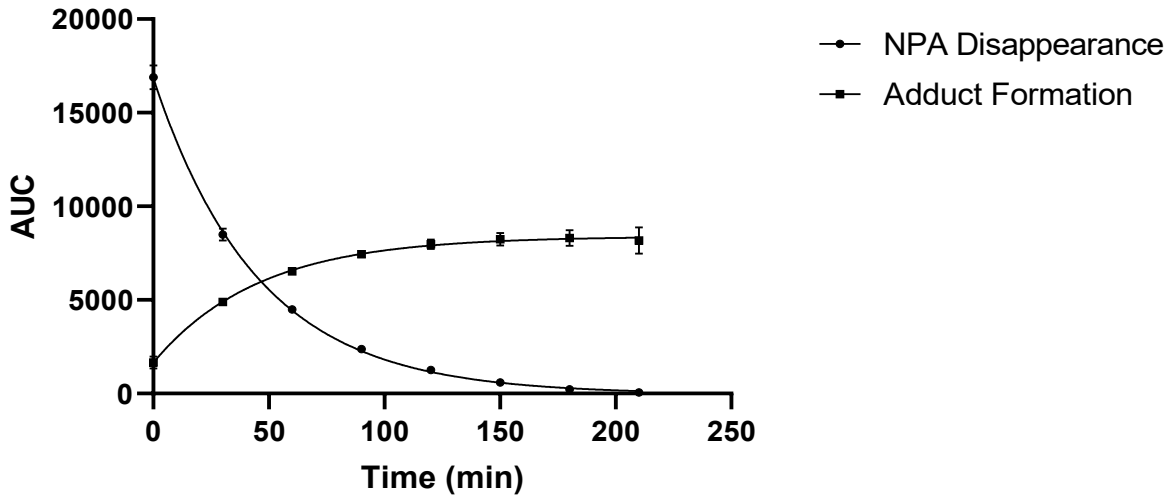

Figure S2.1. Plot of disappearance of NPA (1mM) and formation of adduct for the addition of DEC (10 mM) vs time (min) in 67 mM potassium phosphate buffer (1% v/v DMSO), pH 7.4, μ = 0.100, T = 22°C. The area under the curve (AUC) was integrated from the chromatograph at 214 nm for the peaks corresponding to NPA and the adduct. The AUC data for disappearance of NPA were fitted to a mono-exponential decay with the constraint that the plateau = 0 and the data for formation of adduct were fitted to a mono-exponential association to afford the k_{obs} values summarized in **Table S2.2**.

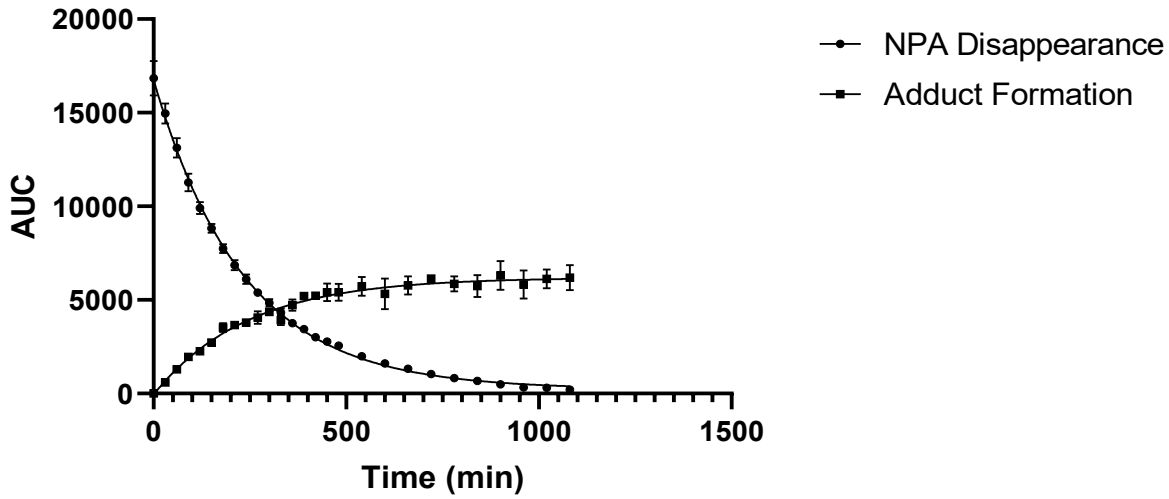

Figure S2.2. Plot of disappearance of NPA (1 mM) and formation of adduct for the addition of Cys (10 mM) vs time (min) in 67 mM potassium phosphate buffer (1% v/v DMSO), pH 7.4, μ = 0.100, T = 22°C. The area under the curve (AUC) was integrated from the chromatograph at 214 nm for the peaks corresponding to NPA and the adduct. The AUC data for disappearance of NPA were fitted to a mono-exponential decay with the constraint that the plateau = 0 and the data for formation of adduct were fitted to a mono-exponential association with the constraint that $Y_0 = 0$ to afford the k_{obs} values summarized in **Table S2.2**.

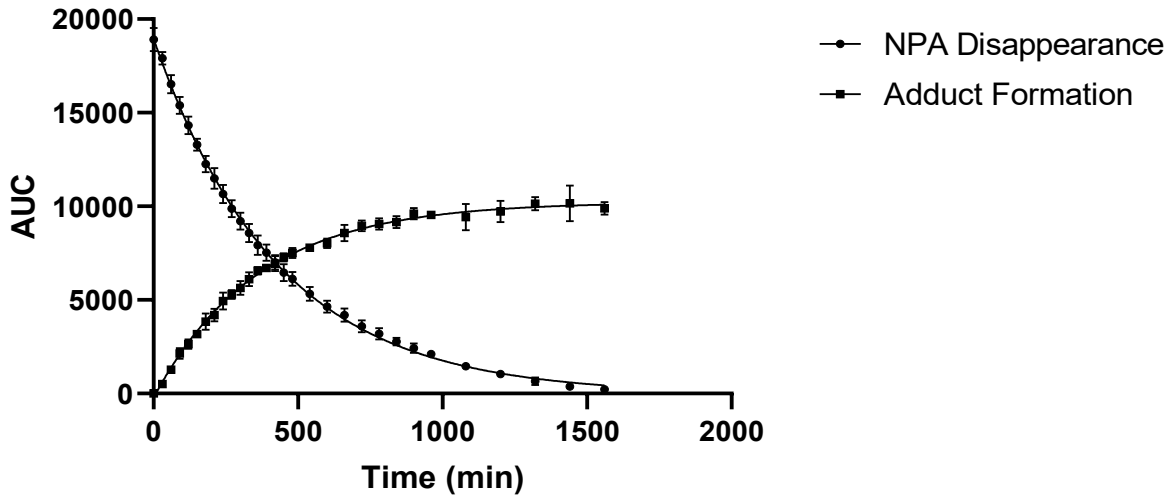

Figure S2.3. Plot of disappearance of NPA (1 mM) and formation of adduct for the addition of GSH (10 mM) vs time (min) in 67 mM potassium phosphate buffer (1% v/v DMSO), pH 7.4, μ = 0.100, T = 22°C. The area under the curve (AUC) was integrated from the chromatograph at 214 nm for the peaks corresponding to NPA and the adduct. The AUC data for disappearance of NPA were fitted to a mono-exponential decay with the constraint that the plateau = 0 and the data for formation of adduct were fitted to a mono-exponential association with the constraint that $Y_0 = 0$ to afford the k_{obs} values summarized in **Table S2.2**.

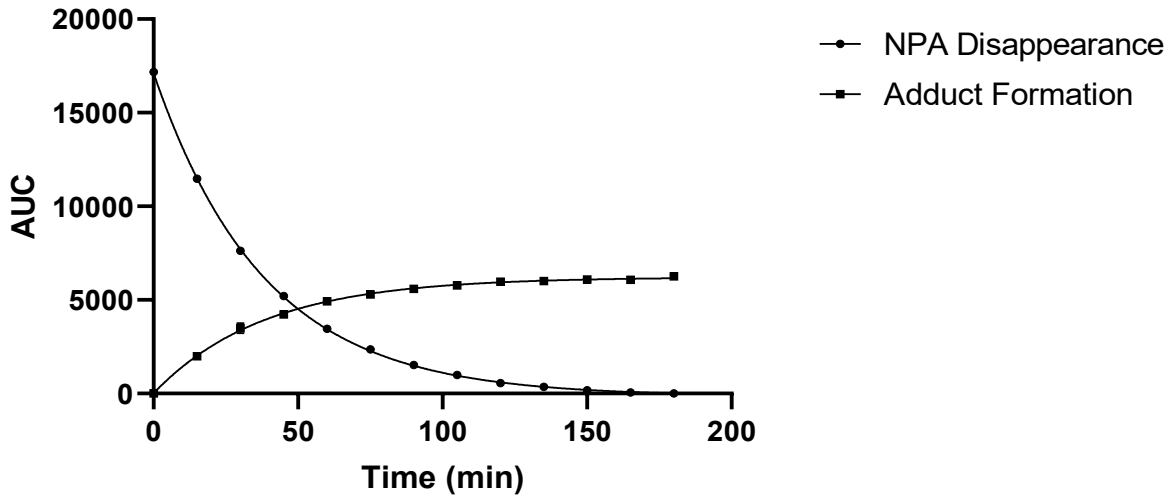

Figure S2.4. Plot of disappearance of NPA (1 mM) and formation of adduct for the addition of BME (10 mM) vs time (min) in 67 mM CHES buffer (1% v/v DMSO), pH 9, $\mu = 0.100$, T = 22°C. The area under the curve (AUC) was integrated from the chromatograph at 214 nm for the peaks corresponding to NPA and the adduct. The AUC data for disappearance of NPA were fitted to a mono-exponential decay with the constraint that the plateau = 0 and the data for formation of adduct were fitted to a mono-exponential association with the constraint that $Y_0 = 0$ to afford the k_{obs} values summarized in **Table S2.2**.

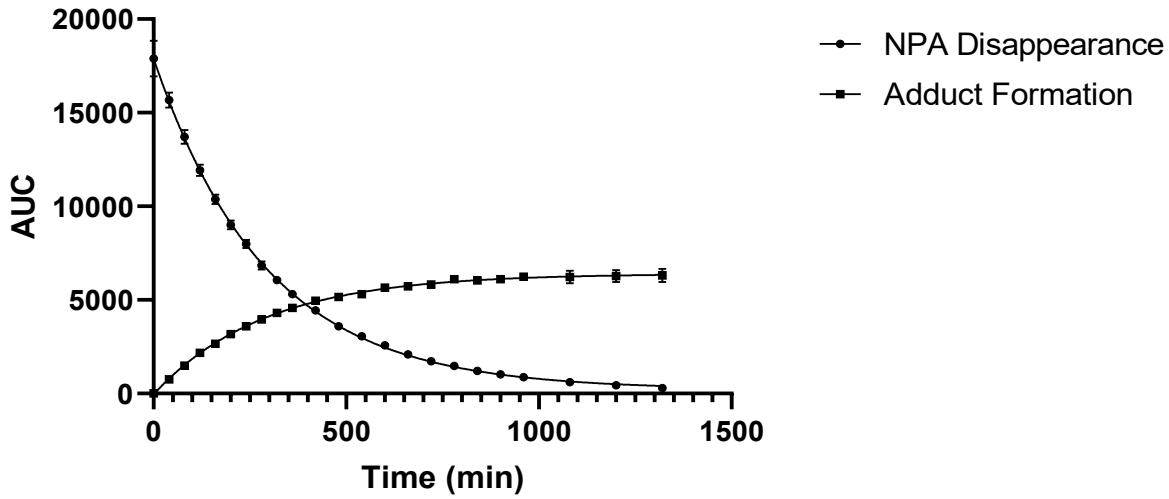

Figure S2.5. Plot of disappearance of NPA (1 mM) and formation of adduct for the addition of MPA (10 mM) vs time (min) in 67 mM CHES buffer (1% v/v DMSO), pH 9, $\mu = 0.100$, T = 22°C. The area under the curve (AUC) was integrated from the chromatograph at 214 nm for the peaks corresponding to NPA and the adduct. The AUC data for disappearance of NPA were fitted to a mono-exponential decay with the constraint that the plateau = 0 and the data for formation of adduct were fitted to a mono-exponential association with the constraint that $Y_0 = 0$ to afford the k_{obs} values summarized in **Table S2.2**.

Table S2.2. Observed rate constants (k_{obs}), calculated second order rate constants (k_2^{calc}), and corrected second order rate constants (k_2^{corr}) for the addition of RSH (**1a-e**) to NPA. Measurements were made in duplicate for both the disappearance of acrylamide and appearance of adduct, unless otherwise indicated. Errors represent the standard deviation of the replicate values.

Thiol	**k_{obs} (s^{-1})**	**k_2^{calc} ($M^{-1}s^{-1}$)**	**k_2^{corr} ($M^{-1}s^{-1}$)**	**log(k_2^{corr})**
1a	0.37 ± 0.03[a]	0.037 ± 0.003	0.13 ± 0.01	-0.887 ± 0.036
1b	0.068 ± 0.007	0.0068 ± 0.0007	0.061 ± 0.006	-1.214 ± 0.043
1c	0.041 ± 0.002[b]	0.0041 ± 0.0002	0.086 ± 0.005	-1.064 ± 0.024
1d	0.44 ± 0.02	0.044 ± 0.002	0.220 ± 0.008	-0.657 ± 0.016
1e	0.056 ± 0.002	0.0056 ± 0.0002	0.118 ± 0.004	-0.929 ± 0.013

[a]*Measurements made in triplicate.* [b]*Measurements made in quadruplet.*

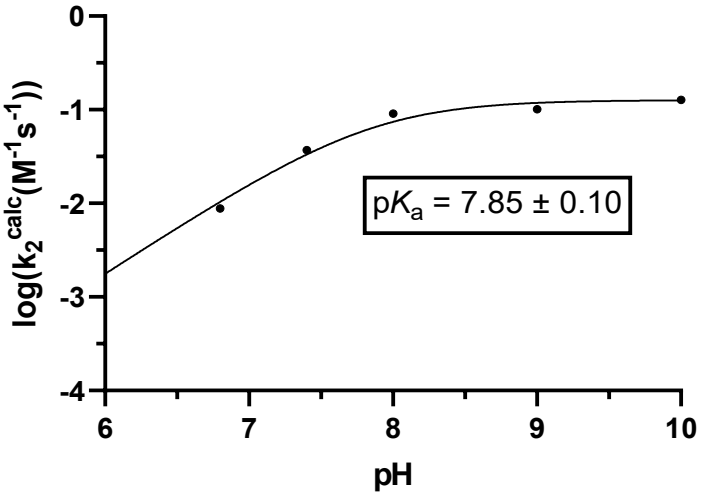

Figure S2.6. Plot of log (k_2^{calc}) vs pH for the addition of 1a to NPA in aqueous buffer (1% v/v DMSO), μ = 0.100, T = 22°C. The data were fitted to the **eq 1**, giving a kinetic pK_a value of 7.85 ± 0.10.

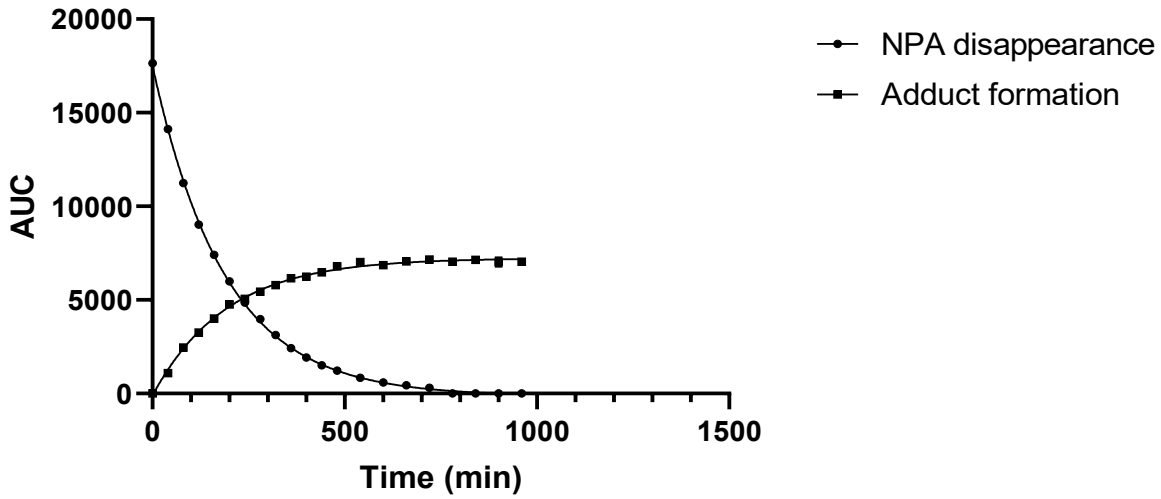

Figure S2.7. Plot of disappearance of NPA (1 mM) and formation of adduct for the addition of 1a (10 mM) vs time (min) in 67 mM MOPS buffer (1% v/v DMSO) at pH 6.8, μ = 0.100, T = 22°C. The area under the curve (AUC) was integrated from the chromatograph at 214 nm for the peaks corresponding to NPA and the adduct. The AUC data for disappearance of NPA were fitted to a mono-exponential decay with the constraint that the plateau = 0 and the data for formation of adduct were fitted to a mono-exponential association with the constraint that $Y_0 = 0$ to afford the k_{obs} values summarized in **Table S2.3**.

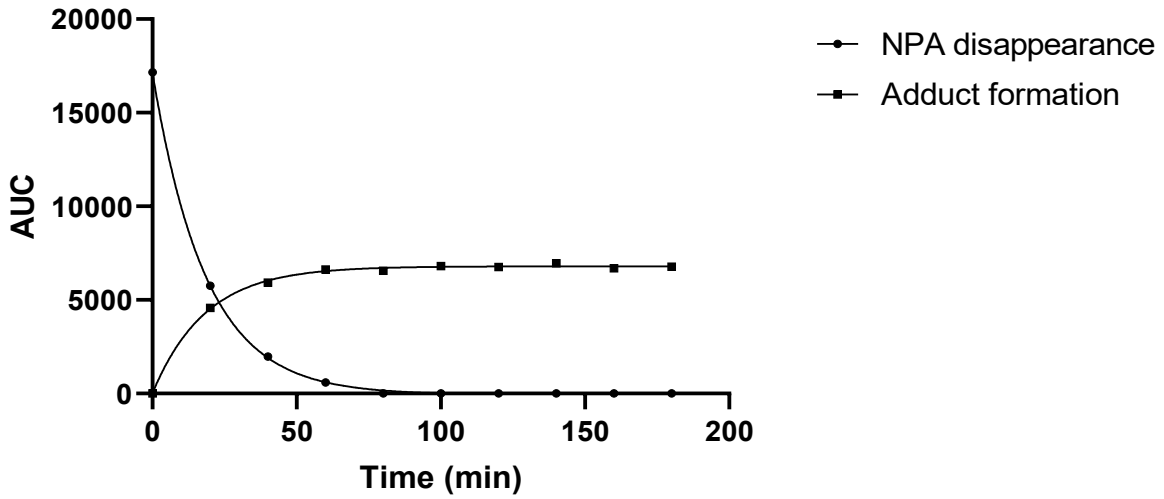

Figure S2.8. Plot of disappearance of NPA (1 mM) and formation of adduct for the addition of 1a (10 mM) vs time (min) in 67 mM TRIS buffer (1% v/v DMSO) at pH 8.0, μ = 0.100, T = 22°C. The area under the curve (AUC) was integrated from the chromatograph at 214 nm for the peaks corresponding to NPA and the adduct. The AUC data for disappearance of NPA were fitted to a mono-exponential decay with the constraint that the plateau = 0 and the data for formation of adduct were fitted to a mono-exponential association with the constraint that $Y_0 = 0$ to afford the k_{obs} values summarized in **Table S2.3.**

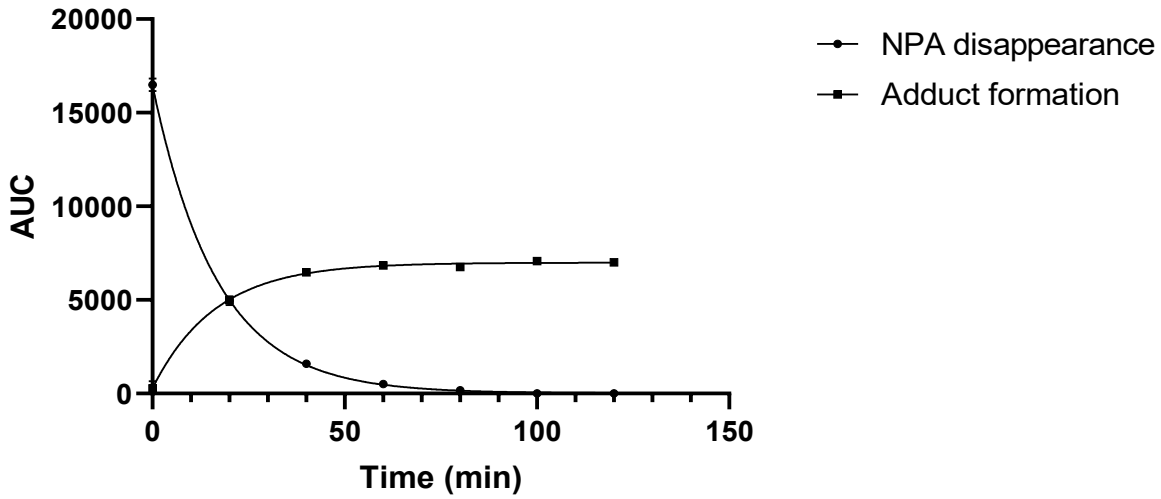

Figure S2.9. Plot of disappearance of NPA (1 mM) and formation of adduct for the addition of 1a (10 mM) vs time (min) in 67 mM CHES buffer (1% v/v DMSO) at pH 9.0, μ = 0.100, T = 22°C. The area under the curve (AUC) was integrated from the chromatograph at 214 nm for the peaks corresponding to NPA and the adduct. The AUC data for disappearance of NPA were fitted to a mono-exponential decay with the constraint that the plateau = 0 and the data for formation of adduct were fitted to a mono-exponential association with the constraint that $Y_0 = 0$ to afford the k_{obs} values summarized in **Table S2.3**.

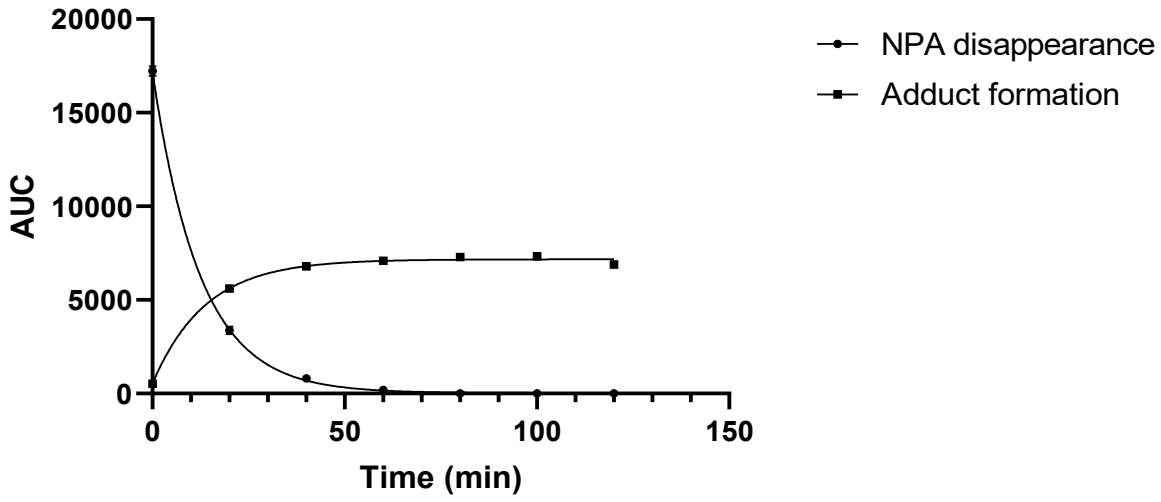

Figure S2.10. Plot of disappearance of NPA (1 mM) and formation of adduct for the addition of 1a (10 mM) vs time (min) in 67 mM CAPS buffer (1% v/v DMSO) at pH 10.0, μ = 0.100, T = 22°C. The area under the curve (AUC) was integrated from the chromatograph at 214 nm for the peaks corresponding to NPA and the adduct. The AUC data for disappearance of NPA were fitted to a mono-exponential decay with the constraint that the plateau = 0 and the data for formation of adduct were fitted to a mono-exponential association with the constraint that $Y_0 = 0$ to afford the k_{obs} values summarized in **Table S2.3**.

Table S2.3. Observed rate constants (k_{obs}) and calculated second order rate constants (k_2^{calc}) for the addition of RSH (1a) to NPA at variable pH. Measurements were made in duplicate for both the disappearance of acrylamide and appearance of adduct. Errors represent the standard deviation of the replicate values.

pH	**k_{obs} (s^{-1})**	**k_2^{calc} ($M^{-1}s^{-1}$)**	**$\log(k_2^{calc})$**
6.8	0.088 ± 0.004	0.0088 ± 0.0004	-2.056 ± 0.020
7.4	0.369 ± 0.032	0.0369 ± 0.0032	-1.433 ± 0.036
8.0	0.908 ± 0.033	0.0908 ± 0.0033	-1.042 ± 0.016
9.0	1.010 ± 0.044	0.1010 ± 0.0044	-0.996 ± 0.019
10.0	1.280 ± 0.085	0.1280 ± 0.0085	-0.894 ± 0.029

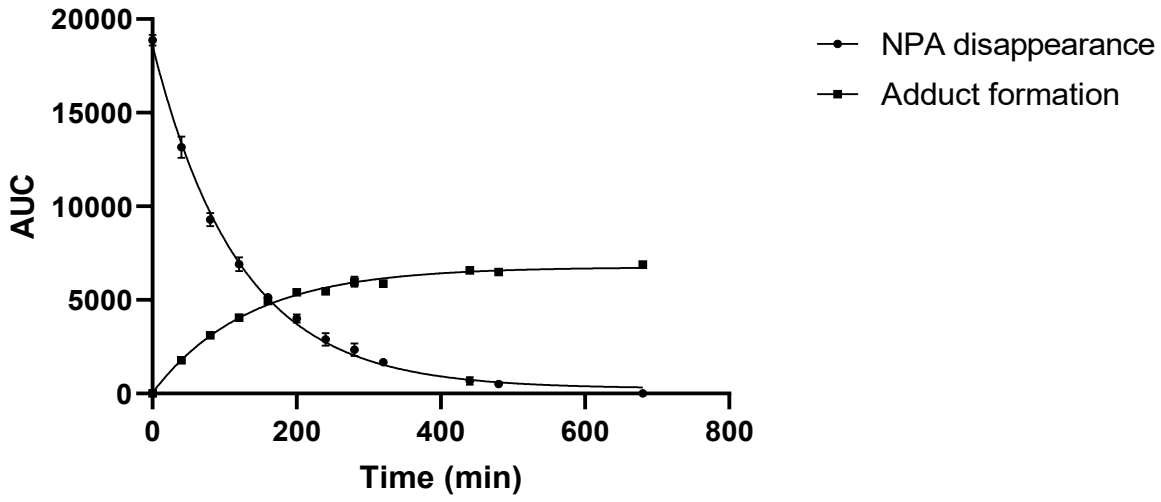

Figure S2.11. Plot of disappearance of NPA (1 mM) and formation of adduct for the addition of 1e (10 mM) vs time (min) in 67 mM CHES buffer (1% v/v DMSO) at pH 9.0, $\mu = 0.100$, T = 37°C. The area under the curve (AUC) was integrated from the chromatograph at 214 nm for the peaks corresponding to NPA and the adduct. The AUC data for disappearance of NPA were fitted to a mono-exponential decay with the constraint that the plateau = 0 and the data for formation of adduct were fitted to a mono-exponential association with the constraint that $Y_0 = 0$ to afford the k_{obs} values summarized in **Table S2.4**.

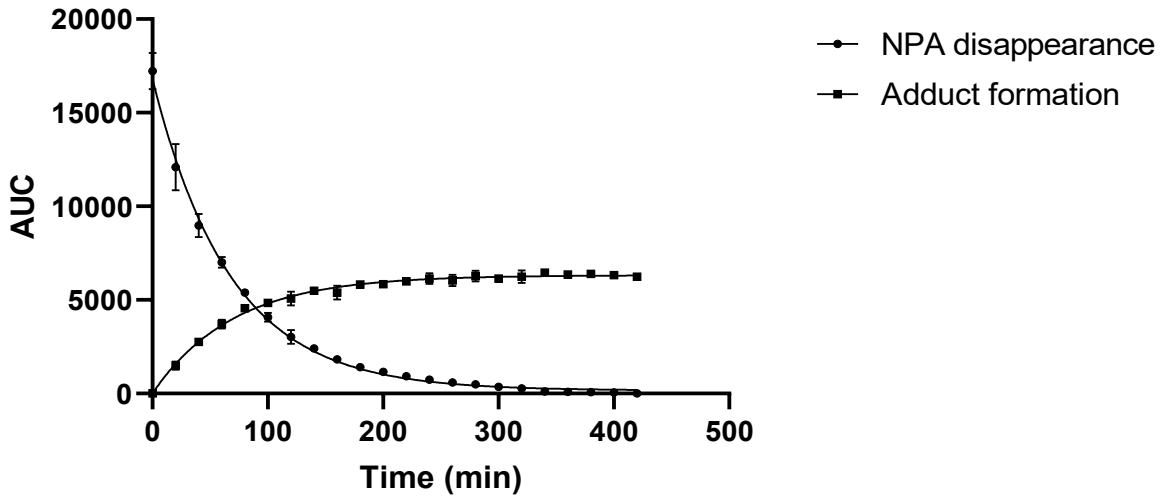

Figure S2.12. Plot of disappearance of NPA (1 mM) and formation of adduct for the addition of 1e (10 mM) vs time (min) in 67 mM CHES buffer (1% v/v DMSO) at pH 9.0, $\mu = 0.100$, T = 53°C. The area under the curve (AUC) was integrated from the chromatograph at 214 nm for the peaks corresponding to NPA and the adduct. The AUC data for disappearance of NPA were fitted to a mono-exponential decay with the constraint that the plateau = 0 and the data for formation of adduct were fitted to a mono-exponential association with the constraint that $Y_0 = 0$ to afford the k_{obs} values summarized in **Table S2.4**.

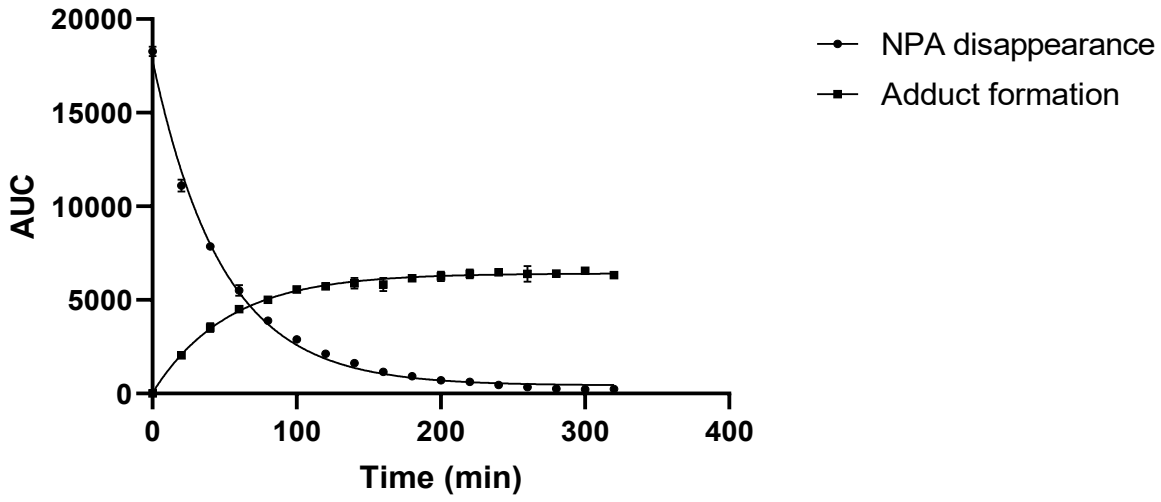

Figure S2.13. Plot of disappearance of NPA (1 mM) and formation of adduct for the addition of 1e (10 mM) vs time (min) in 67 mM CHES buffer (1% v/v DMSO) at pH 9.0, $\mu = 0.100$, T = 62°C. The area under the curve (AUC) was integrated from the chromatograph at 214 nm for the peaks corresponding to NPA and the adduct. The AUC data for disappearance of NPA were fitted to a mono-exponential decay with the constraint that the plateau = 0 and the data for formation of adduct were fitted to a mono-exponential association with the constraint that $Y_0 = 0$ to afford the k_{obs} values summarized in **Table S2.4**.

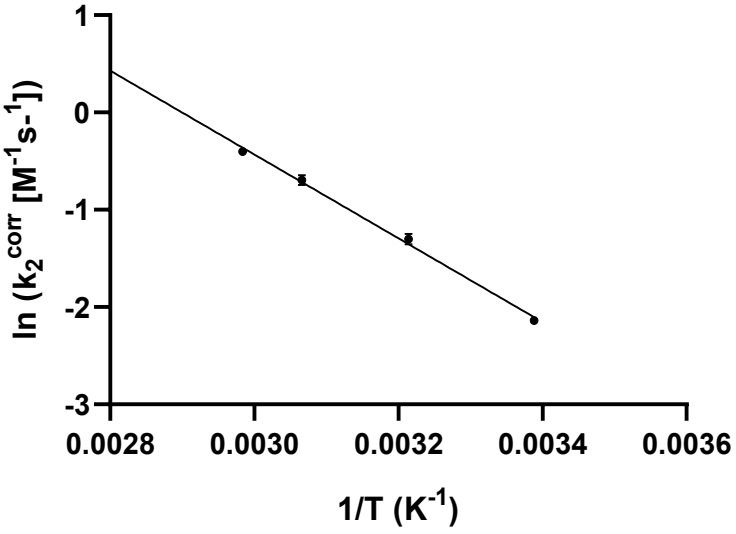

Figure S2.14. Arrhenius plot showing ln(k_2^{corr}) vs 1/T for the addition of 1e to NPA in 67 mM CHES buffer (1% v/v DMSO), pH = 9.0, μ = 0.100. The data were fitted to a linear regression to obtain a slope of -4308 ± 173.3 and y-intercept of 12.49 ± 0.55.

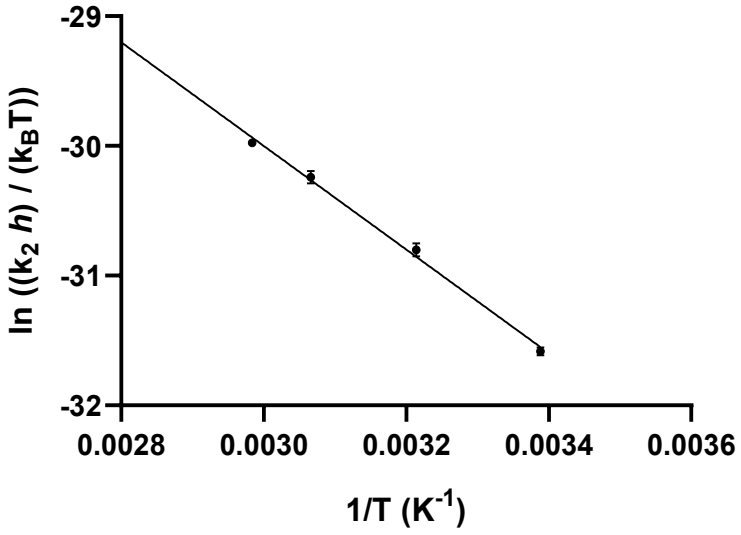

Figure S2.15. Eyring plot showing ln((k_2h)/(k_BT)) vs 1/T for the addition of 1e to NPA in 67 mM CHES buffer (1% v/v DMSO), pH = 9.0, μ = 0.100. The data were fitted to a linear regression to obtain a slope of -3994 ± 177.2 and y-intercept of -18.02 ± 0.56.

Table S2.4. Observed rate constants (k_{obs}), calculated second order rate constants (k_2^{calc}), and corrected second order rate constants (k_2^{corr}) for the addition of MPA (**1e**) to NPA at variable temperatures. Measurements were made in duplicate for both the disappearance of acrylamide and appearance of adduct. Errors represent the standard deviation of the replicate values.

Temp (°C)	**k_{obs} (s^{-1})**	**k_2^{calc} ($M^{-1}s^{-1}$)**	**k_2^{corr} ($M^{-1}s^{-1}$)**	**$\ln(k_2^{corr})$**	**$\ln((k_2^{corr}h)/k_BT)$**
22	0.056 ± 0.002	0.0056 ± 0.0002	0.118 ± 0.004	-2.137 ± 0.029	-31.584 ± 0.031
38	0.130 ± 0.007	0.013 ± 0.0007	0.272 ± 0.015	-1.302 ± 0.053	-30.802 ± 0.050
52	0.238 ± 0.012	0.024 ± 0.001	0.499 ± 0.025	-0.695 ± 0.050	-30.242 ± 0.050
63	0.320 ± 0.007	0.032 ± 0.0006	0.670 ± 0.014	-0.401 ± 0.021	-29.975 ± 0.021

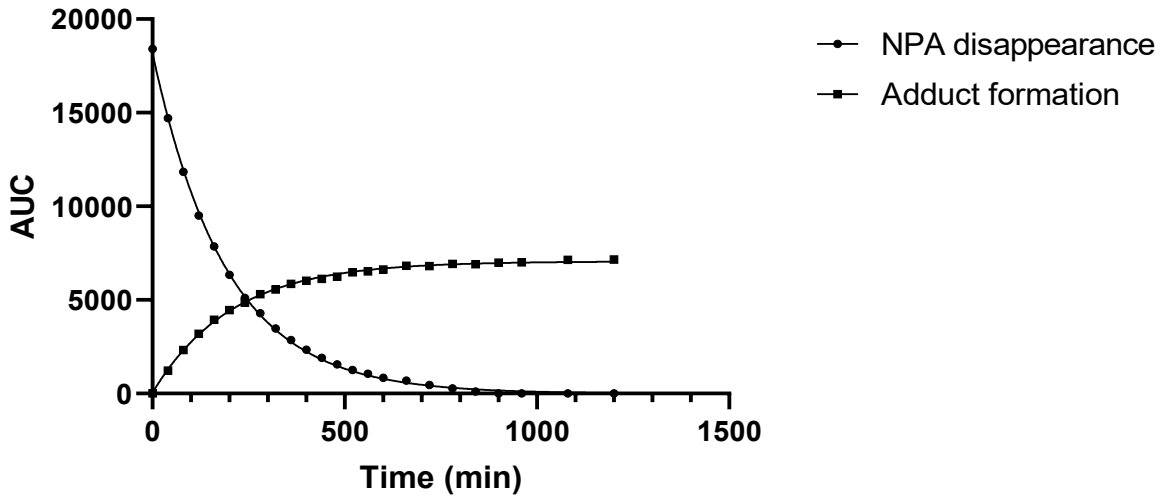

Figure S2.16. Plot of disappearance of NPA (1 mM) and formation of adduct for the addition of 1e (10 mM) vs time (min) in 67 mM CHES buffer (1% v/v DMSO), pH 9.0, $\mu = 0.050$, T = 22°C. The area under the curve (AUC) was integrated from the chromatograph at 214 nm for the peaks corresponding to NPA and the adduct. The AUC data for disappearance of NPA were fitted to a mono-exponential decay with the constraint that the plateau = 0 and the data for formation of adduct were fitted to a mono-exponential association with the constraint that $Y_0 = 0$ to afford the k_{obs} values summarized in **Table S2.5**.

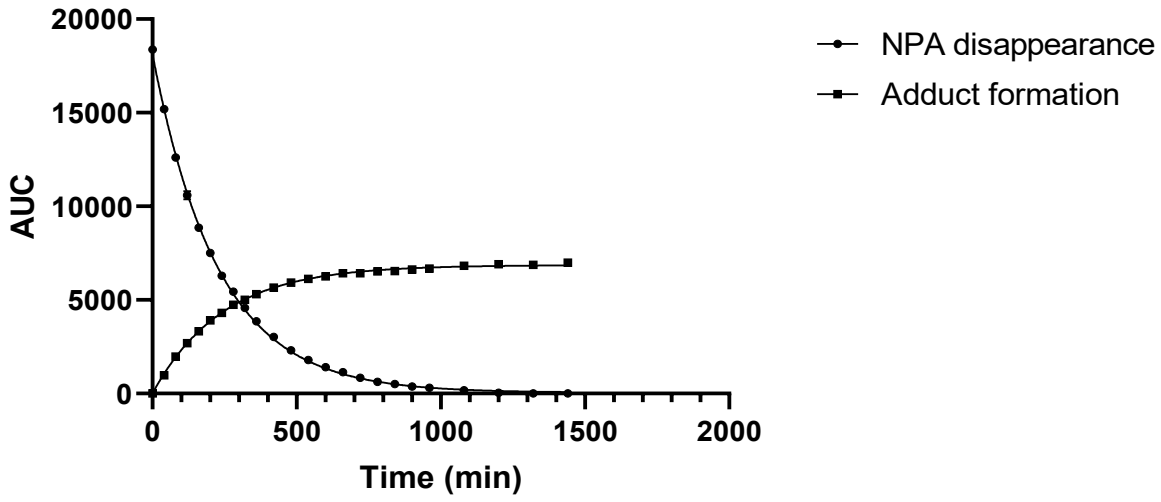

Figure S 2.17. Plot of disappearance of NPA (1 mM) and formation of adduct for the addition of 1e (10 mM) vs time (min) in 67 mM CHES buffer (1% v/v DMSO), pH 9.0, μ = 0.075, T = 22°C. The area under the curve (AUC) was integrated from the chromatograph at 214 nm for the peaks corresponding to NPA and the adduct. The AUC data for disappearance of NPA were fitted to a mono-exponential decay with the constraint that the plateau = 0 and the data for formation of adduct were fitted to a mono-exponential association with the constraint that $Y_0 = 0$ to afford the k_{obs} values summarized in **Table S2.5**.

Table S2.5. Observed rate constants (k_{obs}), calculated second order rate constants (k_2^{calc}), and corrected second order rate constants (k_2^{corr}) for the addition of MPA (**1e**) to NPA at varying ionic strengths. Measurements were made in duplicate for both the disappearance of acrylamide and appearance of adduct. Errors represent the standard deviation of the replicate values.

[KCl] (M)	k_{obs} (s^{-1})	k_2^{calc} ($M^{-1}s^{-1}$)	k_2^{corr} ($M^{-1}s^{-1}$)
0.050	0.0845 ± 0.0032	0.00845 ± 0.00032	0.177 ± 0.007
0.075	0.0707 ± 0.0024	0.00707 ± 0.00024	0.148 ± 0.005
0.100	0.0562 ± 0.0017	0.00562 ± 0.00017	0.118 ± 0.004

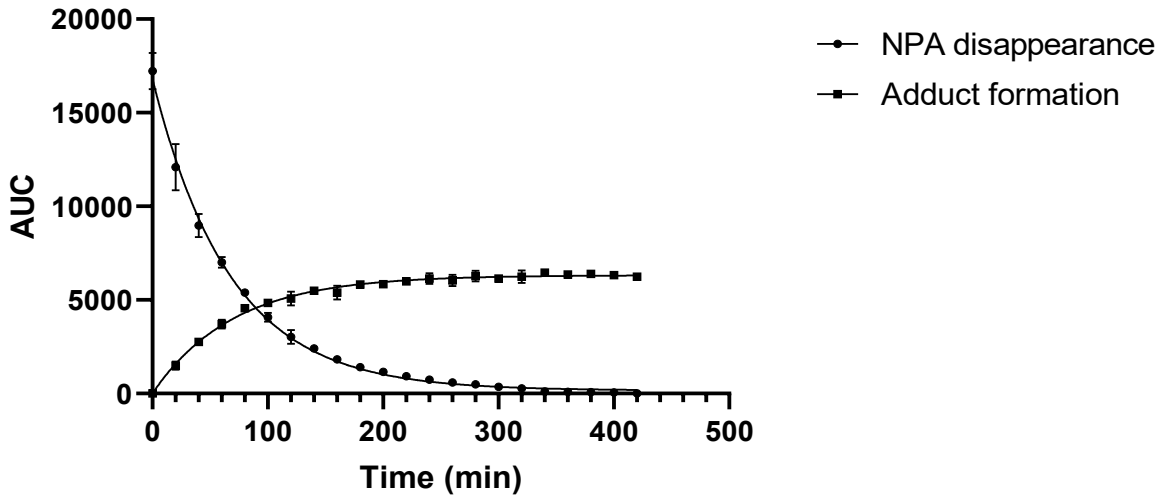

Figure S2.18. Plot of disappearance of NPA (1 mM) and formation of adduct for the addition of 1e (10 mM) vs time (min) in carbonate buffer prepared in D_2O (1% v/v ACN), pD = 9.7, μ = 0.100, T = 22°C. The area under the curve (AUC) was integrated from the chromatograph at 214 nm fort eh peaks corresponding to NPA and the adduct. The AUC data for disappearance of NPA were fitted to a mono-exponential decay with the constraint that the plateau = 0 and the data for formation of adduct were fitted to a mono-exponential association with the constraint that $Y_0 = 0$ to afford the k_{obs} values summarized in **Table S2.6**.

Table S2.6. Observed rate constants (k_{obs}), calculated second order rate constants (k_2^{calc}), corrected second order rate constants (k_2^{corr}), and calculated solvent kinetic isotope effect ratio for the addition of MPA (**1e**) to NPA. Measurements were made in duplicate for both the disappearance of acrylamide and appearance of adduct. Errors represent the standard deviation of the replicate values.

L_2O	k_{obs} (s^{-1})	k_2^{calc} ($M^{-1}s^{-1}$)	k_2^{corr} ($M^{-1}s^{-1}$)	$k_2^{corr,H2O}/k_2^{corr,D2O}$
H	0.0562 ± 0.0017	0.00562 ± 0.00017	0.118 ± 0.004	1.09 ± 0.04
D	0.103 ± 0.003	0.0103 ± 0.0003	0.108 ± 0.003	

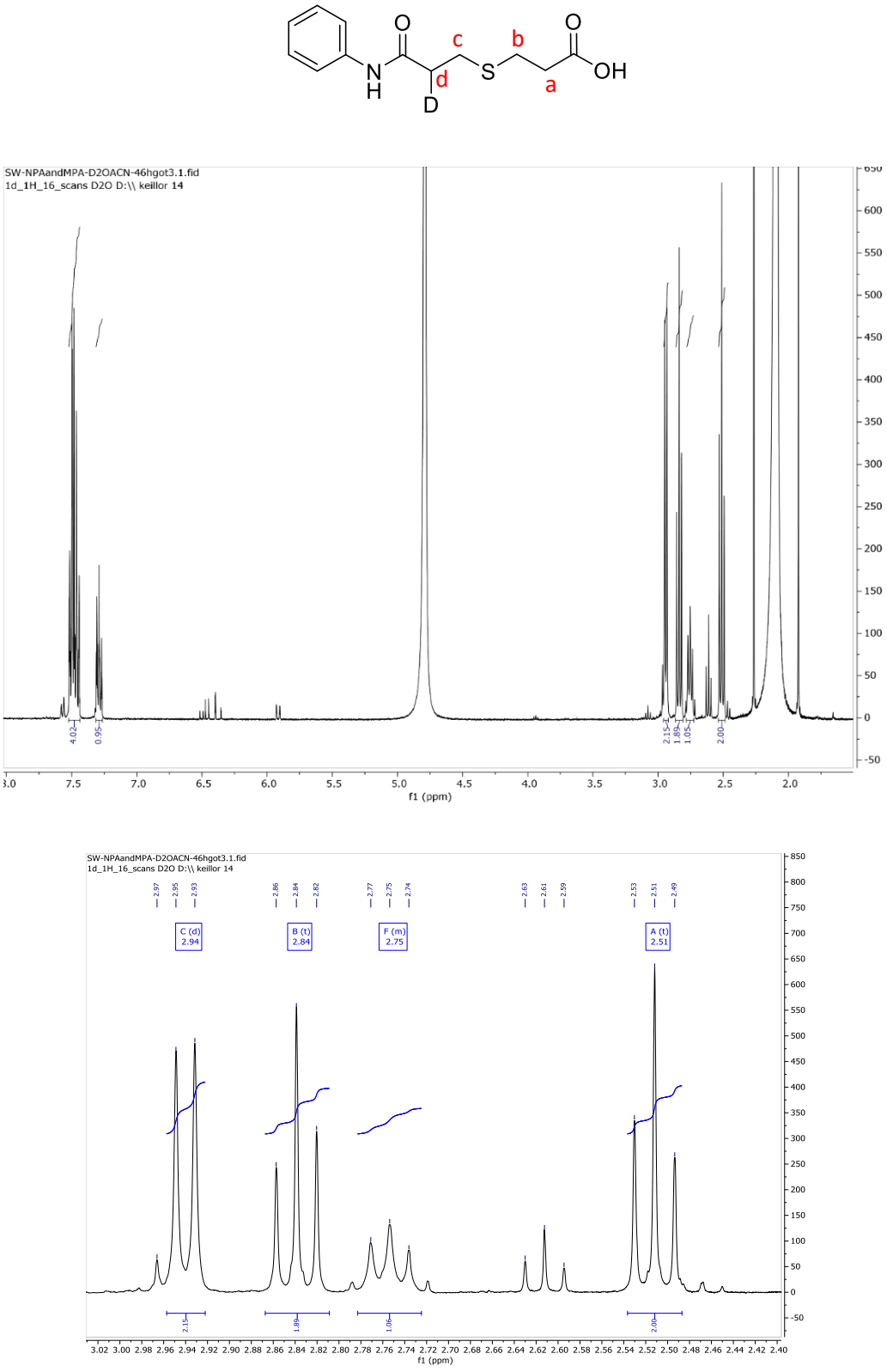

Figure S2.19. ^{1}H-NMR spectra of adduct formed on reaction of MPA with NPA in D_2O.

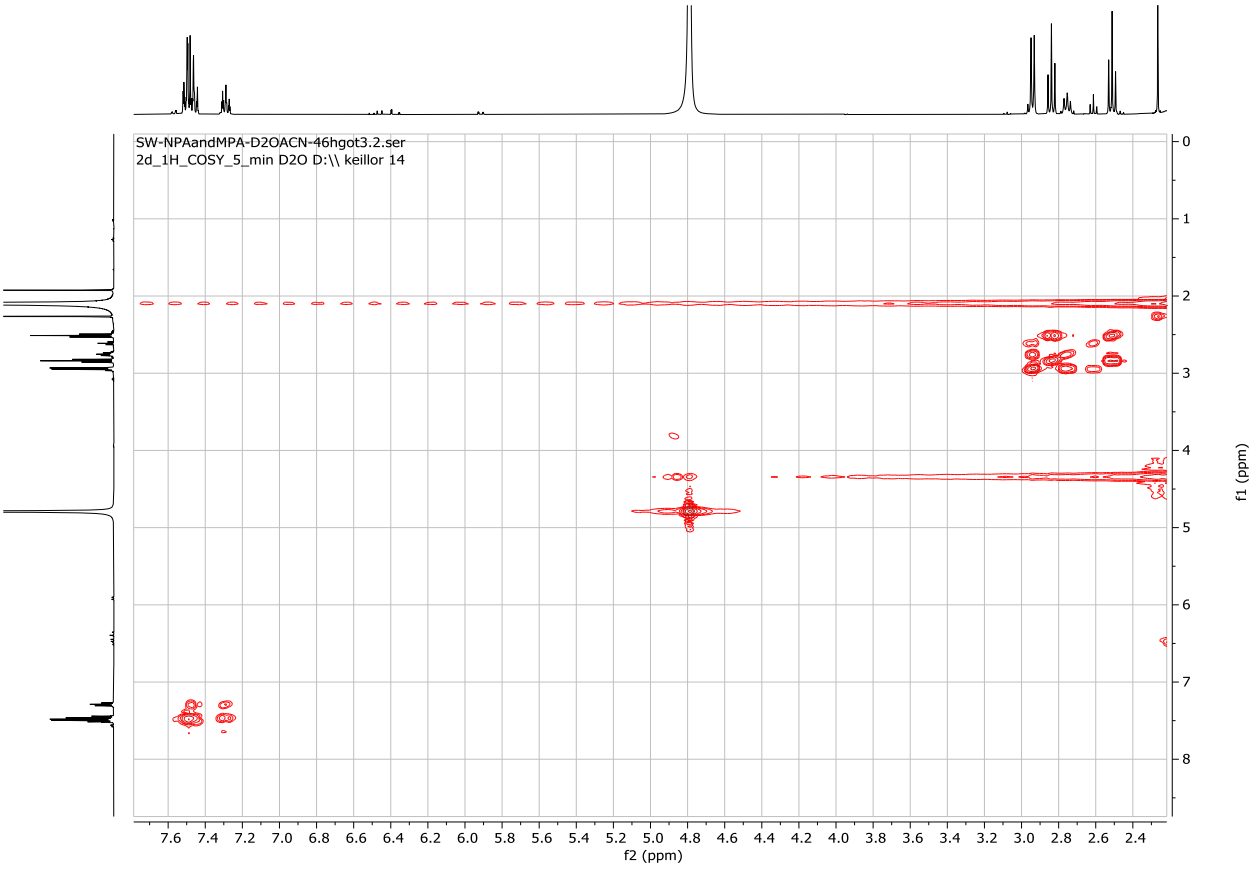

Figure S2.20. COSY spectrum of adduct formed on reaction of MPA with NPA in D_2O.

Table S2.7. DFT Coordinates

Methylthiol (HF=-438.7161991, NImag=0)

C	-1.149875	0.019721	0.000000
H	-1.521320	-1.004113	-0.000000
H	-1.511252	0.526248	-0.892471
H	-1.511252	0.526248	0.892472
S	0.658342	-0.087240	0.000000
H	0.909595	1.229124	0.000000

Methylthiolate (HF=-438.2236907, NImag=0)

C	0.000000	0.000000	-1.122213
H	0.000000	1.015846	-1.529501
H	-0.879748	-0.507923	-1.529501
H	0.879748	-0.507923	-1.529501
S	-0.000000	-0.000000	0.707611

N-Phenylacrylamide (HF=-478.3703966, NImag=0)

C	3.611710	-1.057555	0.511104
H	2.943491	-1.687752	1.087579
C	3.196285	0.005129	-0.163180
H	3.899237	0.636878	-0.693779
C	1.799390	0.510568	-0.209297
O	1.587295	1.701990	-0.426736
N	0.824035	-0.405284	-0.009116
H	1.117902	-1.369748	0.014188
C	-0.569202	-0.208055	0.010601
C	-1.371784	-1.312387	-0.271567
C	-1.162741	1.009409	0.331819
C	-2.750400	-1.199130	-0.243131
H	-0.905735	-2.260536	-0.513364
C	-2.546679	1.111531	0.350031
H	-0.553845	1.866461	0.572571
C	-3.347123	0.016745	0.062630

H	-3.360050	-2.065916	-0.465224
H	-2.999592	2.062864	0.600122
H	-4.425523	0.107605	0.080544
H	4.660775	-1.326323	0.521009

TS (HF=-916.5980778,NImag=1)

C	-2.727797	0.851973	-1.013713
H	-2.207420	0.519948	-1.900693
C	-2.080776	1.625548	-0.071959
H	-2.644296	2.239193	0.619734
C	-0.671971	1.542937	0.176270
O	-0.045133	2.351146	0.892075
N	-0.045223	0.455867	-0.404303
H	-0.680212	-0.312430	-0.619163
C	1.290990	0.078931	-0.230859
C	1.581322	-1.280803	-0.108799
C	2.339597	0.998132	-0.231149

C	2.891165	-1.712022	0.018433
H	0.767313	-1.997348	-0.115973
C	3.646755	0.556727	-0.090002
H	2.134338	2.051444	-0.352629
C	3.933580	-0.795304	0.036583
H	3.095901	-2.771609	0.110617
H	4.451022	1.282407	-0.090190
H	4.957278	-1.130959	0.141980
H	-3.791777	0.991548	-1.148428
S	-2.838250	-1.464237	-0.339721
C	-2.390145	-1.207362	1.385045
H	-3.188602	-1.511813	2.063776
H	-1.480812	-1.749675	1.651576
H	-2.199425	-0.135692	1.549347

Enolate (HF=-916.609191, NImag=0)

C	-2.601821	0.459994	-1.081563
H	-2.048393	0.188402	-1.985195
C	-1.895894	1.449839	-0.230996
H	-2.480458	2.248619	0.209289
C	-0.570338	1.377295	0.138317
O	0.058783	2.244058	0.834645
N	0.128672	0.214691	-0.281346
H	-0.456169	-0.607736	-0.336465
C	1.480567	-0.049635	-0.123602
C	1.888285	-1.370192	0.101229
C	2.466167	0.935822	-0.247493
C	3.230963	-1.692528	0.203745
H	1.135427	-2.145108	0.195617
C	3.806623	0.603379	-0.128703
H	2.177516	1.957549	-0.444550
C	4.204314	-0.707698	0.097427

H	3.516719	-2.723304	0.376383
H	4.551591	1.384189	-0.227099
H	5.253808	-0.958072	0.184410
H	-3.566665	0.853870	-1.401512
S	-2.954386	-1.214978	-0.337209
C	-3.749863	-0.723380	1.198678
H	-4.682050	-0.191465	1.003308
H	-3.970368	-1.629144	1.763181
H	-3.085759	-0.090825	1.788007

Product (HF=-917.1271492,NImag=0)

C	-2.757135	0.311344	0.070894
H	-2.799026	1.145112	-0.630138
C	-1.550151	-0.562626	-0.209756
H	-1.593037	-0.962891	-1.227071
C	-0.245318	0.195474	-0.080425
O	-0.199322	1.416489	0.009391

N	0.848269	-0.603619	-0.090987
H	0.661027	-1.594797	-0.121901
C	2.210508	-0.263251	-0.028946
C	2.691849	1.040777	-0.119371
C	3.113842	-1.317436	0.115218
C	4.059877	1.271217	-0.058089
H	2.009627	1.866266	-0.238488
C	4.473651	-1.073221	0.172280
H	2.739930	-2.332571	0.181382
C	4.957433	0.225991	0.088229
H	4.421606	2.289535	-0.129489
H	5.158422	-1.904509	0.284207
H	6.021472	0.418753	0.134341
H	-2.709159	0.716287	1.082762
S	-4.272549	-0.664633	-0.096759
C	-5.479475	0.620649	0.266039
H	-5.409606	1.433236	-0.457341

H	-6.468835	0.169222	0.196771
H	-5.338681	1.012155	1.273723
H	-1.526752	-1.421752	0.464744

S3. APPENDIX II: Supplementary information for Chapter 3

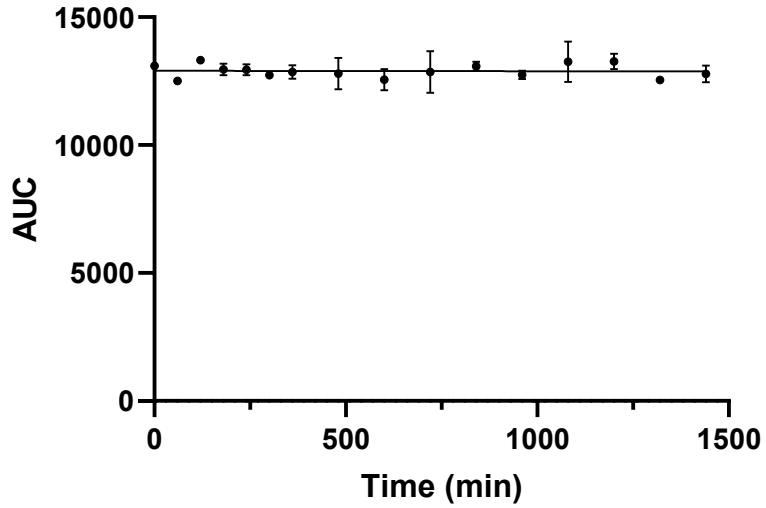

Figure S3.1. Plot of the integrated area under the curve (AUC) of AcrPip (2 mM) in the absence of thiol at 214 nm vs time (min) in 67 mM potassium phosphate buffer (1% v/v DMSO), pH=7.4, μ=0.100, T=22°C. The AUC data for AcrPip was monitored over the course of 24 hours to monitor its stability. The data were fit to a non-linear regression to afford a slope of -0.0178 ± 0.1456, that, once treated to an ANOVA analysis, was determined to not be statistically different from a slope of 0, with a *P* value of 0.9037.

Table S3.1. pH of buffer, mobile phase gradient, length of run and retention times of AcrPip and thiol-adduct for each experiment of AcrPip with RSH (**1a-e**).

Thiol	**pH of Aqueous Buffer**	**Mobile Phase Gradient (% CH_3CN in H_2O)**	**Total Length of Run (min)**	**Retention Time AcrPip (min)**	**Retention Time Adduct (min)**
1a	9.0	18-30	20	5.6	4.6
1b	8.0	15-50	20	7.7	3.4
1c	8.0	15-50	20	7.7	3.8
1d	10.0	12-35	20	10.2	11.1
1e	10.6	20-50	20	5.0	7.5

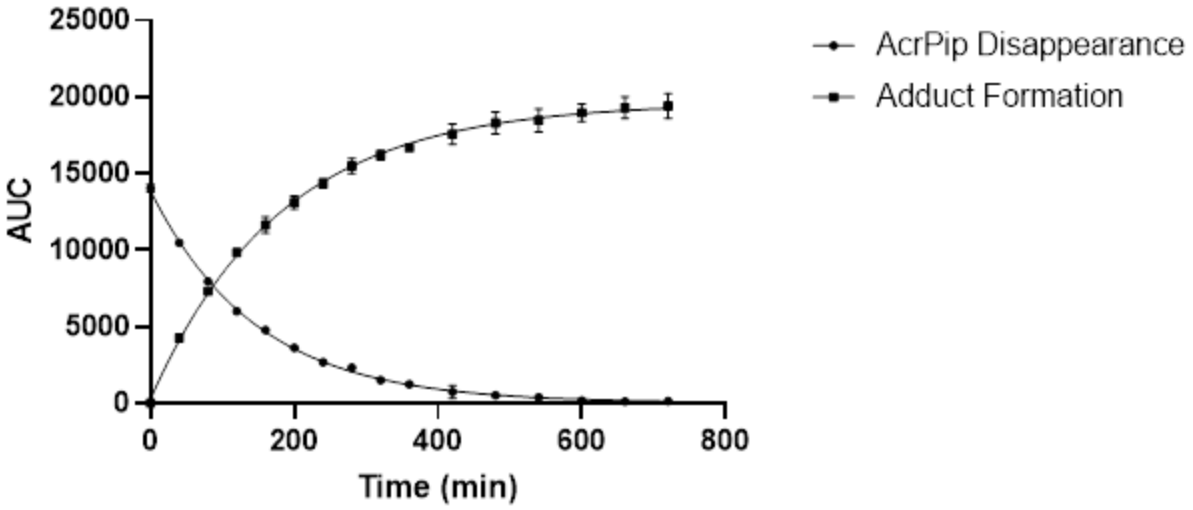

Figure S3.2. Plot of disappearance of AcrPip (2 mM) and formation of adduct for the addition of DEC (20 mM) vs time (min) in 67 mM CHES buffer (1% v/v DMSO), pH 9.0, μ = 0.100, T = 22°C. The area under the curve (AUC) was integrated from the chromatograph at 214 nm for the peaks corresponding to AcrPip and the adduct. The AUC data for disappearance of AcrPip were fitted to a mono-exponential decay with the constraint that the plateau = 0 and the data for formation of adduct were fitted to a mono-exponential association to afford the k_{obs} values summarized in **Table S3.2**.

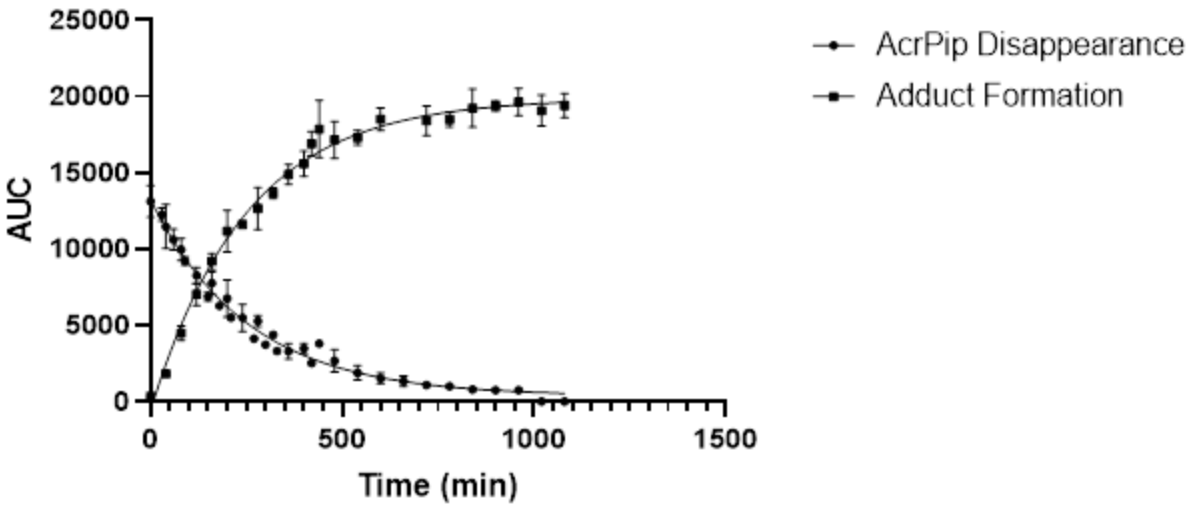

Figure S3.3. Plot of disappearance of AcrPip (2 mM) and formation of adduct for the addition of Cys (20 mM) vs time (min) in 67 mM TRIS buffer (1% v/v DMSO), pH 8.0, $\mu = 0.100$, T = 22°C. The area under the curve (AUC) was integrated from the chromatograph at 214 nm for the peaks corresponding to AcrPip and the adduct. The AUC data for disappearance of AcrPip were fitted to a mono-exponential decay with the constraint that the plateau = 0 and the data for formation of adduct were fitted to a mono-exponential association with the constraint that $Y_0 = 0$ to afford the k_{obs} values summarized in **Table S3.2**.

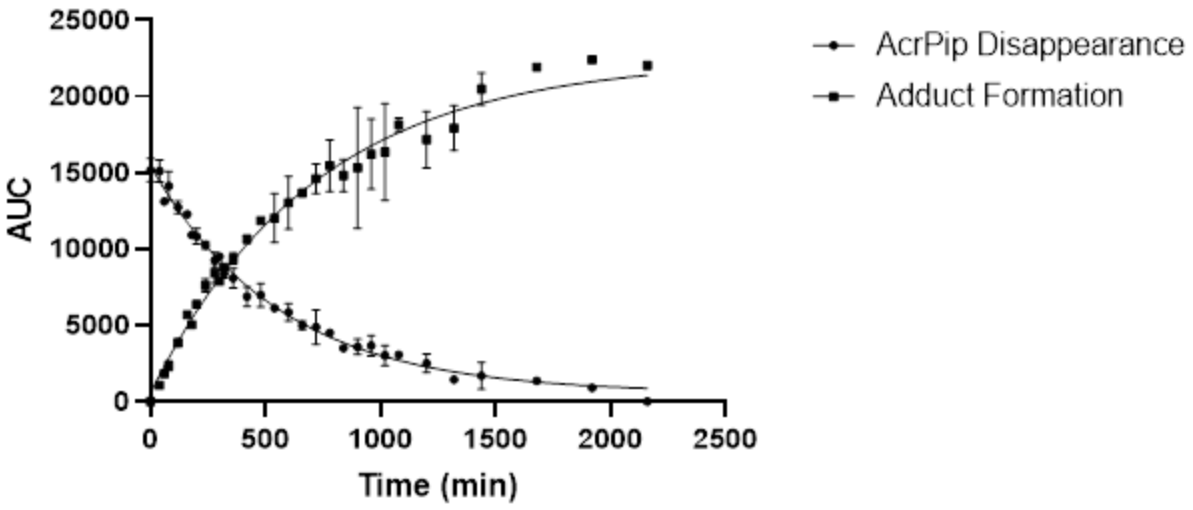

Figure S3.4. Plot of disappearance of AcrPip (2 mM) and formation of adduct for the addition of GSH (20 mM) vs time (min) in 67 mM TRIS buffer (1% v/v DMSO), pH 8.0, $\mu = 0.100$, T = 22°C. The area under the curve (AUC) was integrated from the chromatograph at 214 nm for the peaks corresponding to AcrPip and the adduct. The AUC data for disappearance of AcrPip were fitted to a mono-exponential decay with the constraint that the plateau = 0 and the data for formation of adduct were fitted to a mono-exponential association with the constraint that $Y_0 = 0$ to afford the k_{obs} values summarized in **Table S3.2**.

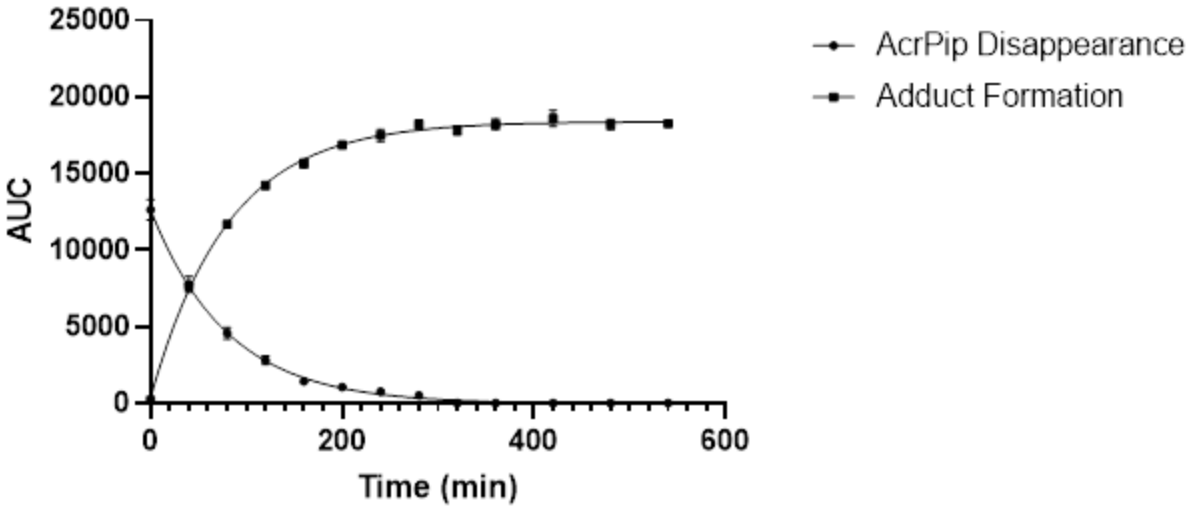

Figure S3.5. Plot of disappearance of AcrPip (2 mM) and formation of adduct for the addition of BME (20 mM) vs time (min) in 67 mM CAPS buffer (1% v/v DMSO), pH 10.0, $\mu = 0.100$, T = 22°C. The area under the curve (AUC) was integrated from the chromatograph at 214 nm for the peaks corresponding to AcrPip and the adduct. The AUC data for disappearance of AcrPip were fitted to a mono-exponential decay with the constraint that the plateau = 0 and the data for formation of adduct were fitted to a mono-exponential association with the constraint that $Y_0 = 0$ to afford the k_{obs} values summarized in **Table S3.2**.

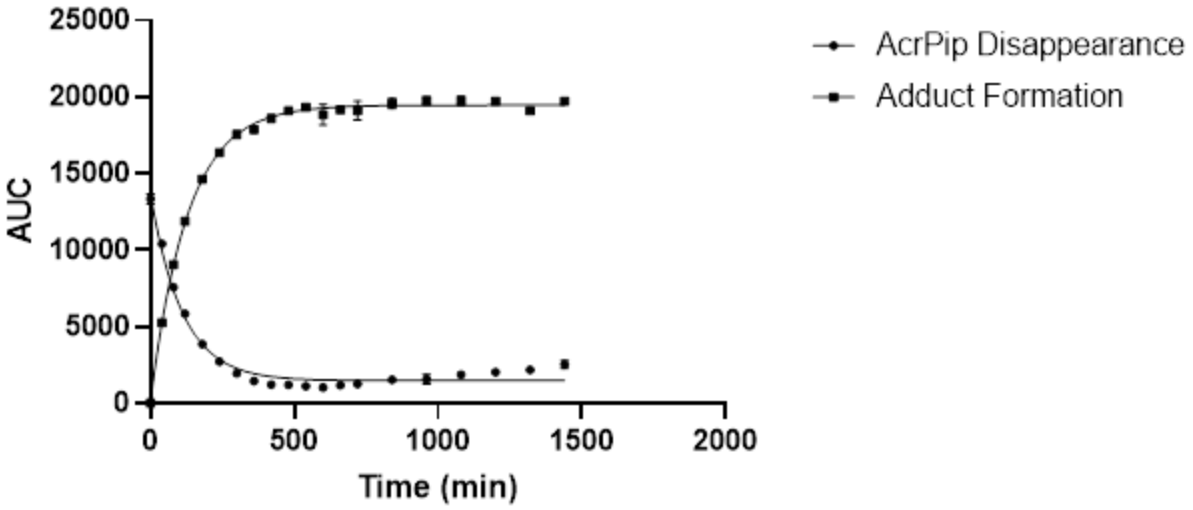

Figure S3.6. Plot of disappearance of AcrPip (2 mM) and formation of adduct for the addition of MPA (20 mM) vs time (min) in 67 mM CAPS buffer (1% v/v DMSO), pH 10.6, $\mu = 0.100$, T = 22°C. The area under the curve (AUC) was integrated from the chromatograph at 214 nm for the peaks corresponding to AcrPip and the adduct. The AUC data for disappearance of AcrPip were fitted to a mono-exponential decay and the data for formation of adduct were fitted to a mono-exponential association with the constraint that $Y_0 = 0$ to afford the k_{obs} values summarized in **Table S3.2**.

Table S3.2. Observed rate constants (k_{obs}), calculated second order rate constants (k_2^{calc}), and corrected second order rate constants (k_2^{corr}) for the addition of RSH (**1a-e**) to AcrPip. Measurements were made in duplicate for both the disappearance of acrylamide and appearance of adduct, unless otherwise indicated. Errors represent the standard deviation of the replicate values.

Thiol	**k_{obs} (s^{-1})**	**k_2^{calc} ($M^{-1}s^{-1}$)**	**k_2^{corr} ($M^{-1}s^{-1}$)**	**log(k_2^{corr})**
1a (2)	0.104 ± 0.011	0.00518 ± 0.00057	0.00551 ± 0.00061	-2.439 ± 0.048
1b[a] (3)	0.0653 ± 0.0065	0.00326 ± 0.00033	0.00977 ± 0.00097	-2.0051 ± 0.0516
1c[a] (3)	0.0274 ± 0.0040	0.00137 ± 0.00020	0.00824 ± 0.00121	-2.0840 ± 0.0671
1d (2)	0.212 ± 0.009	0.0106 ± 0.0005	0.0148 ± 0.0007	-1.830 ± 0.020
1e (2)	0.140 ± 0.013	0.00699 ± 0.00063	0.0105 ± 0.0009	-1.981 ± 0.039

[a]Measurements made in triplicate.

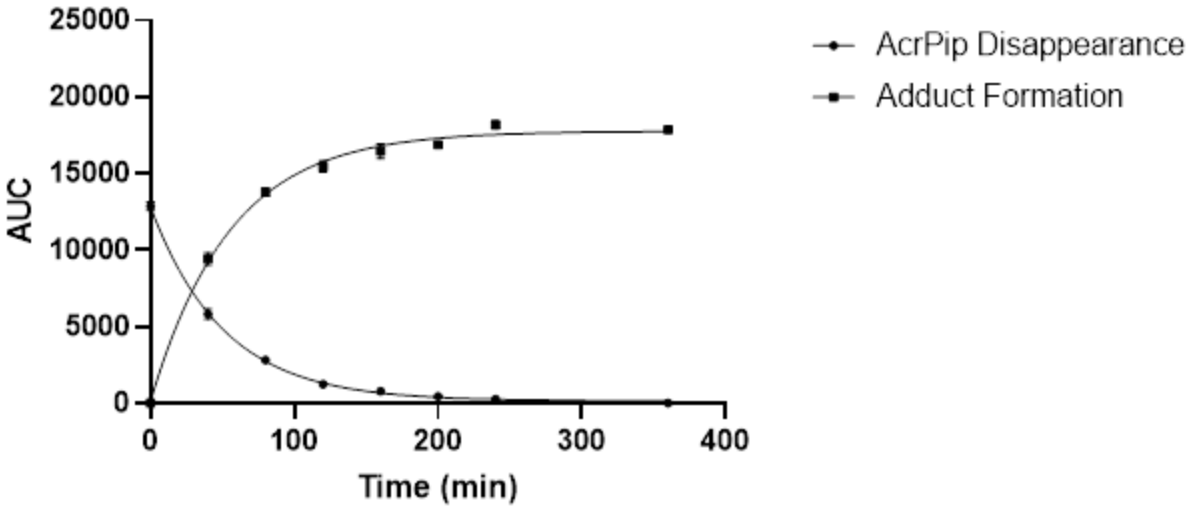

Figure S3.7. Plot of disappearance of AcrPip (2 mM) and formation of adduct for the addition of 1a (20 mM) vs time (min) in 67 mM CHES buffer (1% v/v DMSO) at pH 9.0, $\mu = 0.100$, T = 38°C. The area under the curve (AUC) was integrated from the chromatograph at 214 nm for the peaks corresponding to AcrPip and the adduct. The AUC data for disappearance of AcrPip were fitted to a mono-exponential decay with the constraint that the plateau = 0 and the data for formation of adduct were fitted to a mono-exponential association with the constraint that $Y_0 = 0$ to afford the k_{obs} values summarized in **Table S3.3**.

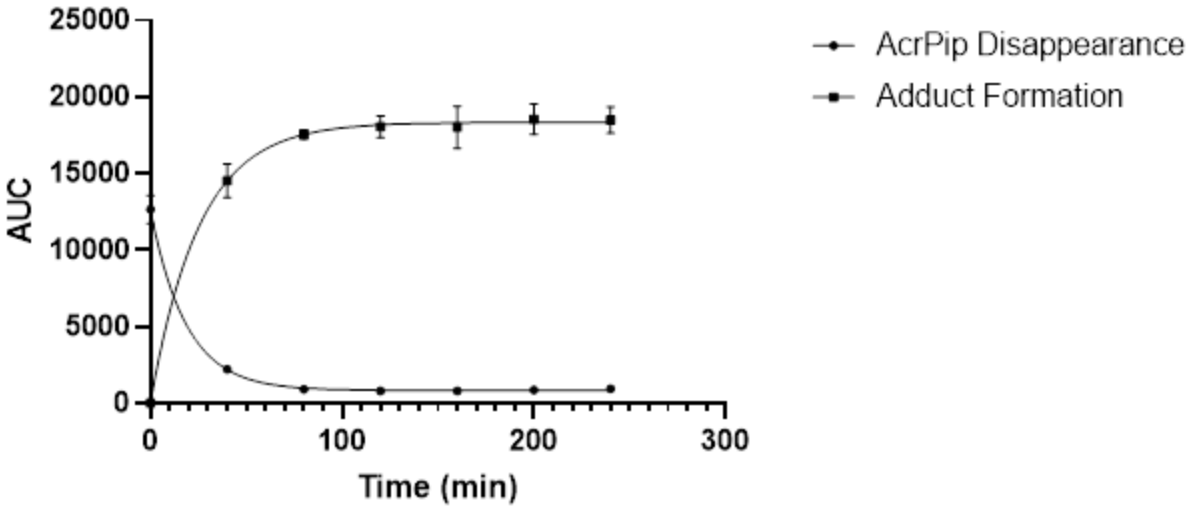

Figure S3.8. Plot of disappearance of AcrPip (2 mM) and formation of adduct for the addition of 1a (20 mM) vs time (min) in 67 mM CHES buffer (1% v/v DMSO) at pH 9.0, $\mu = 0.100$, T = 53°C. The area under the curve (AUC) was integrated from the chromatograph at 214 nm for the peaks corresponding to AcrPip and the adduct. The AUC data for disappearance of AcrPip were fitted to a mono-exponential decay and the data for formation of adduct were fitted to a mono-exponential association with the constraint that $Y_0 = 0$ to afford the k_{obs} values summarized in **Table S3.3**.

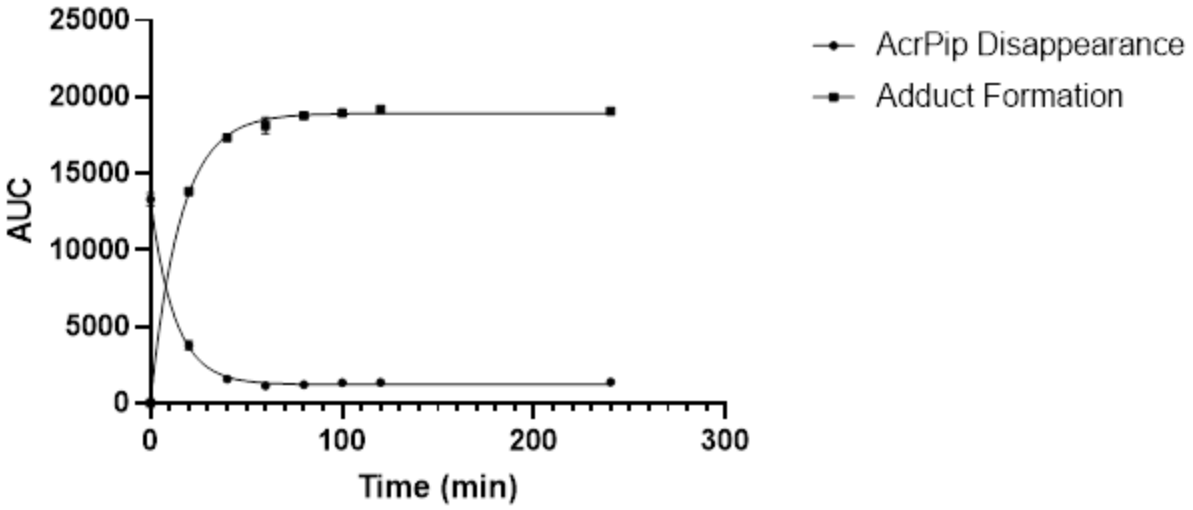

Figure S3.9. Plot of disappearance of AcrPip (2 mM) and formation of adduct for the addition of 1a (20 mM) vs time (min) in 67 mM CHES buffer (1% v/v DMSO) at pH 9.0, $\mu = 0.100$, T = 62°C. The area under the curve (AUC) was integrated from the chromatograph at 214 nm for the peaks corresponding to AcrPip and the adduct. The AUC data for disappearance of AcrPip were fitted to a mono-exponential decay and the data for formation of adduct were fitted to a mono-exponential association with the constraint that $Y_0 = 0$ to afford the k_{obs} values summarized in **Table S3.3**.

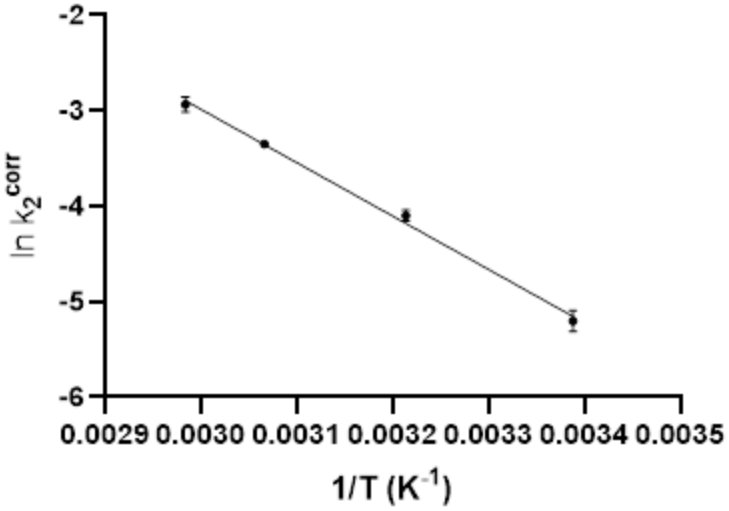

Figure S3.10. Arrhenius plot showing ln(k_2^{corr}) vs 1/T for the addition of 1a to AcrPip in 67 mM CHES buffer (1% v/v DMSO), pH = 9.0, μ = 0.100. The data were fitted to a linear regression to obtain a slope of -4308 ± 173.3 and y-intercept of 12.49 ± 0.55.

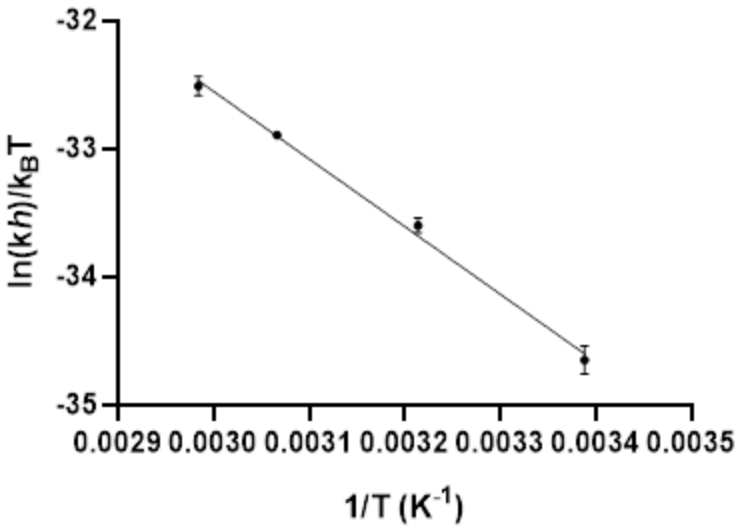

Figure S3.11. Eyring plot showing $\ln((k_2h)/(k_BT))$ vs 1/T for the addition of 1a to AcrPip in 67 mM CHES buffer (1% v/v DMSO), pH = 9.0, $\mu = 0.100$. The data were fitted to a linear regression to obtain a slope of -3994 ± 177.2 and y-intercept of -18.02 ± 0.56.

Table S3.3. Observed rate constants (k_{obs}), calculated second order rate constants (k_2^{calc}), and corrected second order rate constants (k_2^{corr}) for the addition of DEC (**1a**) to AcrPip at variable temperatures. Measurements were made in duplicate for both the disappearance of acrylamide and appearance of adduct. Errors represent the standard deviation of the replicate values.

Temp (°C)	**k_{obs} (s^{-1})**	**k_2^{calc} ($M^{-1}s^{-1}$)**	**k_2^{corr} ($M^{-1}s^{-1}$)**	**$\ln(k_2^{corr})$**	**$\ln((k_2^{corr}h)/k_BT)$**
22	0.104 ± 0.0114	0.00518 ± 0.00057	0.00551 ± 0.00061	-5.201 ± 0.110	-34.649 ± 0.111
38	0.312 ± 0.0176	0.0156 ± 0.0009	0.0166 ± 0.0009	-4.098 ± 0.055	-33.599 ± 0.057
53	0.663 ± 0.0170	0.0332 ± 0.0009	0.0352 ± 0.0009	-3.347 ± 0.026	-32.894 ± 0.026
62	0.998 ± 0.0767	0.0499 ± 0.0038	0.0531 ± 0.0041	-2.936 ± 0.076	-32.510 ± 0.077

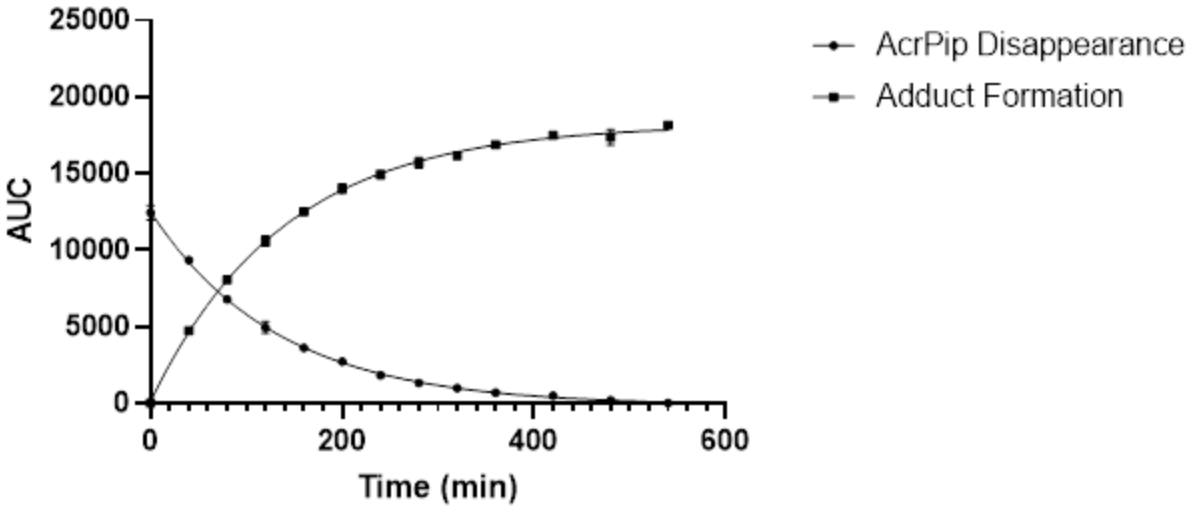

Figure S3.12. Plot of disappearance of AcrPip (2 mM) and formation of adduct for the addition of 1a (20 mM) vs time (min) in 67 mM CHES buffer (1% v/v DMSO), pH 9.0, μ = 0.050, T = 22°C. The area under the curve (AUC) was integrated from the chromatograph at 214 nm for the peaks corresponding to AcrPip and the adduct. The AUC data for disappearance of AcrPip were fitted to a mono-exponential decay with the constraint that the plateau = 0 and the data for formation of adduct were fitted to a mono-exponential association with the constraint that $Y_0 = 0$ to afford the k_{obs} values summarized in **Table S3.4**.

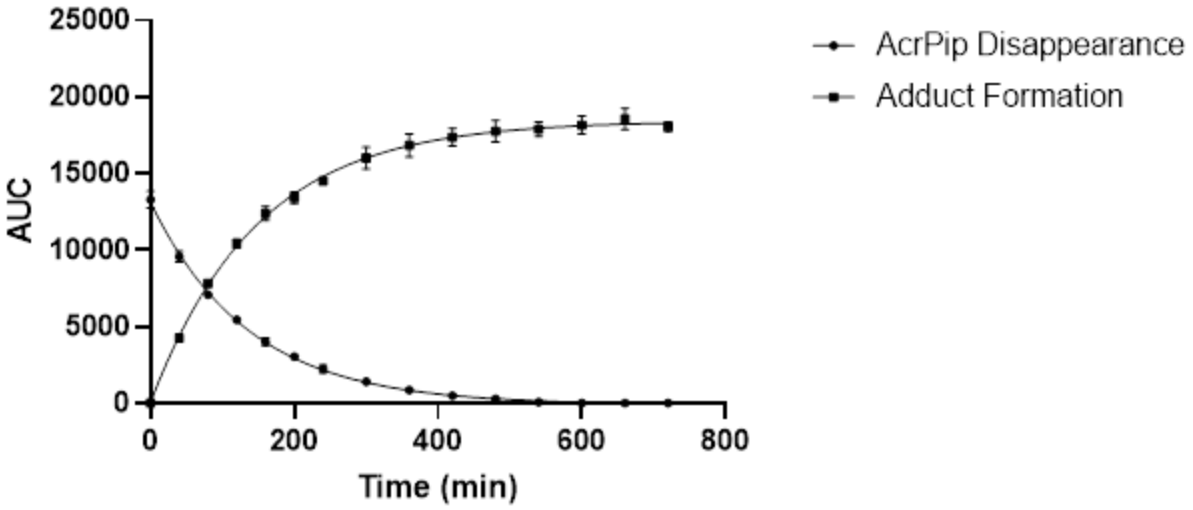

Figure S3.13. Plot of disappearance of AcrPip (2 mM) and formation of adduct for the addition of 1a (20 mM) vs time (min) in 67 mM CHES buffer (1% v/v DMSO), pH 9.0, μ = 0.075, T = 22°C. The area under the curve (AUC) was integrated from the chromatograph at 214 nm for the peaks corresponding to AcrPip and the adduct. The AUC data for disappearance of AcrPip were fitted to a mono-exponential decay with the constraint that the plateau = 0 and the data for formation of adduct were fitted to a mono-exponential association with the constraint that $Y_0 = 0$ to afford the k_{obs} values summarized in **Table S3.4**.

Table S3.4. Observed rate constants (k_{obs}), calculated second order rate constants (k_2^{calc}), and corrected second order rate constants (k_2^{corr}) for the addition of DEC (**1a**) to AcrPip at varying ionic strengths. Measurements were made in duplicate for both the disappearance of acrylamide and appearance of adduct. Errors represent the standard deviation of the replicate values.

[KCl] (M)	k_{obs} (s^{-1})	k_2^{calc} ($M^{-1}s^{-1}$)	k_2^{corr} ($M^{-1}s^{-1}$)
0.050	0.120 ± 0.008	0.00601 ± 0.00039	0.00639 ± 0.00041
0.075	0.119 ± 0.007	0.00595 ± 0.00037	0.00633 ± 0.00039
0.100	0.104 ± 0.011	0.00518 ± 0.00057	0.00551 ± 0.00061

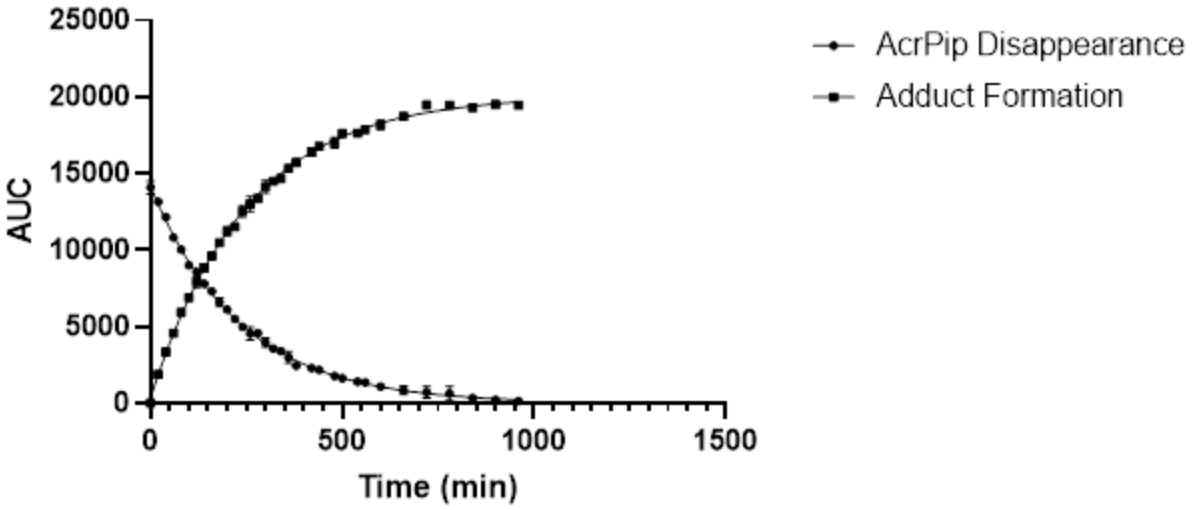

Figure S3.14. Plot of disappearance of AcrPip (2 mM) and formation of adduct for the addition of 1a (20 mM) vs time (min) in carbonate buffer prepared in D_2O (1% v/v ACN), pD = 9.6, μ = 0.100, T = 22°C. The area under the curve (AUC) was integrated from the chromatograph at 214 nm for the peaks corresponding to AcrPip and the adduct. The AUC data for disappearance of AcrPip were fitted to a mono-exponential decay with the constraint that the plateau = 0 and the data for formation of adduct were fitted to a mono-exponential association with the constraint that $Y_0 = 0$ to afford the k_{obs} values summarized in **Table S3.5**.

Table S3.5. Observed rate constants (k_{obs}), calculated second order rate constants (k_2^{calc}), corrected second order rate constants (k_2^{corr}), and calculated solvent kinetic isotope effect ratio for the addition of DEC (**1a**) to AcrPip. Measurements were made in duplicate for both the disappearance of acrylamide and appearance of adduct. Errors represent the standard deviation of the replicate values.

L_2O	k_{obs} (s^{-1})	k_2^{calc} ($M^{-1}s^{-1}$)	k_2^{corr} ($M^{-1}s^{-1}$)	$k_2^{corr,H2O}/k_2^{corr,D2O}$
H	0.104 ± 0.011	0.00518 ± 0.00057	0.00551 ± 0.00061	1.52 ± 0.17
D	0.0701 ± 0.0023	0.00351 ± 0.00011	0.00363 ± 0.00012	

From unpaired t-test ($P < 0.05$): P value = 0.0009, therefore statistically significantly different due to precision of measurements.

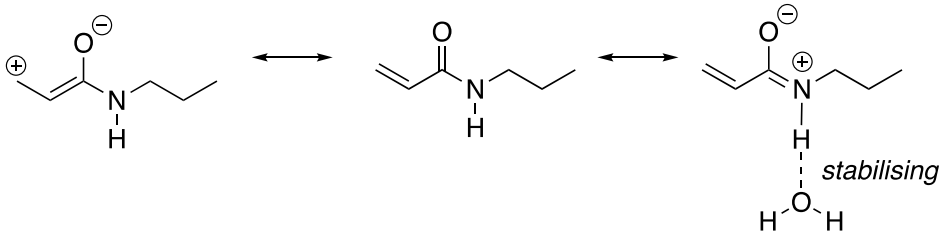

Scheme S3.1. Solvation hypothesis to explain lower reactivity of *N*-propylacrylamide compared to AcrPip.

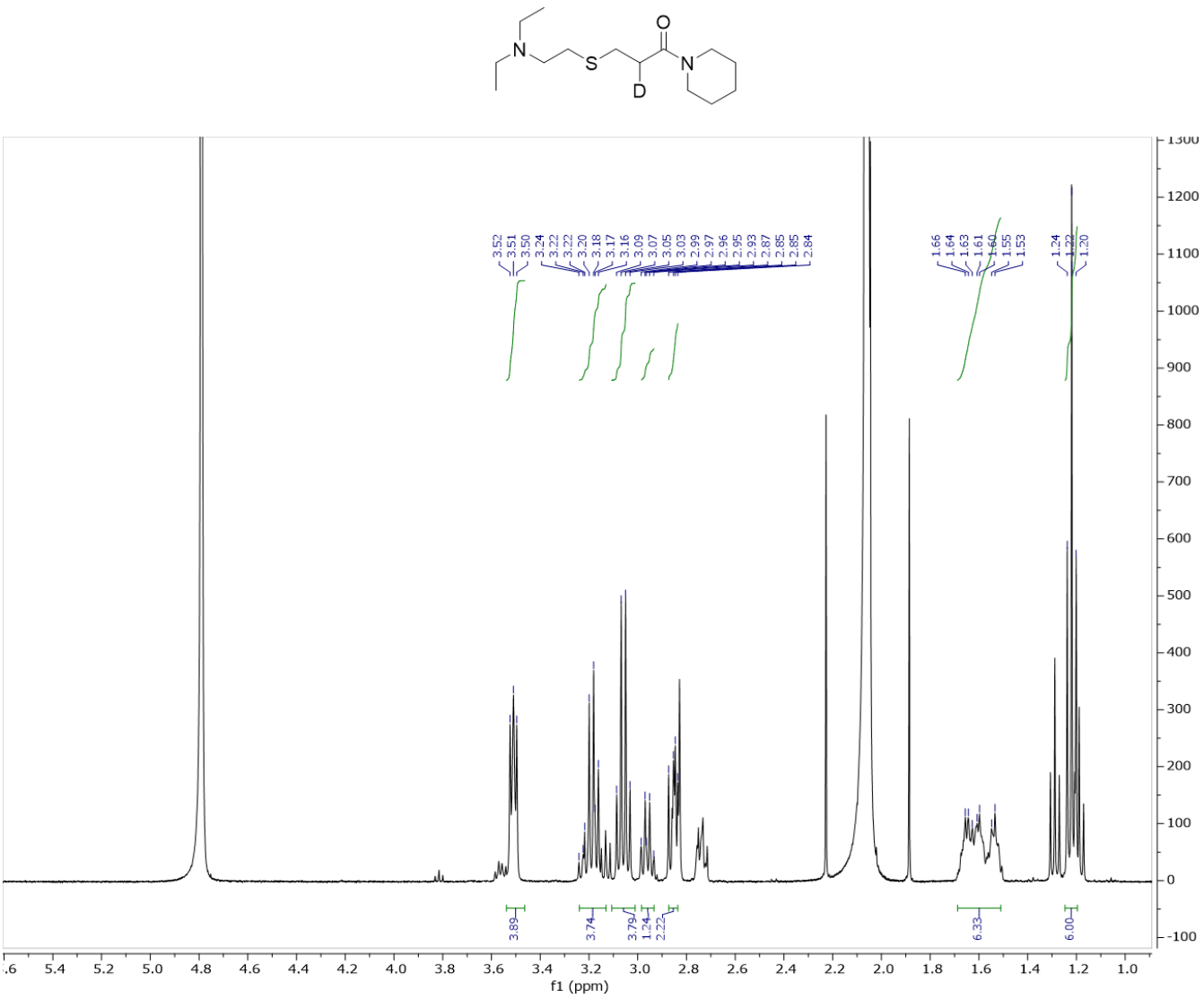

Figure S3.15. ^{1}H-NMR spectra of adduct formed for the reaction of DEC with AcrPip in D_2O.

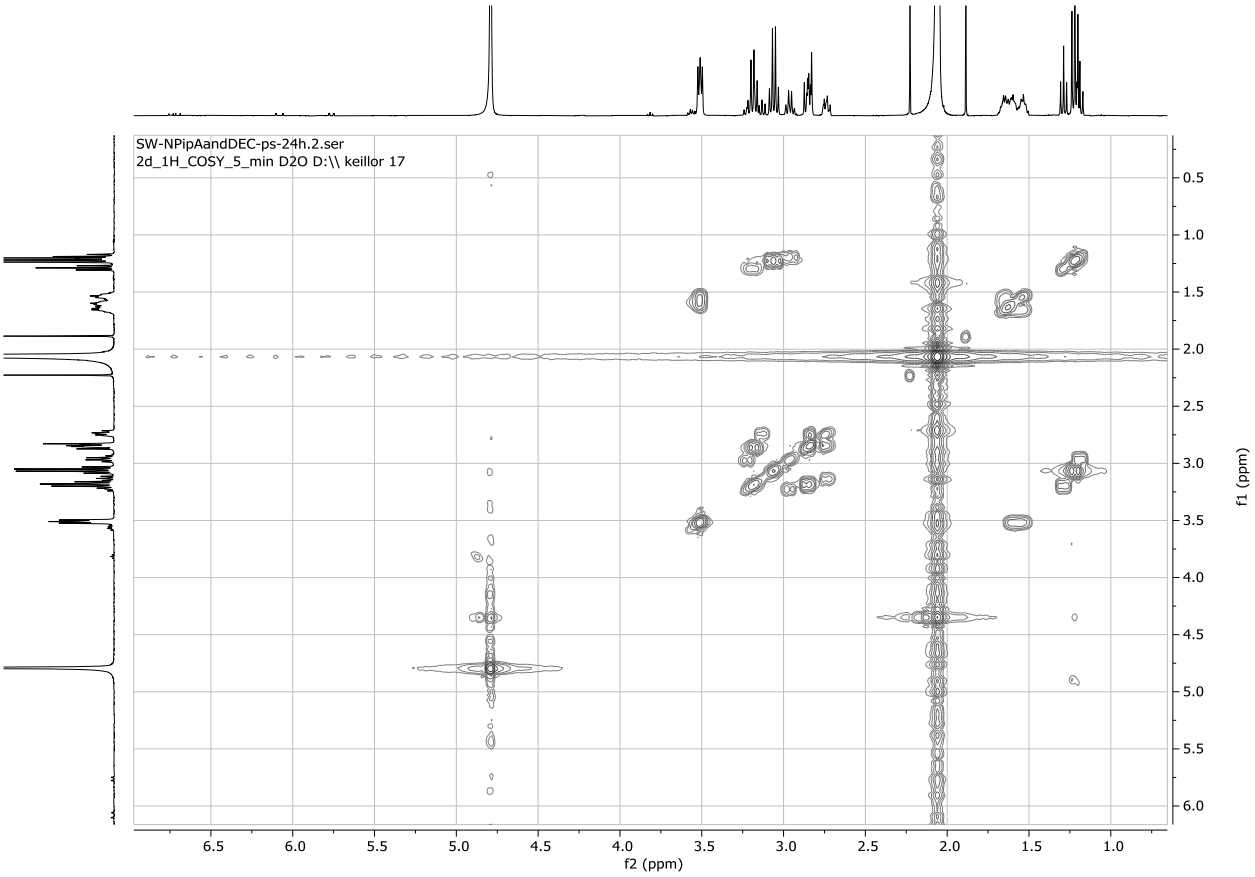

Figure S3.16. 2D-COSY spectrum of adduct formed of the reaction of DEC with AcrPip in D_2O.

Table S 3.6. Corrected second order rate constants (k_2^{corr}) for the addition of RSH (**1a-e**) to acrylamide derivatives *N*-phenylacrylamide, *N*-acryloylpiperidine, and *N*-propylacrylamide. Measurements were made in duplicate for both the disappearance of acrylamide and appearance of adduct, unless otherwise noted. Errors represent the standard deviation of the replicate values.

Thiol	***N*-phenylacrylamide k_2^{corr} ($M^{-1}s^{-1}$ x 10^3)**	***N*-acryloylpiperidine k_2^{corr} ($M^{-1}s^{-1}$ x 10^3)**	***N*-propylacrylamide k_2^{corr} ($M^{-1}s^{-1}$ x 10^3)[c]**
1a	130 ± 10[a]	5.51 ± 0.61	2.13 ± 0.03
1b	61 ± 6	9.77 ± 0.97[a]	/
1c	86 ± 5[b]	8.24 ± 1.21[a]	/
1d	220 ± 8	14.8 ± 0.7	8.64 ± 0.17
1e	118 ± 4	10.5 ± 0.9	3.48 ± 0.25

[a]Measurements made in triplicate. [b]Measurements made in quadruplet. [c]Observed only the disappearance of acrylamide.

Table S3.7. DFT Coordinates

N-acryloylpiperidine Addition

AcrPip coordinates

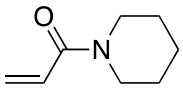

C	-2.578697	0.500760	-0.208097
C	-1.443299	1.501281	-0.008600
C	-0.370710	0.922289	0.905071
C	-0.945159	-1.358058	0.257056
C	-2.038031	-0.847629	-0.675803
H	0.463437	1.605303	1.022108
H	-0.993135	1.750847	-0.974203
H	-1.818871	2.429462	0.425896
H	-3.106549	0.365860	0.742079
H	-3.305833	0.887741	-0.923915
H	-0.498048	-2.274243	-0.116030
H	-1.364450	-1.561443	1.248811

H	-1.622526	-0.750321	-1.683230
H	-2.838725	-1.587891	-0.724363
H	-0.797149	0.746098	1.899388
N	0.105563	-0.357434	0.394970
C	1.384533	-0.674636	0.113441
C	2.431626	0.393611	0.108530
H	3.313251	0.149361	0.690657
C	2.406656	1.468333	-0.664079
H	1.547302	1.710343	-1.279116
H	3.253918	2.140363	-0.714655
O	1.743366	-1.818144	-0.167917

Transition State coordinates

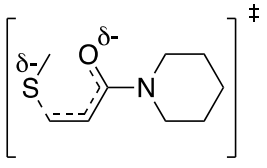

C	3.880381	-0.260308	0.560497
C	3.066893	-1.389872	-0.056165
C	1.571304	-1.208365	0.184383

C	1.864447	1.207145	0.317328
C	3.358407	1.080016	0.059184
H	1.039514	-1.981270	-0.361537
H	3.246766	-1.418964	-1.135450
H	3.372606	-2.356682	0.349529
H	3.787224	-0.298677	1.651680
H	4.940197	-0.377992	0.325719
H	1.472360	2.127777	-0.103062
H	1.693500	1.239535	1.405914
H	3.545292	1.168356	-1.015703
H	3.876499	1.907308	0.549304
H	1.353305	-1.347793	1.254973
N	1.117451	0.098523	-0.255977
C	-0.184576	0.342964	-0.686346
C	-1.091765	-0.755808	-0.855915
H	-0.835787	-1.741718	-0.499981
C	-2.382978	-0.539370	-1.328364

H	-2.568107	0.364962	-1.890874
H	-2.952106	-1.397691	-1.658429
O	-0.513336	1.521168	-0.933534
C	-2.747645	0.046979	1.703738
H	-1.753472	-0.242431	1.328403
H	-2.671313	1.045926	2.135203
H	-3.032719	-0.654104	2.488981
S	-3.889752	-0.002240	0.315338

AcrPip enolate intermediate coordinates

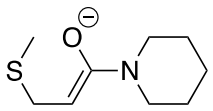

C	3.832210	-0.148769	0.748788
C	3.120321	-1.372146	0.187590
C	1.604446	-1.206815	0.219927
C	1.824633	1.193531	0.087712
C	3.341570	1.101653	0.030503
H	1.148215	-2.062494	-0.275299

H	3.434935	-1.530439	-0.848965
H	3.390918	-2.270074	0.748194
H	3.610067	-0.059231	1.818260
H	4.915331	-0.254797	0.655479
H	1.465918	2.050090	-0.475457
H	1.520221	1.340308	1.141775
H	3.658558	1.071264	-1.016942
H	3.774419	2.000666	0.475956
H	1.261419	-1.217238	1.270573
N	1.185368	0.004494	-0.456019
C	-0.198386	0.179687	-0.789361
C	-1.097974	-0.844558	-0.530440
H	-0.808216	-1.724480	0.024245
C	-2.518056	-0.722455	-0.911249
H	-2.656068	0.072951	-1.642707
H	-2.943277	-1.643375	-1.319652
O	-0.494404	1.281752	-1.343722

C	-2.964838	1.102930	1.204157
H	-1.886362	0.949015	1.272236
H	-3.168222	1.988535	0.602625
H	-3.377275	1.242882	2.202551
S	-3.709155	-0.371089	0.488955

AcrPip + Methanethiol product coordinates

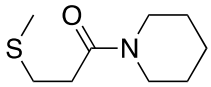

C	2.953957	-1.137321	0.203652
C	1.891651	-0.992022	1.288442
C	1.380042	0.442095	1.360111
C	1.912354	0.815089	-0.990991
C	2.435030	-0.609946	-1.130165
H	0.596777	0.533095	2.104727
H	1.052568	-1.661236	1.075631
H	2.292163	-1.274187	2.263677
H	3.843513	-0.568418	0.494566

H	3.259561	-2.180557	0.109110
H	1.465102	1.167098	-1.915232
H	2.736418	1.489491	-0.731412
H	1.625080	-1.250793	-1.490951
H	3.223120	-0.627225	-1.885130
H	2.196545	1.104309	1.670226
N	0.904293	0.892470	0.058909
C	-0.325713	1.381032	-0.213656
C	-1.375492	1.361943	0.883558
H	-2.179345	2.010070	0.540095
C	-1.945564	-0.023712	1.197537
H	-1.176440	-0.708856	1.555879
H	-2.678271	0.078237	1.998191
O	-0.623424	1.810731	-1.326769
C	-1.498710	-1.561348	-1.115367
H	-0.915287	-0.796787	-1.623807
H	-0.852061	-2.168254	-0.482102

H	-1.964039	-2.205149	-1.860494
S	-2.840731	-0.845177	-0.145347
H	-0.981693	1.793994	1.805644

N-Phenyl Acrylamide Addition

N-Phenyl Acrylamide coordinates

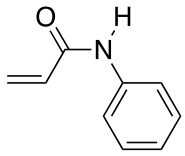

N	-0.817394	-0.390525	0.111458
C	-1.811687	0.535694	0.161133
C	-3.198882	-0.011127	0.167526
H	-3.912699	0.630486	0.670508
C	-3.594658	-1.114036	-0.451488
H	-2.914896	-1.749216	-1.008073
H	-4.635181	-1.411756	-0.441002
O	-1.628387	1.742514	0.199524
C	0.572567	-0.198952	0.045432
C	1.376206	-1.328784	0.206364
C	1.170207	1.038036	-0.187097
C	2.753456	-1.224665	0.138285
H	0.916041	-2.293639	0.385586

C	2.554097	1.127122	-0.250820
H	0.558463	1.916169	-0.312595
C	3.353337	0.006748	-0.089664
H	3.360098	-2.112227	0.265436
H	3.007867	2.093537	-0.431761
H	4.431036	0.089503	-0.141529
H	-1.109726	-1.349503	0.198996

Transition State coordinates

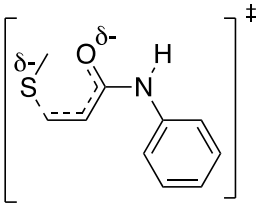

N	0.006810	0.384780	-0.341008
C	0.665494	1.545935	0.066249
C	2.058632	1.567486	-0.252740
H	2.658271	2.276437	0.303650
C	2.669751	0.656422	-1.115196
H	2.106461	0.262131	-1.951768

H	3.712219	0.826887	-1.349860
O	0.065694	2.442585	0.679462
C	2.616322	-1.017135	1.493774
H	2.337896	0.046432	1.540120
H	1.797275	-1.601134	1.914138
H	3.508360	-1.167166	2.102150
S	2.900306	-1.434276	-0.233201
C	-1.331573	0.045001	-0.180331
C	-1.667279	-1.313686	-0.215261
C	-2.357506	0.982542	-0.031562
C	-2.984289	-1.722613	-0.104166
H	-0.879562	-2.049948	-0.332638
C	-3.673105	0.558076	0.084222
H	-2.114739	2.032706	-0.002199
C	-4.001333	-0.789509	0.050418
H	-3.215703	-2.780339	-0.135011
H	-4.454120	1.300260	0.199013

H	-5.031656	-1.108247	0.140644
H	0.626498	-0.398862	-0.518105

Enolate intermediate coordinates

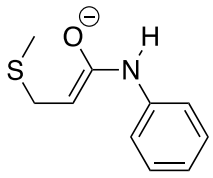

N	-0.147233	0.247730	-0.284529
C	0.595820	1.406804	0.083629
C	1.935579	1.429439	-0.279033
H	2.498399	2.284346	0.078137
C	2.679388	0.395513	-1.025300
H	2.047002	-0.226377	-1.662656
H	3.437002	0.830782	-1.680743
O	-0.011631	2.321158	0.704592
C	2.488133	-1.478558	1.092162
H	1.906202	-0.667059	1.531904
H	1.822325	-2.171593	0.575723

H	3.006501	-2.015438	1.885161
S	3.726512	-0.792639	-0.018783
C	-1.495394	-0.017195	-0.153593
C	-1.919172	-1.350368	-0.281028
C	-2.474824	0.963622	0.058057
C	-3.258073	-1.687655	-0.202677
H	-1.179596	-2.126896	-0.444824
C	-3.812542	0.607762	0.141789
H	-2.166419	1.991454	0.160714
C	-4.223117	-0.711930	0.013668
H	-3.548165	-2.726405	-0.307319
H	-4.548836	1.386182	0.306084
H	-5.270813	-0.975275	0.079187
H	0.401095	-0.549467	-0.551918

N-Phenylacrylamide + Methanethiol Product coordinates

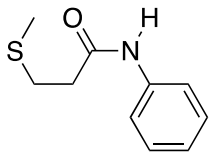

N	-0.181049	0.929395	-0.359670
C	0.804461	1.136531	0.556336
C	2.124657	1.575170	-0.045367
H	2.774089	1.854959	0.781596
C	2.803010	0.506343	-0.905672
H	2.200153	0.249153	-1.778340
H	3.743868	0.909923	-1.279508
O	0.664850	0.968197	1.755518
C	1.694091	-1.935662	-0.045197
H	0.982306	-1.520414	0.665686
H	1.257168	-1.954158	-1.043198
H	1.933460	-2.955145	0.253642
S	3.255455	-1.028269	-0.058452
C	-1.472484	0.407090	-0.180001

C	-2.302556	0.369622	-1.301626
C	-1.943227	-0.084714	1.035720
C	-3.581006	-0.149062	-1.210592
H	-1.939828	0.748823	-2.249999
C	-3.229380	-0.602413	1.111411
H	-1.310711	-0.057738	1.907551
C	-4.054751	-0.639215	-0.000638
H	-4.209686	-0.169793	-2.091648
H	-3.584606	-0.982173	2.061257
H	-5.055426	-1.044648	0.071785
H	0.050350	1.156931	-1.312876
H	1.963231	2.463099	-0.663408

AcrPip proton transfer from water cluster to enolate

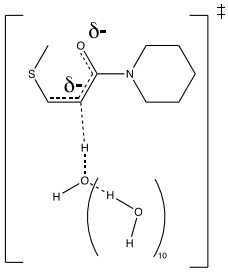

C	3.958629	1.507650	1.220799
C	3.256831	0.253015	1.734342
C	1.799162	0.245793	1.294916
C	2.271201	1.601594	-0.651499
C	3.749981	1.669021	-0.282204
H	1.277436	-0.639128	1.639339
H	3.756144	-0.638604	1.342377
H	3.307172	0.202079	2.824008
H	3.545231	2.381929	1.735686
H	5.023894	1.475799	1.457239
H	2.137148	1.635552	-1.728852
H	1.743622	2.464387	-0.223106

H	4.279452	0.873243	-0.814821
H	4.162497	2.619999	-0.626079
H	1.285459	1.103718	1.751033
N	1.681004	0.374733	-0.147114
C	0.909665	-0.421433	-0.954157
C	0.496823	-1.733477	-0.520699
H	-0.080615	-2.196013	-1.320230
C	1.462506	-2.713298	0.089078
H	2.092641	-2.279293	0.864118
H	0.922128	-3.545090	0.548429
O	0.512925	0.054835	-2.052973
C	3.578333	-2.187858	-1.681811
H	2.950280	-1.478055	-2.218344
H	4.085449	-1.676130	-0.864103
H	4.323132	-2.590932	-2.366830
S	2.607611	-3.574863	-1.066384
O	-1.406313	1.731203	1.113863

H	-1.141758	1.864991	0.179187
H	-0.927451	2.428839	1.600127
H	-3.144854	1.701203	0.937997
O	0.069096	3.904578	2.013991
O	-0.863737	2.249466	-1.552558
H	-1.772518	2.094798	-1.885250
O	-4.051194	1.515106	0.604865
H	-4.664841	2.004759	1.154716
H	0.198114	4.231200	1.099154
H	-0.311278	1.471160	-1.825419
H	0.946331	3.723731	2.356855
O	-1.306327	-1.167567	1.331477
H	-0.524691	-1.412252	0.506148
O	-3.488519	1.700567	-2.170820
H	-3.832384	1.739092	-1.262674
H	-3.487959	0.748268	-2.387579
O	-0.037684	-2.394223	3.406648

H	-0.519946	-1.950416	2.671546
H	0.671219	-2.879812	2.981930
H	-1.241028	-0.203429	1.423117
H	-2.810945	-1.297339	0.673271
O	-3.719007	-1.255478	0.258651
H	-4.017074	-0.346369	0.437304
H	-0.202513	3.792561	-1.075239
O	0.122480	4.613160	-0.646554
H	0.958386	4.819214	-1.069062
O	-5.408090	-3.203095	1.304618
H	-5.329539	-3.133139	2.256969
H	-4.818194	-2.510963	0.950466
H	-3.505822	-1.248111	-1.495024
O	-3.376479	-1.071825	-2.452121
H	-4.097140	-1.516614	-2.901744

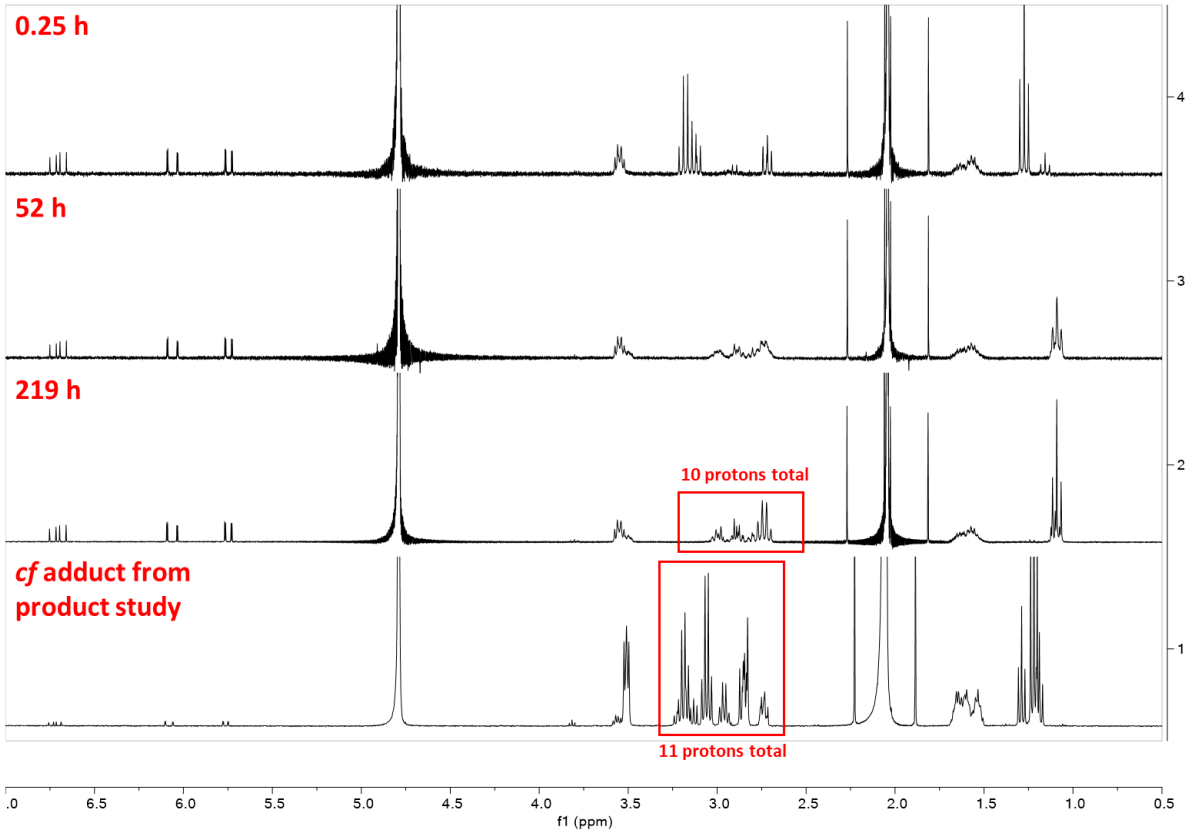

Figure S3.17. ^{1}H-NMR spectra of adduct formed from the reaction of DEC with AcrPip in D_2O, followed over several days in the presence of added carbonate base.

S4. APPENDIX III: Supplementary information for Chapter 4

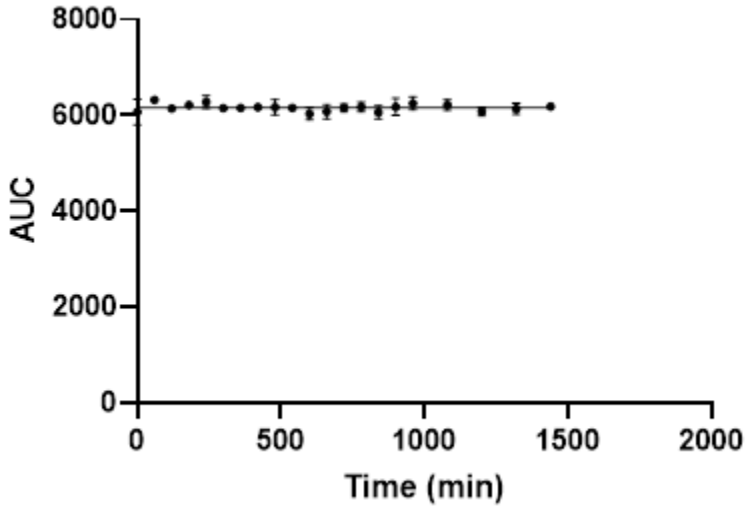

Figure S4.1. Stability of 1 mM NPC in aqueous buffer, pH=7.4, assessed over 24 hours. Data were fit to a linear regression to obtain a slope of -0.029 ± 0.042 that is not statistically significant from zero, P value = 0.4998, and y-intercept of 6179 ± 31.

Table S4.1. pH of buffer, mobile phase gradient, length of run and retention times of NPC and thiol-adduct for each experiment of NPC with RSH (**1a-d**).

Thiol	**[NPC] mM**	**[Thiol] mM**	**pH of Aqueous Buffer**	**Mobile Phase Gradient (% CH_3CN in H_2O)**	**Total Length of Run (min)**	**Retention Time NPC (min)**	**Retention Time Adduct (min)**
1a	2	20	6.80	20-80	15	8.6	4.5
1b	1	10	7.40	18-30	20	11.9	3.3
1c	2	20	8.00	20-80	15	8.6	5.8
1d	1	10	9.01	18-30	20	11.9	10.8

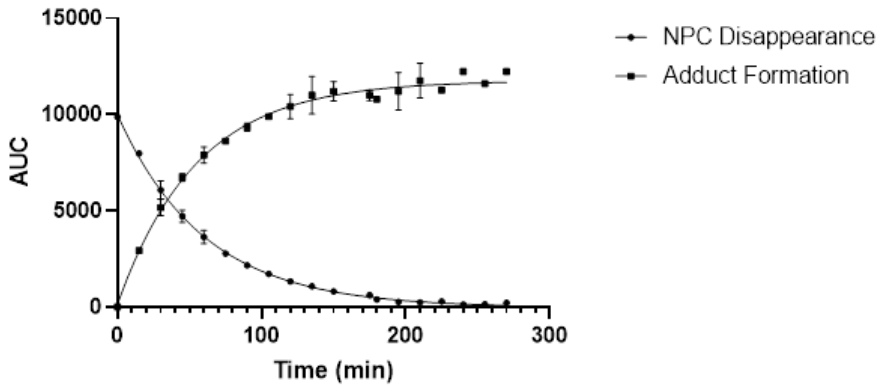

Figure S4.2. Plot of disappearance of NPC (2 mM) and formation of adduct for the addition of DEC (20 mM) vs time (min) in 67 mM MOPS buffer (1% v/v DMSO), pH 6.8, μ = 0.100, T = 22°C. The area under the curve (AUC) was integrated from the chromatograph at 214 nm for the peaks corresponding to NPC and the adduct. The AUC data for disappearance of NPC were fitted to a mono-exponential decay with the constraint that the plateau = 0 and the data for formation of adduct were fitted to a mono-exponential association to afford the k_{obs} values summarized in **Table S4.2**.

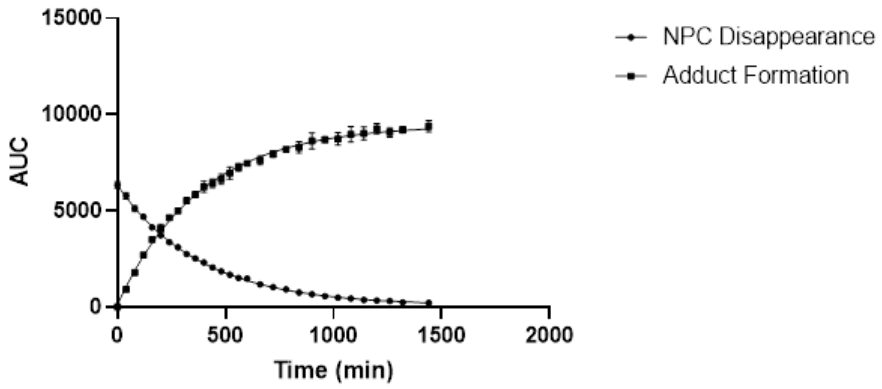

Figure S4.3. Plot of disappearance of NPC (1 mM) and formation of adduct for the addition of GSH (10 mM) vs time (min) in 67 mM potassium phosphate buffer (0.5% v/v DMSO), pH 7.4, μ = 0.100, T = 22°C. The area under the curve (AUC) was integrated from the chromatograph at 214 nm for the peaks corresponding to NPC and the adduct. The AUC data for disappearance of NPC were fitted to a mono-exponential decay with the constraint that the plateau = 0 and the data for formation of adduct were fitted to a mono-exponential association with the constraint that $Y_0 = 0$ to afford the k_{obs} values summarized in **Table S4.2**.

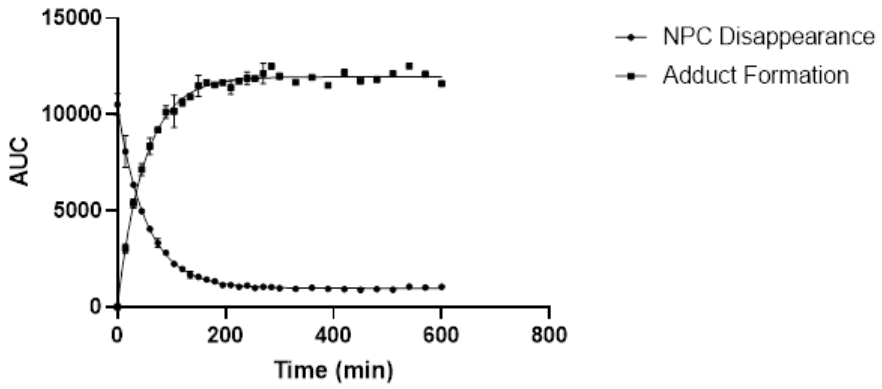

Figure S4.4. Plot of disappearance of NPC (2 mM) and formation of adduct for the addition of BME (20 mM) vs time (min) in 67 mM Tris buffer (1% v/v DMSO), pH=8.0, μ=0.100, T=22°C. The area under the curve (AUC) was integrated from the chromatograph at 214 nm for the peaks corresponding to NPC and the adduct. The AUC data for disappearance of NPC were fitted to a mono-exponential decay with the constraint that the plateau = 0 and the data for formation of adduct were fitted to a mono-exponential association with the constraint that $Y_0 = 0$ to afford the k_{obs} values summarized in **Table S4.2**.

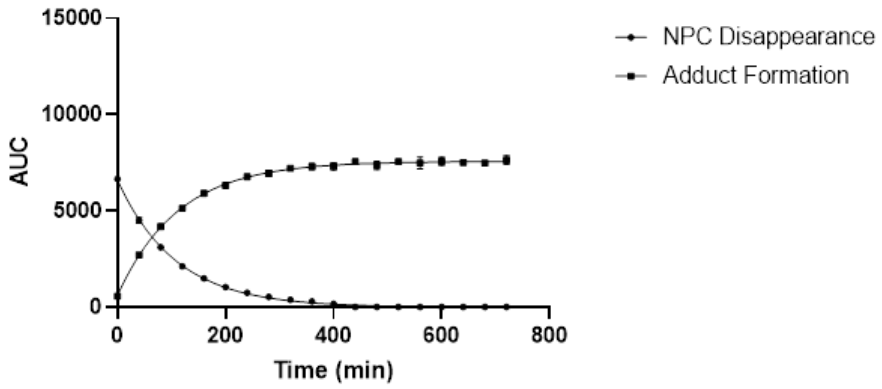

Figure S4.5. Plot of disappearance of NPC (1 mM) and formation of adduct for the addition of MPA (10 mM) vs time (min) in 67 mM CHES buffer (1% v/v DMSO), pH=9, μ=0.100, T=22°C. The area under the curve (AUC) was integrated from the chromatograph at 214 nm for the peaks corresponding to NPC and the adduct. The AUC data for disappearance of NPC were fitted to a mono-exponential decay with the constraint that the plateau = 0 and the data for formation of adduct were fitted to a mono-exponential association with the constraint that $Y_0 = 0$ to afford the k_{obs} values summarized in **Table S4.2**.

Table S4.2. Observed rate constants (k_{obs}), calculated second order rate constants (k_2^{calc}), and corrected second order rate constants (k_2^{corr}) for the addition of RSH (**1a-d**) to NPC. Measurements were made in duplicate for both the disappearance of chloroacetamide and appearance of adduct, providing quadruplicate measurements. Errors shown for k_{obs} and k_2^{calc} represent the standard error of the fitting. The errors shown for k_2^{calc} represent the propagated uncertainty including the uncertainty in *f* RS- (see Table 2).

Thiol	k_{obs} (10^{-3} s^{-1})	k_2^{calc} ($M^{-1}s^{-1}$)	k_2^{corr} ($M^{-1}s^{-1}$)	$\log(k_2^{corr})$
1a	0.2722 ± 0.0046	0.01361 ± 0.00023	0.150 ± 0.039	-0.825 ± 0.131
1a	0.2877 ± 0.0045	0.01491 ± 0.00023	0.158 ± 0.041	-0.801 ± 0.131
1a	0.3532 ± 0.0254	0.01766 ± 0.00127	0.194 ± 0.052	-0.712 ± 0.137
1a	0.2798 ± 0.0135	0.01399 ± 0.00068	0.154 ± 0.041	-0.813 ± 0.134
1b	0.04237 ± 0.00031	0.004237 ± 0.000031	0.0813 ± 0.0101	-1.090 ± 0.058
1b	0.04178 ± 0.00037	0.004178 ± 0.000037	0.0802 ± 0.0100	-1.096 ± 0.058
1b	0.04450 ± 0.00085	0.004450 ± 0.000085	0.0854 ± 0.0107	-1.068 ± 0.058
1b	0.04468 ± 0.00086	0.004468 ± 0.000086	0.0858 ± 0.0108	-1.067 ± 0.058
1c	0.3308 ± 0.0061	0.01654 ± 0.00031	0.645 ± 0.083	-0.190 ± 0.060
1c	0.2955 ± 0.0175	0.01478 ± 0.00087	0.577 ± 0.081	-0.239 ± 0.066
1c	0.3392 ± 0.0056	0.01696 ± 0.00028	0.662 ± 0.085	-0.179 ± 0.060
1c	0.3137 ± 0.0096	0.01568 ± 0.00048	0.612 ± 0.080	-0.213 ± 0.061
1d	0.1548 ± 0.0018	0.01548 ± 0.00018	0.297 ± 0.037	-0.527 ± 0.058
1d	0.1574 ± 0.0020	0.01574 ± 0.00020	0.302 ± 0.038	-0.520 ± 0.058
1d	0.1599 ± 0.0061	0.01599 ± 0.00061	0.307 ± 0.040	-0.513 ± 0.060
1d	0.1663 ± 0.0064	0.01663 ± 0.00064	0.319 ± 0.041	-0.496 ± 0.060

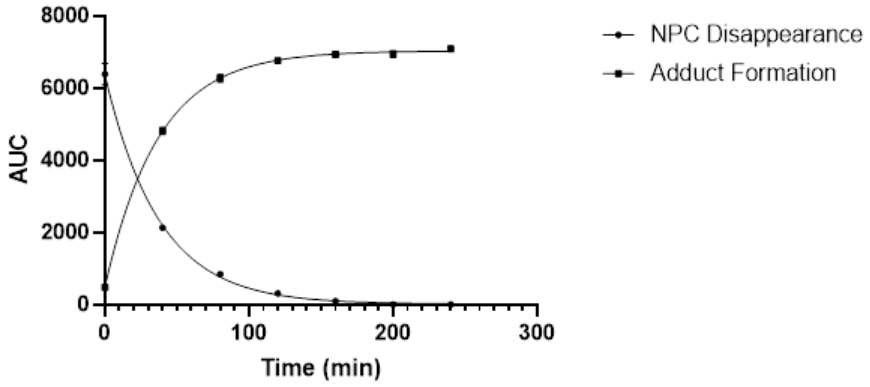

Figure S4.6. Plot of disappearance of NPC (1 mM) and formation of adduct for the addition of 1d (10 mM) vs time (min) in 67 mM CHES buffer (0.5% v/v DMSO) at pH 9.0, $\mu = 0.100$, T = 37°C. The area under the curve (AUC) was integrated from the chromatograph at 214 nm for the peaks corresponding to NPC and the adduct. The AUC data for disappearance of NPC were fitted to a mono-exponential decay with the constraint that the plateau = 0 and the data for formation of adduct were fitted to a mono-exponential association with the constraint that $Y_0 = 0$ to afford the k_{obs} values summarized in **Table S4.3**.

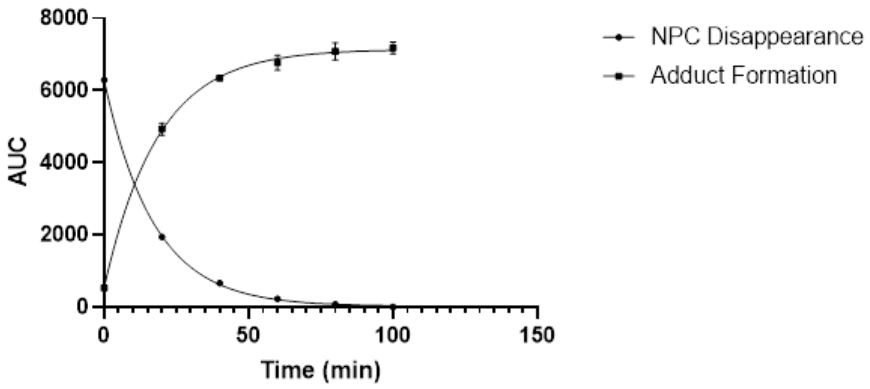

Figure S4.7. Plot of disappearance of NPC (1 mM) and formation of adduct for the addition of 1d (10 mM) vs time (min) in 67 mM CHES buffer (0.5% v/v DMSO) at pH 9.0, $\mu = 0.100$, T = 53°C. The area under the curve (AUC) was integrated from the chromatograph at 214 nm for the peaks corresponding to NPC and the adduct. The AUC data for disappearance of NPC were fitted to a mono-exponential decay with the constraint that the plateau = 0 and the data for formation of adduct were fitted to a mono-exponential association with the constraint that $Y_0 = 0$ to afford the k_{obs} values summarized in **Table S4.3**.

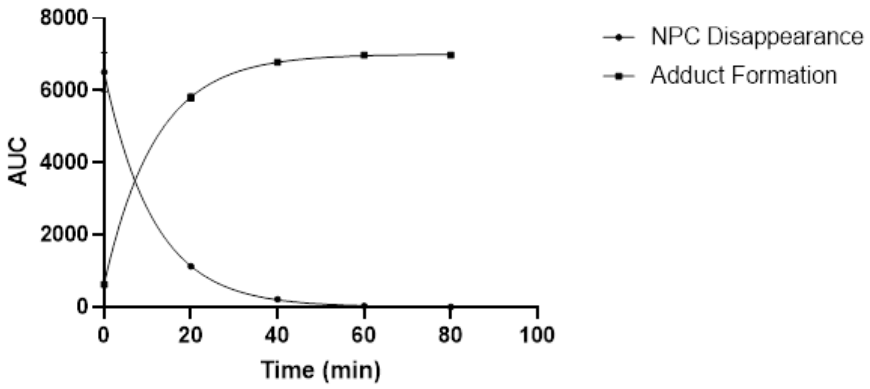

Figure S4.8. Plot of disappearance of NPC (1 mM) and formation of adduct for the addition of 1d (10 mM) vs time (min) in 67 mM CHES buffer (0.5% v/v DMSO) at pH 9.0, $\mu = 0.100$, T = 62°C. The area under the curve (AUC) was integrated from the chromatograph at 214 nm for the peaks corresponding to NPC and the adduct. The AUC data for disappearance of NPC were fitted to a mono-exponential decay with the constraint that the plateau = 0 and the data for formation of adduct were fitted to a mono-exponential association with the constraint that $Y_0 = 0$ to afford the k_{obs} values summarized in **Table S4.3**.

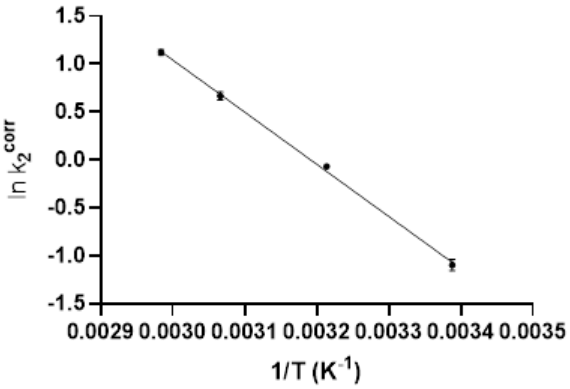

Figure S4.9. Arrhenius plot showing $\ln(k_2^{corr})$ vs 1/T for the addition of 1d to NPC in 67 mM CHES buffer (0.5% v/v DMSO), pH = 9.0, μ = 0.100. The data were fitted to a linear regression to obtain a slope of -5440 ± 143 and y-intercept of 17.36 ± 0.45, R^2 = 0.9986.

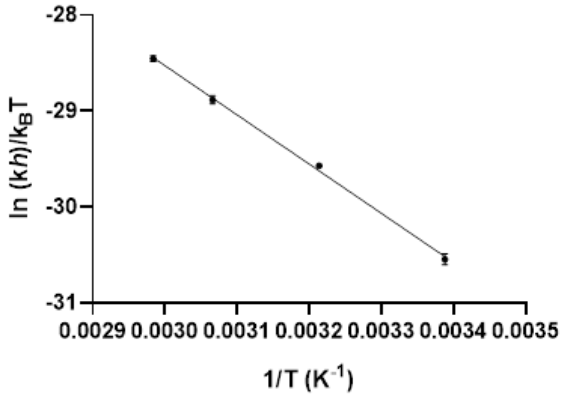

Figure S4.10. Eyring plot showing $\ln((k_2h)/(k_BT))$ vs 1/T for the addition of 1d to NPC in 67 mM CHES buffer (0.5% v/v DMSO), pH = 9.0, μ = 0.100. The data were fitted to a linear regression to obtain a slope of -5126 ± 146 and y-intercept of -13.15 ± 0.46, R^2 = 0.9984.

Table S4.3. Observed rate constants (k_{obs}), calculated second order rate constants (k_2^{calc}), and corrected second order rate constants (k_2^{corr}) for the addition of MPA (**1d**) to NPC at variable temperatures. Measurements were made in duplicate for both the disappearance of acetamide and appearance of adduct. Errors represent the standard deviation of the replicate values.

Temp (°C)	**k_{obs} (10^3 s^{-1})**	**k_2^{calc} ($M^{-1}s^{-1}$)**	**k_2^{corr} ($M^{-1}s^{-1}$)**	**ln(k_2^{corr})**	**ln((k_2^{corr}h)/k_BT)**
22	0.1596 ± 0.0049	0.01596 ± 0.00049	0.3344 ± 0.0103	-1.0953 ± 0.0589	-30.543 ± 0.059
38	0.4460 ± 0.0116	0.04460 ± 0.00116	0.9345 ± 0.0243	-0.0678 ± 0.0255	-29.568 ± 0.026
52	0.9299 ± 0.0396	0.09299 ± 0.00396	1.9483 ± 0.0829	0.6670 ± 0.0432	-28.880 ± 0.043
63	1.4650 ± 0.0442	0.14650 ± 0.00442	3.0695 ± 0.0926	1.1215 ± 0.0304	-28.453 ± 0.030

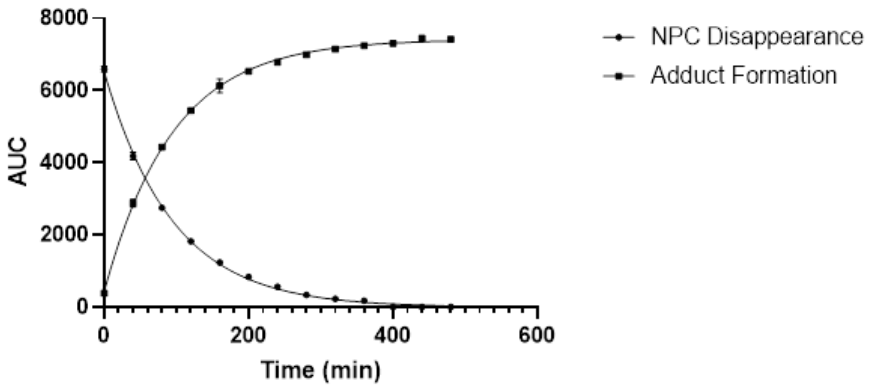

Figure S4.11. Plot of disappearance of NPC (1 mM) and formation of adduct for the addition of 1d (10 mM) vs time (min) in 67 mM CHES buffer (0.5% v/v DMSO), pH 9.0, μ = 0.050, T = 22°C. The area under the curve (AUC) was integrated from the chromatograph at 214 nm for the peaks corresponding to NPC and the adduct. The AUC data for disappearance of NPC were fitted to a mono-exponential decay with the constraint that the plateau = 0 and the data for formation of adduct were fitted to a mono-exponential association with the constraint that $Y_0 = 0$ to afford the k_{obs} values summarized in **Table S4.4**.

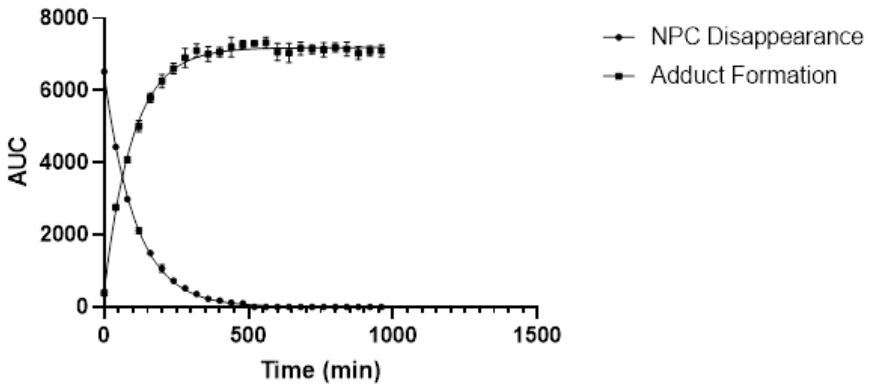

Figure S4.12. Plot of disappearance of NPC (1 mM) and formation of adduct for the addition of 1d (10 mM) vs time (min) in 67 mM CHES buffer (0.5% v/v DMSO), pH 9.0, μ = 0.075, T = 22°C. The area under the curve (AUC) was integrated from the chromatograph at 214 nm for the peaks corresponding to NPC and the adduct. The AUC data for disappearance of NPC were fitted to a mono-exponential decay with the constraint that the plateau = 0 and the data for formation of adduct were fitted to a mono-exponential association with the constraint that $Y_0 = 0$ to afford the k_{obs} values summarized in **Table S4.4**.

Table S4.4. Observed rate constants (k_{obs}), calculated second order rate constants (k_2^{calc}), and corrected second order rate constants (k_2^{corr}) for the addition of MPA (**1d**) to NPC at varying ionic strengths. Measurements were made in duplicate for both the disappearance of acetamide and appearance of adduct. Errors represent the standard deviation of the replicate values.

[KCl] (M)	k_{obs} (10^3 s^{-1})	k_2^{calc} ($M^{-1}s^{-1}$)	k_2^{corr} ($M^{-1}s^{-1}$)
0.050	0.1834 ± 0.0070	0.01834 ± 0.00070	0.3843 ± 0.0146
0.075	0.1662 ± 0.0134	0.01662 ± 0.00134	0.3483 ± 0.0282
0.100	0.1596 ± 0.0049	0.01596 ± 0.00049	0.3344 ± 0.0103

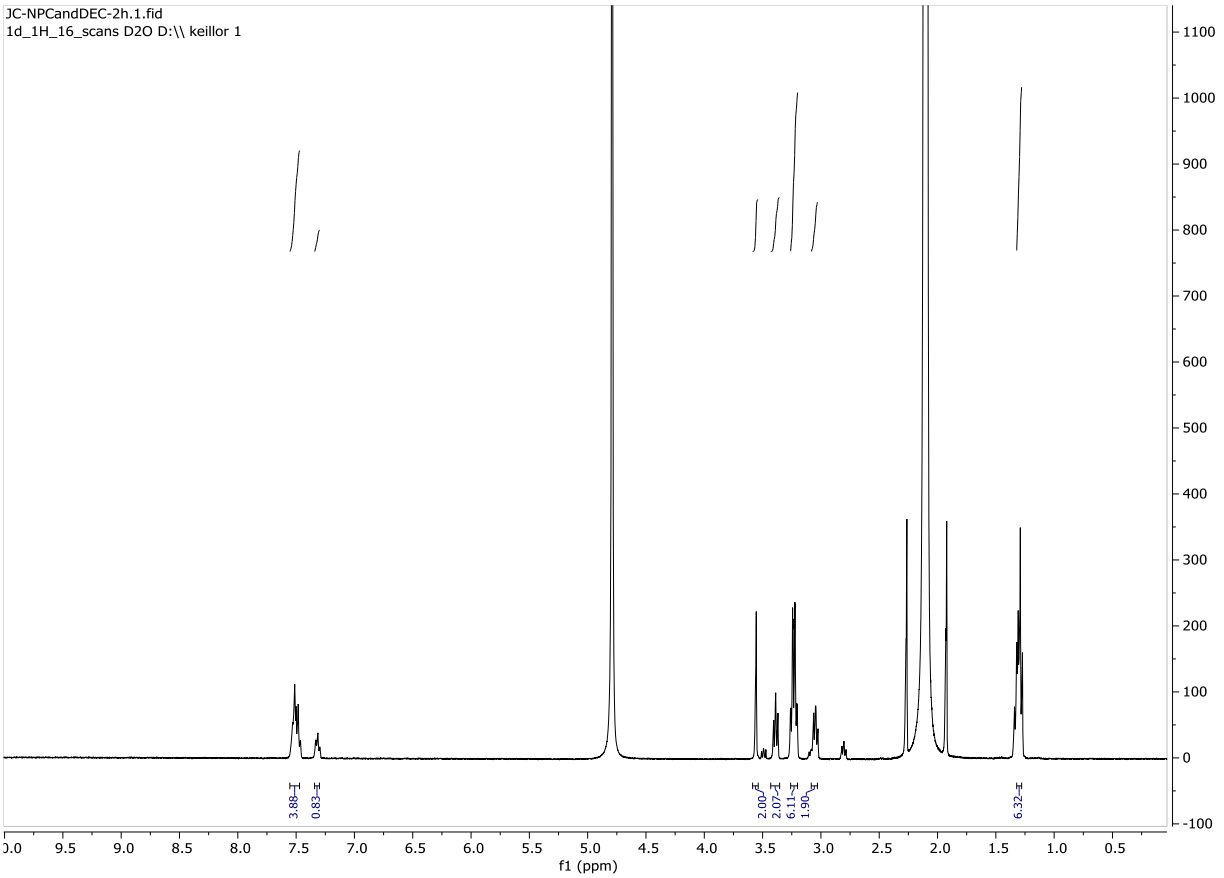

Figure S4.13. ^{1}H-NMR spectrum of adduct formed after 2 hours of allowing DEC to react with NPC in deuterated buffer.

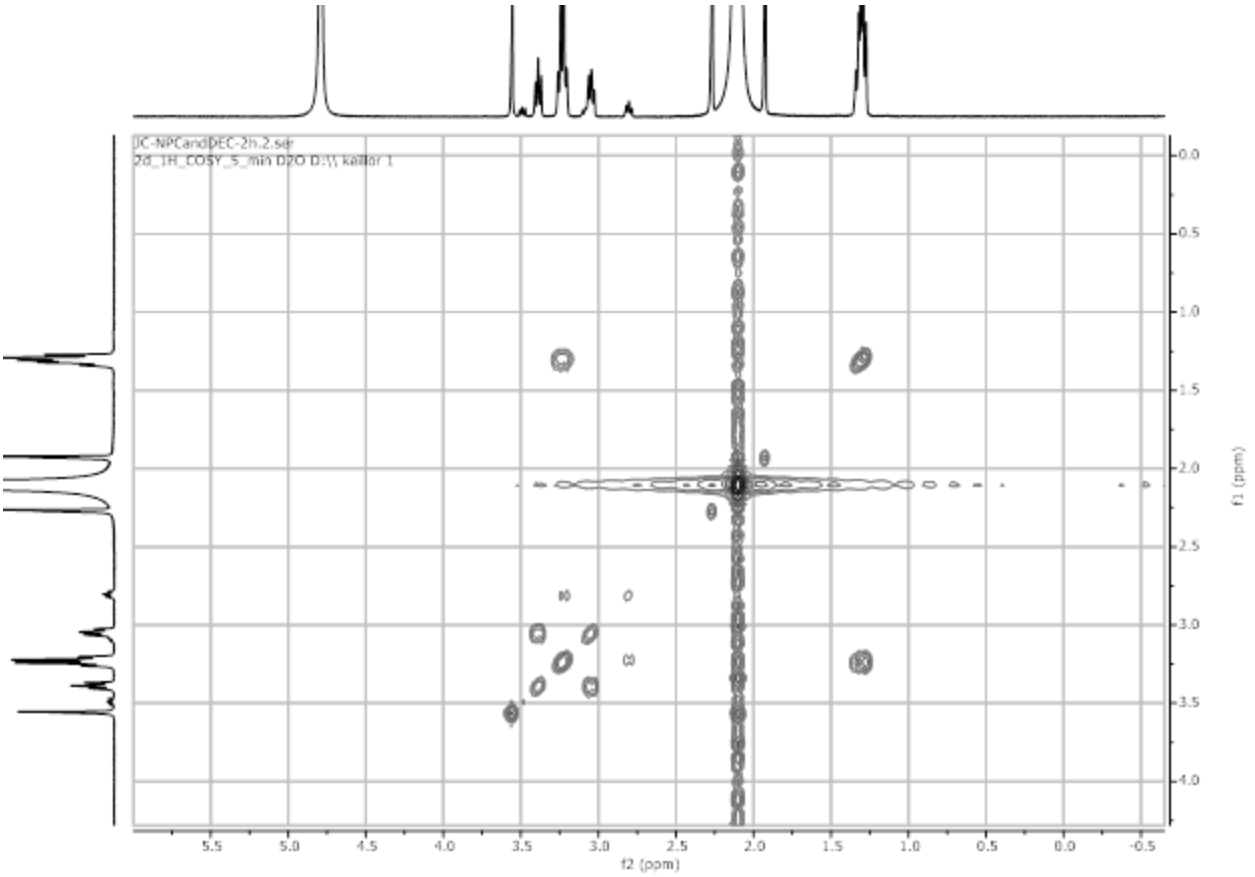

Figure S4.14. COSY spectrum of adduct formed after 2 hours of allowing DEC to react with NPC in deuterated buffer.

Table S4.5. Cartesian Coordinates of DFT-Calculated Structures

N-phenyl chloroacetamide

19

g98_logfile structure: 23

N	-0.455752	-0.102793	-0.000058
C	-1.302676	0.943677	0.000067
C	-2.794610	0.634774	0.000057
H	-3.229492	1.090507	-0.885569
O	-0.986920	2.120180	0.000190
C	0.951625	-0.106150	-0.000046
C	1.576787	-1.352996	0.000093
C	1.725568	1.051331	-0.000163
C	2.956647	-1.442926	0.000122
H	0.976106	-2.254839	0.000187
C	3.109871	0.944930	-0.000125
H	1.249745	2.018163	-0.000274
C	3.733695	-0.292169	0.000015

H	3.425458	-2.418603	0.000231
H	3.703943	1.850174	-0.000209
H	4.813575	-0.361424	0.000045
H	-0.890687	-1.013027	-0.000151
Cl	-3.263235	-1.089767	-0.000074
H	-3.229463	1.090364	0.885772

TS – methylthiolate chloroacetamide

24

g98_logfile structure: 32

N	0.282585	0.412989	-0.480867
C	-0.808840	0.278938	0.328099
C	-2.100068	0.631393	-0.334896
H	-2.997560	0.406353	0.209333
O	-0.758291	-0.009131	1.512319
C	1.626435	0.141188	-0.204261
C	2.530882	0.261007	-1.263056

C	2.100382	-0.231593	1.053567
C	3.877508	0.014614	-1.069941
H	2.171344	0.549563	-2.244025
C	3.455272	-0.477048	1.231004
H	1.412436	-0.327278	1.877251
C	4.351751	-0.357623	0.181230
H	4.559778	0.113563	-1.904834
H	3.808912	-0.766425	2.212966
H	5.405524	-0.551293	0.333088
H	0.085519	0.642959	-1.440279
H	-2.164635	0.762884	-1.398936
Cl	-2.123882	2.735159	0.105895
S	-2.221491	-1.866878	-0.922121
C	-2.923518	-2.389323	0.670059
H	-2.917376	-3.477385	0.750387
H	-2.330809	-1.980800	1.491098
H	-3.953878	-2.047004	0.784356

N-phenyl bromoacetamide

19

g98_logfile structure: 23

N	0.144468	0.104147	-0.000045
C	-0.578164	1.240142	-0.000085
C	-2.096144	1.119780	-0.000070
H	-2.472993	1.622924	-0.885743
O	-0.126044	2.371490	-0.000150
C	1.542689	-0.058750	0.000013
C	2.021885	-1.368829	-0.000130
C	2.443204	1.003158	0.000134
C	3.382631	-1.614834	-0.000117
H	1.322919	-2.197189	-0.000239
C	3.806428	0.740106	0.000159
H	2.080393	2.017774	0.000186
C	4.285452	-0.559870	0.000052
H	3.737706	-2.637405	-0.000230

H	4.499423	1.572051	0.000276
H	5.350442	-0.751519	0.000068
H	-0.387824	-0.752653	-0.000104
H	-2.472956	1.623049	0.885552
Br	-2.871655	-0.662954	0.000057

TS N-phenyl bromoacetamide

24

g98_logfile structure: 35

N	-0.570415	-0.134609	-0.496951
C	0.466884	0.231542	0.310644
C	1.801165	0.194693	-0.361721
H	2.617562	0.636407	0.178267
O	0.360299	0.480809	1.499880
C	-1.938230	-0.188382	-0.209196
C	-2.796532	-0.516277	-1.262291
C	-2.476979	0.060505	1.053064

C	-4.161891	-0.593615	-1.059484
H	-2.385662	-0.710957	-2.246200
C	-3.850249	-0.020564	1.240419
H	-1.825086	0.314799	1.872337
C	-4.701030	-0.345820	0.196278
H	-4.807904	-0.848812	-1.890042
H	-4.254871	0.175592	2.225710
H	-5.769625	-0.405815	0.355999
H	-0.334038	-0.295873	-1.461497
H	1.881930	0.123044	-1.430790
Br	2.388932	-1.959386	0.048063
S	1.307157	2.706248	-0.906920
C	1.893857	3.338931	0.692707
H	1.605360	4.383495	0.820198
H	1.453036	2.760449	1.507301
H	2.980715	3.275913	0.774332

N-phenyl iodoacetamide

19

g98_logfile structure: 24

N	0.855283	-0.086474	0.758031
C	-0.074335	0.897625	0.663244
C	-1.428330	0.525180	1.226817
H	-1.931435	1.420708	1.573218
O	0.120461	1.995472	0.175069
C	2.184709	-0.101136	0.299081
C	2.913474	-1.271323	0.516167
C	2.790431	0.973543	-0.347825
C	4.226359	-1.367042	0.093262
H	2.446370	-2.110246	1.018535
C	4.109362	0.861943	-0.766896
H	2.236369	1.881637	-0.518394
C	4.834587	-0.298834	-0.552570
H	4.775647	-2.282901	0.270189

H 4.570889 1.703006 -1.268960

H 5.862096 -0.372737 -0.883735

H 0.552205 -0.940466 1.197012

H -1.387020 -0.219759 2.015439

I -2.668176 -0.297310 -0.318826

TS N-phenyliodoacetamide

24

g98_logfile structure: 64

N -0.773390 0.006725 -0.423928

C 0.104121 0.489431 0.500640

C 1.340002 1.079621 -0.087842

H 1.958978 1.648908 0.579117

O -0.063272 0.422551 1.706404

C -2.038852 -0.558060 -0.219828

C -2.875359 -0.666937 -1.332413

C -2.483980 -1.025224 1.015792

C	-4.133315	-1.229057	-1.212898
H	-2.534701	-0.304289	-2.295321
C	-3.750408	-1.583151	1.121205
H	-1.845552	-0.946593	1.880245
C	-4.582194	-1.689826	0.017652
H	-4.766861	-1.303488	-2.087676
H	-4.085258	-1.941164	2.086888
H	-5.567513	-2.126983	0.112958
H	-0.549363	0.212121	-1.383378
H	1.423554	1.256657	-1.143697
I	2.813575	-0.927486	-0.105146
S	-0.001175	3.344799	-0.238674
C	-1.731993	3.002166	0.205213
H	-1.788174	2.353644	1.082264
H	-2.246526	3.934874	0.442378
H	-2.267501	2.515030	-0.611122

N-phenylacetamide thioether product

23

g98_logfile structure: 31

N	-0.163819	0.064547	-0.327762
C	-0.965917	1.141443	-0.178166
C	-2.441596	0.908326	-0.495800
H	-2.608375	1.249495	-1.519544
O	-0.595384	2.255367	0.150540
C	1.224386	-0.050552	-0.150941
C	1.785575	-1.310445	-0.364050
C	2.045648	1.011935	0.219414
C	3.145661	-1.506115	-0.209084
H	1.148909	-2.138574	-0.653026
C	3.409308	0.799880	0.371683
H	1.619257	1.987580	0.385864
C	3.968415	-0.450222	0.160805
H	3.563760	-2.490190	-0.378500

H	4.039023	1.632226	0.660263
H	5.032802	-0.602647	0.282586
H	-0.648924	-0.783036	-0.592611
H	-3.018550	1.557162	0.161969
S	-3.069708	-0.777257	-0.419002
C	-3.015272	-1.057044	1.361831
H	-3.650475	-0.339308	1.878806
H	-3.394383	-2.062457	1.535855
H	-1.995153	-0.992135	1.738234

Table S4.6. Second order rate constants calculated according to Eyring transition state theory, using activation energies calculated for the reaction of *N*-phenylhaloacetamides with methanethiol.

***N*-phenylhaloacetamide derivative**	**Calculated $k_2 = \frac{k_B T}{h} \exp\left(-\frac{\Delta G^{\ddagger}_{calc}}{k_B T}\right)$ ($M^{-1}s^{-1}$)**
Cl	6.07×10^{-5}
Br	1.07×10^{-1}
I	1.77×10^{-1}

Table S4.7. DFT-calculated activation energies for the reaction of *N*-phenylhaloacetamides with methanethiol in water and dichloromethane (DCM) solvents.

***N*-phenylhaloacetamide derivative**	**Calculated $\Delta G^{\ddagger}$ (kcal/mol)**	
	Water	DCM
Cl	19.1	16.4
Br	14.7	12.3
I	14.4	5.9